High power ultrafast laser design and high-order harmonic generation in capillary discharge plasmas

by

David M. Gaudiosi

B.S., Saint Joseph's University, 1999

M.S., University of Colorado at Boulder, 2002

A thesis submitted to the

Faculty of the Graduate School of the

University of Colorado in partial fulfillment

of the requirements for the degree of

Doctor of Philosophy

Department of Physics

2007

This thesis entitled:
High power ultrafast laser design and high-order harmonic generation in capillary discharge plasmas
written by David M. Gaudiosi
has been approved for the Department of Physics

Henry C. Kapteyn

Margaret M. Murnane

Date

The final copy of this thesis has been examined by the signatories, and we find that both the content and the form meet acceptable presentation standards of scholarly work in the above mentioned discipline.

Gaudiosi, David M. (Ph.D., Physics)

High power ultrafast laser design and high-order harmonic generation in capillary discharge plasmas

Thesis directed by Profs. Henry C. Kapteyn and Margaret M. Murnane

Chirped pulse amplification (CPA) has been used for over twenty years to generate high power, sub-picosecond laser pulses. In a chirped pulse amplifier, an ultrashort pulse is stretched, amplified, and compressed, usually using grating stretchers and compressors. Despite the low efficiency (50–60%) of grating compressors, this CPA scheme has remained virtually unchanged since the first demonstration [Strickland and Mourou, *Opt. Commun.* **56**, 219 (1985)]. In the first half of this thesis, a novel amplifier design, based on downchirped pulse amplification (DPA), is presented. The DPA design utilizes a negative dispersion stretcher and a positive dispersion compressor, usually a block of transparent material. This design avoids many of the limitations, such as low efficiency and sensitivity to alignment, of traditional grating- and prism-based CPA systems. In addition to presenting the first demonstration of a DPA based amplifier system, the DPA scheme is combined with a simple, compact stretcher based on grisms to construct an ultrafast amplifier scalable to >40 kHz, a previously underdeveloped amplifier repetition frequency range.

CPA systems have also enabled the study of high-field physics, specifically high-order harmonic generation. High-order harmonic generation is a process which generates extreme-ultraviolet radiation through the interaction of an intense laser field with a medium, usually a noble gas. Depletion of the neutral atoms, plasma defocusing, and energy loss due to ionization limit the laser intensity and ultimately the highest possible photon energy that can be generated. Using ions in a waveguide as the generating medium can minimize these limitations, extending the maximum photon energy.

In the second half of this thesis, a method for generating high harmonic radiation from ions is demonstrated. A capillary discharge is used to preionize a low pressure xenon gas before a high intensity, ultrashort pulse is injected. The discharge generates ions and mitigates the plasma defocusing and ionization loss experienced by the ultrashort laser pulse, allowing for the generation of photon energies much higher than those previously observed in xenon. This method could be combined with the technique of quasi-phasematching to efficiently generate short wavelength radiation.

Dedication

To my family and friends.

Acknowledgements

First and foremost, I would like to thank my advisors, Professors Margaret Murnane and Henry Kapteyn, for all of their guidance and patience over that last seven years. This thesis would not have been possible without their expertise, generosity, and advice. I would also like to thank Dr. Sterling Backus for his knowledge and friendship. He showed me how to align and maintain an amplifier system and patiently answered my incessant questions. I am indebted to Sterling for getting me involved in the DPA projects, as well as for his assistance during those projects. His expertise has been invaluable.

I've learned a great deal from my conversations with Professor Jorge Rocca and his enthusiasm for science is very contagious. I am grateful to Tim Whiteaker, Michael Grisham, and Brendan Reagan from CSU for teaching me the intricate inner workings of capillary discharges as well as constructing various discharges for use in our collaborative experiments. I also want to thank Tim, Mike, and Brendan for driving down to Boulder from Fort Collins for the past four years. I know the drive was neither short nor pleasant (especially in the snow). In addition, Tenio Popmintchev has been a valuable asset in the lab over the past few years and deserves my thanks. Also, the advice and assistance provided by visiting professor Barry C. Walker was indispensable.

I've had the pleasure of working with a large number of scientists, post-docs and students during my graduate studies at JILA, all of whom have enriched my graduate experience and to whom I owe a great deal. Specifically I want to thank the following peo-

ple for their insight, knowledge, and assistance: Ralph Jimenez, Etienne Gagnon, Amy Lytle, Steve Kane, Ariel Paul, Ra'annan Tobey, Nick Wagner, Erez Gershgoren, Arvinder Sandhu, Oren Cohen, Guido Saathoff, Andrea Wüest, Thomas Weinacht, Thomas Feurer, Randy Bartels, Tim Lei, Kendal Read, Erik Zeek, Luis Miaja-Avila, Richard Sandberg, Daisy Raymondson, Jim Holtsnider, Scott Christensen, David Samuels, Anthony Calamai and anyone I may have forgotten.

The fantastic support staff of JILA deserves my gratitude, specifically Rachael Tearle, Randall Holliness, Brian Lynch, Ed Holliness, Joel Frahm, Jim McKown, Mike Paige, David Alchenberger, Hans Green, Todd Asnicar, and Kim Hagen. Much less would have gotten done without their help.

I want to also thank my family and friends for their support over the past seven years, including Lesley Cook, Robert Dollinger, and Jonathan Moore.

Lastly, thanks to the entire staff of IHOP, including Kristy, Sergei, Adelita, Justin, Carmen, and Hussam, for allowing me to stay for hours, and keeping the Pepsi flowing, while I wrote this.

Contents

Chapter

Tables

Table

Figures

Figure

Chapter 1

Introduction

The technology of high power, ultrafast lasers has progressed rapidly in the past 20 years. An ultrafast laser system is one that can produce high energy pulses with picosecond and sub-picosecond duration, enabling investigation of previously inaccessible phenomena. The short pulse widths produced by these laser systems are extremely useful for studying protein dynamics [2] and chemical reactions [3] on extremely short time scales, while the unique combination of a short pulse width and high pulse energy, provided by these laser systems, has advanced the fields of laser machining [4], laser particle acceleration [5], and high-harmonic generation [6]. The rapid progress of the ultrafast laser field can be attributed to a few key developments. First is the development of the chirped pulse amplification (CPA) scheme [7]. The CPA scheme allowed ultrashort pulses to be amplified to extremely high energies, while avoiding the nonlinear effects and optical damage associated with the propagation of high power, ultrashort pulses, by stretching the ultrashort pulse in time before amplification and then recompressing it after amplification. The second key is the development of grating based stretchers and compressors [8–12], which are attractive for several reasons. Pulse stretching can be achieved by using any dispersive optical element, but grating based systems allow for stretching and compressing without propagation through a transparent dielectric material, which can introduce nonlinear effects. Also, employing grating stretchers and compressors allows for large stretch/compression factors in a small amount of space.

The last key that has contributed to the rapid progress of ultrafast laser technology is the development of high quality, solid state crystals that have broad amplification bandwidths (Ti:sapphire and Ytterbium-based crystals). The large bandwidth of these crystals has allowed the generation of extremely short (few cycle) laser pulses [13]. In addition, these crystals can store large amounts of energy, allowing for the development of terawatt and petawatt laser systems [14, 15].

Surprisingly, there has been very little development in stretcher/compressor design since CPA was first demonstrated, even though the efficiency of grating based compressors reduces the overall amplifier efficiency by a factor of $\sim$2 due to loss from the gratings in the pulse compression process. In the first part of this thesis, a novel amplifier design, which stretches the pulse with negative dispersion instead of positive dispersion, is demonstrated. Subsequently, a grism stretcher is used in this novel design to build an amplifier in a previously underdeveloped range of amplifier repetition frequencies. A grism is a compact optical element composed of gratings and prisms which exhibits some of the advantages of both gratings and prisms.

The second part of this thesis will describe experiments designed to generate high-order harmonic radiation from a preionized gas. High-order harmonic generation (HHG) coherently upconverts laser light from the visible and infrared into the extreme-ultraviolet (EUV) region of the spectrum. Over the past decade, HHG has been used as an EUV light source for a wide range of applications, such as investigating surface dynamics [16], holographic imaging [17], and probing static molecular structure [18, 19]. In HHG, the nonlinear interaction between a gas [20, 21] and an intense laser field produces high order harmonics of the laser frequency. The laser field first ionizes the atom, then accelerates the liberated electron away from the ion, finally generating high-order harmonic photons when the laser field reverses and the oscillating electron recollides with its parent ion. The highest photon energy that can be produced via this interaction is predicted [22,23] by the cutoff rule to be $\hbar\omega_{max} = I_p + 3.17U_p$, where I_p is

the ionization potential of the atom and $U_p \propto I_L\lambda^2$ is the ponderomotive energy of the electron in the laser field. Here I_L is the peak laser intensity and λ is the wavelength of the driving laser field. It is clear from this cutoff rule that the range of harmonic photon energies generated is determined by the laser intensity.

However, in most experiments to date, the maximum observed photon energy generated via HHG has been limited not by the available laser intensity (I_L), but by the intensity at which the target atoms are nearly completely ($\sim$98%) ionized - or the "saturation intensity" I_s ($< I_L$). To obtain the highest possible photon energy, this saturation intensity can be increased either by using a shorter duration laser pulse, or by using atoms with a higher ionization potential, both of which allow neutral atoms to survive to a higher laser intensity. Using atoms with higher ionization potentials is a good solution to this problem, but these atoms have smaller effective nonlinear susceptibilities [24]. Therefore they can be used to generate higher photon energies, but with lower photon flux. Generating harmonic radiation from ions has the potential to circumvent both problems since ions can exhibit very large ionization potentials and large effective susceptibilities.

There are many ways to generate ions for the purpose of high harmonic generation. For the experiments described in this thesis, a fast capillary discharge was used to generate the ions. A fast capillary discharge consists of a hollow capillary filled with a low pressure gas and a pair of electrodes, one at each end of the capillary. A fast rising current pulse is passed through the gas, simultaneously ionizing the gas and heating the resulting plasma. Interaction of this hot plasma with the cold capillary walls causes a radial temperature gradient in the plasma, with a maximum temperature on axis and a minimum near the capillary walls. This temperature gradient leads to a density gradient, with a minimum density on axis and a maximum near the capillary walls. Since the index of refraction of a plasma is lower for regions of high electron density, this concave density gradient comprises a plasma waveguide, allowing for the guiding of

very high intensity pulses [25–28].

In addition to the plasma waveguide aspect of a capillary discharge, it is beneficial to the high harmonic process to preionize the generating medium before the laser pulse is injected. Intense laser pulses will ionize the medium during the high harmonic generation process, causing a reduction in laser intensity for two reasons. First, ionization of the gaseous medium requires energy, which is provided by the laser pulse. Therefore, the laser pulse will lose energy as it propagates through the ionizing medium. Second, the ionization is an intensity dependent process, resulting in larger ionization on axis and no ionization near the beam edge. This results in an electron density that is maximum on axis and minimum near the edge, which, for reasons outlined above, acts like a negative lens. The negative lensing effect defocuses the laser beam, reducing the laser intensity. Preionizing the gaseous medium can minimize both of these effects, leading to higher laser intensities. This work shows the benefits of generating harmonics from ions in a preformed plasma. In addition, a capillary discharge is shown to be an almost ideal way to generate ions for the purposes of HHG.

Appendix A describes an attempt at amplifying HHG radiation in a capillary discharge laser. Given the low conversion efficiency of the high harmonic generation process, an external EUV amplifier would be extremely beneficial as it would significantly increase the EUV pulse energy while preserving the short pulse nature of HHG. Amplification of high harmonic radiation has been previously demonstrated [29–31] using laser created gain media, but there have been no published attempts using a capillary discharge as the amplifier. Capillary discharges have been used as EUV lasers [32,33], so they are a straightforward choice for an EUV amplifier. Unfortunately, this attempt did not result in the amplification of HHG radiation, but the problem was reduced to alignment of the HHG with the gain medium. Seeing as this is not a fundamental limitation, future experiments could prove successful with the necessary improvements.

Chapter 2

High-power, ultrafast laser amplifiers

2.1 Introduction

High-power ultrafast lasers produce high energy pulses with sub-picosecond pulse widths. The short pulse nature of these lasers make them extremely useful for the study of fast biological [2] and chemical [3] dynamics. In addition, the combination of short pulse width and high pulse energy that these lasers produce make them ideal for high field experiments [4–6]. Unfortunately, the large electric fields produced by these lasers make amplification to high energy difficult. Therefore, most high-power ultrafast laser amplifiers make use of the chirped-pulse amplification (CPA) technique [7] in which a femtosecond pulse is positively chirped to increase its duration to 0.1-1 ns, amplified and then recompressed back to femtosecond duration. The most successful architecture uses a Ti:sapphire crystal, pumped by a green laser, as the gain medium. To date, Ti:sapphire laser systems have been implemented in two basic configurations: very high repetition rate systems (>100 kHz) with low pulse energy (<10 μJ), pumped by CW lasers [34] and low to medium repetition rate systems (10 Hz - 10 kHz) with high pulse energy (1 mJ - a few Joules) pumped by pulsed lasers [35,36]. Average powers available from ultrafast laser systems have been increased from ∼1 W in the 1990's, to ∼10 W today through the use of cryogenic cooling of the Ti:sapphire crystal [36–38]. This has allowed millijoule-level ultrafast laser systems to be implemented at repetition rates greater than 10 kHz.

A very large fraction of ultrafast laser applications require pulses with moderate energy, in the tens of microjoules to a few millijoules range, and with typical peak powers of gigawatts – for example, as an energy source for broadly-tunable optical parametric amplifiers (OPA's), or simply to generate a peak focused intensity of $\sim 10^{14}$–10^{15} W/cm^2 for material ablation or VUV/EUV harmonic generation. Although these applications often require pulse energies in excess of that available from CW-pumped amplifier systems, they benefit from higher repetition rates than those available with amplifier systems pumped by pulsed lasers. In addition, the lower repetition rate amplifier systems usually provide much more pulse energy than is needed. As a result, a large fraction of the available laser energy is discarded.

2.1.1 Chirped pulse amplification

The chirped pulse amplification (CPA) method, shown schematically in Figure 2.1, is extremely useful for amplifying ultrashort laser pulses while avoiding the technical problems associated with high peak laser power. A thorough discussion of high power amplifiers already exists in the literature [35], so this section will provide a brief overview of the chirped pulse amplification scheme. First applied to lasers by Mourou and his co-workers [7, 39, 40], the first step in the CPA process is to stretch ultrashort light pulses, originating from a mode-locked laser. These mode-locked, ultrashort pulses are stretched in time either by passing them through a grating pulse stretcher [11], by propagating the light through optical fiber [7], or through other means of introducing positive (i.e. normal) dispersion on the pulse. By performing a Taylor expansion on the phase in the frequency domain, the different orders of dispersion can be identified:

$$\phi(\omega) = \phi_0 + \left.\frac{d\phi}{d\omega}\right|_{\omega_0} (\omega - \omega_0) + \frac{1}{2}\left.\frac{d^2\phi}{d\omega^2}\right|_{\omega_0} (\omega - \omega_0)^2 + \frac{1}{3!}\left.\frac{d^3\phi}{d\omega^3}\right|_{\omega_0} (\omega - \omega_0)^3 + \ldots \quad (2.1)$$

where $\phi(\omega)$ is the total phase and each of the derivatives are evaluated at the central fre-

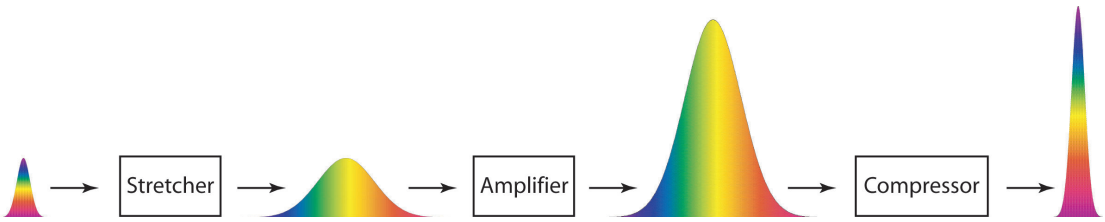

Figure 2.1: Schematic diagram of chirped pulse amplification.

quency, ω_0. The first derivative is defined as the group delay (τ_{gd}), the second derivative is the second-order dispersion (SOD) (also know as group velocity dispersion (GVD)), the third derivative is the third-order dispersion (TOD), and so on. In dielectric materials, dispersion results from a wavelength dependent index of refraction ($n(\lambda)$). This index can be used to calculate the group delay, GVD, and higher order dispersion terms, as outlined below:

$$\begin{aligned} \phi(\lambda) &= \frac{2\pi n(\lambda) L}{\lambda} && (2.2) \\ \tau_{gd}(\lambda) &= \frac{d\phi}{d\omega} = \frac{d\lambda}{d\omega}\frac{d\phi(\lambda)}{d\lambda} \\ &= \frac{L}{c}\left(n(\lambda) - \lambda\frac{dn}{d\lambda}\right) && (2.3) \\ \mathrm{GVD}(\lambda) &= \frac{\lambda^3 L}{2\pi c^2}\frac{d^2 n}{d\lambda^2} && (2.4) \\ \mathrm{TOD}(\lambda) &= \frac{-\lambda^4 L}{4\pi^2 c^3}\left(3\frac{d^2 n}{d\lambda^2} + \lambda\frac{d^3 n}{d\lambda^3}\right) && (2.5) \end{aligned}$$

where L is the material length, λ is the vacuum wavelength and c is the speed of light. Optical fiber stretchers use this material dispersion to stretch and compress ultrashort pulses. On the other hand, grating stretchers (compressors) spatially disperse the spectrum and have a longer physical path length for shorter (longer) wavelengths (Fig. 2.2) [8–12]. It can be seen from Figure 2.2(a) that for a grating compressor the optical path length ABC is given by:

$$P = \frac{L_g}{\cos\theta}(1 + \cos(\gamma - \theta)) \tag{2.6}$$

where L_g is the perpendicular distance between gratings, θ is the diffracted angle, and γ is the incident angle, as indicated in Figure 2.2(a). The diffracted angle can be determined from the grating equation

$$\sin\gamma + \sin\theta = \lambda/d \tag{2.7}$$

where d is the groove spacing. The group delay is the path length divided by the speed of light ($\tau_{gd} = P/c$) and, from this expression, the GVD and TOD for a grating compressor can be determined (Eqs. 2.8 and 2.9).

$$GVD = \frac{-\lambda^3 L_g}{2\pi c^2 d^2}\left[1-\left(\frac{\lambda}{d}-\sin\gamma\right)^2\right]^{-3/2} \tag{2.8}$$

$$TOD = \frac{3\lambda^4 L_g}{4\pi^2 c^3 d^2}\left[\frac{1+\frac{\lambda}{d}\sin\gamma-\sin^2\gamma}{\left(1-\left(\frac{\lambda}{d}-\sin\gamma\right)^2\right)^{5/2}}\right] \tag{2.9}$$

From Equation 2.8, it can be seen that the GVD for a grating pair is always negative. These expressions are for a single pass through the optical system. To prevent spatial chirp (i.e. different frequencies in the laser pulse have different spatial positions/divergence) in the output beam, the pulse is retro-reflected back through the system, resulting in twice the dispersion, but zero spatial chirp.

In 1987, Martinez showed that, by placing a telescope between the gratings, the dispersion is determined by the distance between the second grating and the image of the first grating [11, 12]. By making this effective distance negative, the dispersion will have the opposite sign of a grating pair. Either an anti-parallel grating pair separated by an even number of lenses (Fig. 2.2(b)) or a parallel grating pair separated by an odd number of lenses can achieve this negative effective distance. As can be seen from Figure 2.2(b), the effective distance between the gratings is $L_g = 2\Delta x$, with a positive distance occurring when the image of the first grating is in front of the second. By combining this grating stretcher with a grating pair, a matched stretcher/compressor pair is formed, with the GVD and TOD exactly canceling out.

The applied chirp can increase the duration of the light pulse by factors of 10^3 – 10^4, lowering the peak power of the pulse. This lower peak power makes it possible to amplify the pulse to high energy without distorting the pulse due to nonlinear effects (discussed below) or damaging the laser amplifiers by exceeding the damage threshold of

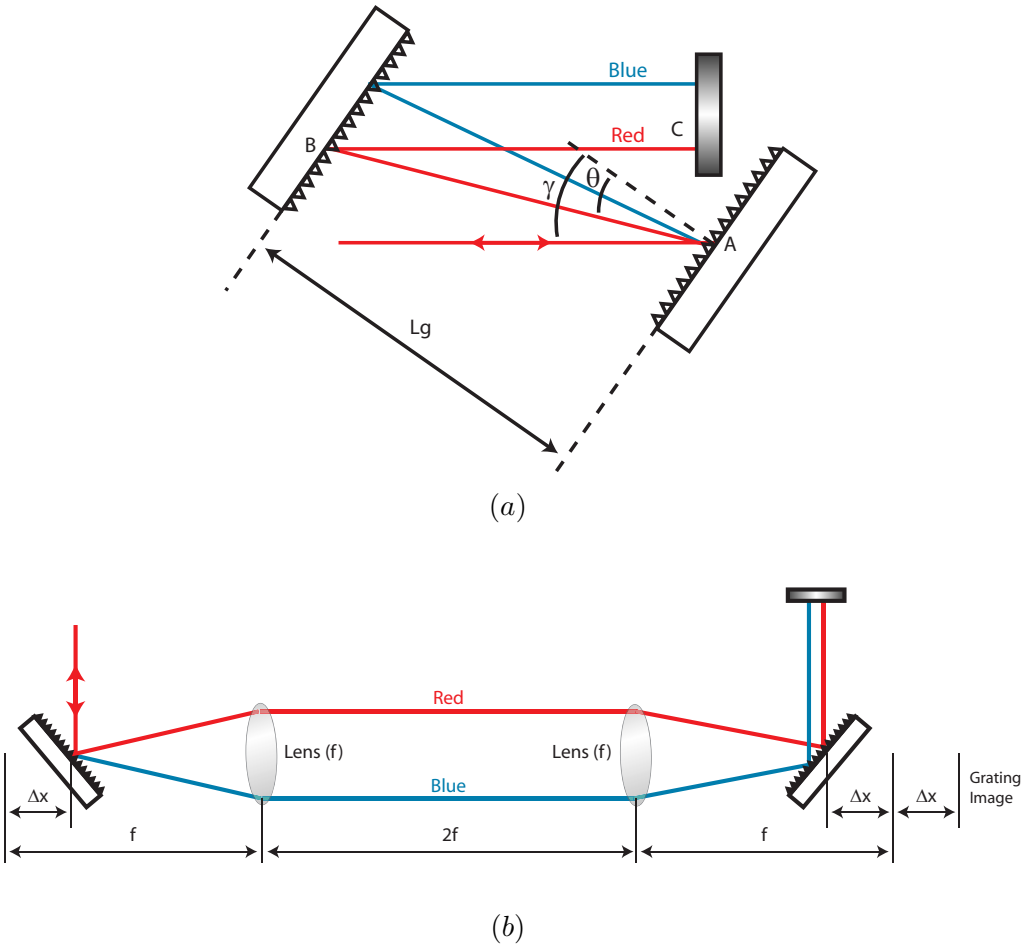

Figure 2.2: Grating based (a) compressor and (b) stretcher configurations.

the crystals and optics. Subsequently, a pulse compressor is used to provide a wavelength dependent optical path length with negative chirp – opposite to that of the stretcher and the amplifier medium. This regains an ultrashort duration pulse, but with dramatically increased peak power. Progress in CPA lasers in recent years has been enabled in large part by the development of very large area gratings, making it possible to generate peak powers of up to a petawatt [14].

Despite its usefulness, CPA has significant limitations, particularly in the pulse compression process. The technique of downchirped pulse amplification (DPA) was developed to bypass or overcome the limitations imposed by the CPA technique. The results obtained with DPA establish it as a viable alternative to CPA, particularly for Ti:sapphire amplifiers in the 10–100 kHz repetition frequency range. In addition, it may be useful for very large amplifier systems to avoid the use of large area compressor gratings or for very short pulses to avoid the bandwidth limitations of grating compressors.

2.1.2 Limitations of CPA compressors

Despite the recent advances in amplifier performance, chirped pulse amplification has significant limitations, primarily associated with the pulse compression process. Pulse compressors exhibit a high sensitivity to alignment, due to the fact that the spectrum of the pulse is spatially dispersed. Small misalignments result in unwanted high-order dispersion [41] and spatial-chirp [42]. High-order dispersion will prevent efficient recompression of a pulse, limiting the peak intensity. Spatial chirp will cause a beam to focus to a spectrally dispersed line, which can cause dramatic, unwanted effects in an experiment. As can be seen in Figure 2.2, the large number of optics in a stretcher/compressor pair make accurate alignment difficult. Grating based compressor systems have the added limitations of thermal loading and high energy and bandwidth losses. Thermal loading is an effect where the intensity of the laser is high enough to cause a local thermal expansion of the grating surface. Due to this expansion, the two

grating surfaces are no longer parallel, introducing distortions on the laser pulse. This local expansion will also cause a slight misalignment of the beam, adding to the pulse distortions. As for grating losses, typical grating efficiencies are around 85–90%. Compressors have two gratings and the pulse traverses this optical system twice to prevent spatial chirp. This results in four reflections from the gratings, giving an overall grating compressor efficiency of 50–65%, significantly limiting the amplifier output energy. The output spectrum of CPA systems is strongly influenced by the wavelength-dependent efficiency of diffraction gratings, which can cause minor reshaping of the spectrum and significant bandwidth losses. Bandwidth losses can also occur due to the finite size of the gratings. Depending on the amount of compression needed, the spectrum can be dispersed to a spatial extent larger than that of the grating, resulting in clipping of the edges of the spectrum. Prism compressors are an alternative to grating compressors and are also commonly used in CPA. They do not suffer from thermal loading or large energy losses, but they require much more table space for a given compression factor. Prism compressors can suffer from non-linear phase distortions that are caused by propagating an intense beam through a transparent material. In high energy applications, it may be difficult or expensive to obtain prisms or gratings large enough to prevent non-linear effects from distorting the beam. All of these limitations motivated the development of a novel scheme for the amplification of microjoule to millijoule level energy, ultrafast pulses.

2.1.3 Thermal lensing

Another limitation that affects all high power laser systems is thermal lensing. When a high power pump laser is focused onto an amplifier crystal, such as Ti:sapphire, the absorbed pump energy creates a temperature gradient, and thus an index gradient, across the pump beam profile. The seed pulse experiences this index gradient as a lens, affecting the pulse on each pass. This focusing can lead to lower efficiency due

to a changing seed spot size or it can lead to more detrimental effects such as optical damage to the amplifier mirrors or crystals. The focal length of this thermal lens is given by [43]:

$$f = \frac{2\,k\,\pi r^2}{(dn/dT)\,E\,\nu} = \frac{2\,k}{(dn/dT)\,F\,\nu}, \tag{2.10}$$

where k is the thermal conductivity of the crystal, r is the pump radius, dn/dT is the change in the index of refraction with temperature, E is the pulse energy, ν is the repetition frequency, and $F = E/(\pi r^2)$ is the pump fluence. For Ti:sapphire at 300 K, $k = 0.43$ W/(cm K) [44] and $dn/dT = 1.3 \times 10^{-5}$ /K [45], while at 73 K, $k = 9.8$ W/(cm K) [44] and $dn/dT = 1.8 \times 10^{-6}$/K [45]. Therefore, the focal length of the thermal lens is increased from <1 cm for an uncooled crystal to approximately 6 m for a cryogenically cooled crystal at 100 W pump power. Figure 2.3 shows the thermal lens focal length, at 50 and 77 K, as a function of repetition rate, when the peak focused fluence is kept constant at 3 J/cm^2 for a gain of ∼5 per pass. A number of laser amplifier systems have made use of cryogenic cooling for higher performance [36–38, 46]. As an example, a 100 kHz system running at 50 K would have a thermal lens of ∼110 cm, while the same system at 77 K would have a thermal lens of ∼36 cm, or at room temperature, ∼2 mm.

2.2 Downchirped pulse amplification

Downchirped pulse amplification (DPA) is similar to CPA, but avoids many of the problems associated with CPA compressors, especially schemes which employ grating-based compressors. In DPA, pulses from a mode-locked oscillator are passed through an optical system that applies negative dispersion to stretch the pulse. Such negative dispersion stretchers can easily be constructed without focusing optics, which are necessary in positive dispersion grating-based stretchers, making accurate alignment more

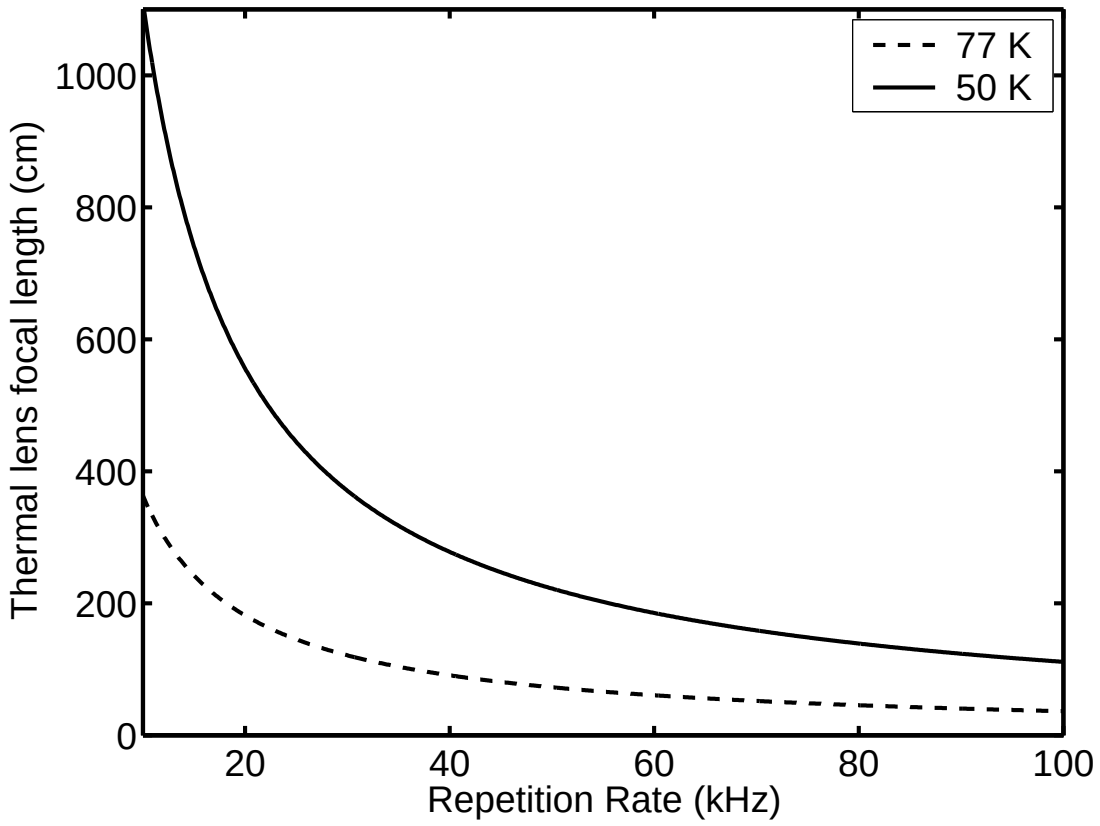

Figure 2.3: Focal length of the thermal lens induced in a Ti:sapphire crystal at 77 K (dashed) and 50 K (solid), showing the benefit of cryocooling the Ti:sapphire crystal. The fluence is kept constant at 3 J/cm^2.

difficult. The downchirped pulses are then amplified and recompressed simply by passing the pulses through a block of transparent (dispersive) material. Pulse recompression based on material dispersion has several significant advantages over standard grating-based pulse compressors. First, the DPA scheme makes it much easier to implement a "hands-free" amplifier design, since the compressor is insensitive to small misalignments of the pulse compressor that can introduce high-order dispersion and spatial chirp. The small beam size, low pulse energy, and absence of focusing optics in the stretcher makes it easier to accurately align the stretcher and to avoid spatial chirp, while the alignment free compressor makes the stretcher alignment more straightforward.

Second, the compressor has low (potentially near-zero) energy and spectral bandwidth throughput losses, increasing the overall system efficiency. Most, if not all, of the amplifier energy is usable for experiments. Third, for the case of high-average-power systems, the DPA scheme avoids beam distortion due to thermal loading of the compressor gratings. Fourth, this scheme can result in a simplified, compact amplifier design. Finally, since DPA avoids any spatial-spectral dispersion of the beam in the high power part of the system, it may be preferable for laser amplifier systems that generate carrier-envelope stabilized pulses. It has been discussed that grating- or prism-based dispersion can result in a coupling of beam pointing to the carrier-envelope offset, resulting in added noise in this parameter [47], although recent measurements have indicated this is not a major issue [48, 49]. In the DPA scheme, spatial-spectral dispersion is used only in the low-power part of the system before amplification, therefore these optics can be included "in-loop" at high repetition rates in any CEO feedback stabilization.

Furthermore, the DPA scheme also has advantages over amplifier designs that use prism compressors to avoid grating throughput losses [50]. Prism compressors are relatively bulky, and still have limited spectral aperture. Increasing beam aperture in a large area prism compressor also increases required material path, which must be compensated by further prism separation. Furthermore, nonlinear distortion in a

prism-based compressor is accumulated during a time where the beam has angular and spatial-spectral chirp, possibly resulting in complex beam distortions. In contrast, high-intensity propagation of the pulse occurs exclusively during collimated propagation in DPA, resulting in relatively little distortion.

At first glance, pulse compression by use of material dispersion seems counterintuitive because the CPA scheme was designed, in part, to prevent the nonlinear pulse distortion that results from propagation of a high-power beam in the amplifier system material. Nonlinear pulse distortion arises from the nonlinear contribution to the index of refraction:

$$n = n_0 + n_2 I \tag{2.11}$$

where n is the index of refraction of the material, n_0 is the static index, n_2 is the nonlinear coefficient, and I is the intensity of the light. This intensity dependent index of refraction gives rise to an intensity dependent phase. The nonlinear phase difference between the center, most intense part of the beam, and the beam edge is called the B-integral of the beam and is given by Equation 2.12.

$$B = \frac{2\pi n_2}{\lambda} \int_0^L I(z) dz, \tag{2.12}$$

where n_2 is the material nonlinear index, λ is the vacuum wavelength, L is the material length, and $I(z)$ is the pulse intensity at the beam's center as a function of propagation distance. It is a measure of the phase retardation of the most intense portion of the beam. This phase retardation can cause a self-focusing effect, increasing the intensity and thus the phase retardation. If the intensity is large enough, the self-focusing can lead to intensity spikes and filamenting, all of which degrade the beam quality. The spatial mode quality of the beam may be quantified by a factor denoted M^2, which is defined as

$$M^2 = \frac{\omega_L \theta_L}{\omega_0 \theta_0}, \tag{2.13}$$

where ω_L and θ_L are the waist radius and half-angle divergence of the laser beam, respectively, and ω_0 and θ_0 are the waist radius and half-angle divergence of a perfect TEM_{00} (i.e. Gaussian) mode, respectively. Therefore, a TEM_{00} mode will propagate in free space with a half-angle divergence of

$$\theta_0 = \frac{\lambda}{\pi \omega_0} \tag{2.14}$$

where λ is the wavelength and ω_0 is defined above. When higher order spatial modes are present, as is the case with real laser beams, the beam will diverge faster:

$$\theta_L = \frac{\mathrm{M}^2 \lambda}{\pi \omega_L}. \tag{2.15}$$

Consequently, when a collimated TEM_{00} mode is focused by a lens, the resulting focal spot radius is

$$\omega_0 = \frac{\lambda f}{\pi \omega} \tag{2.16}$$

where f is the lens focal length and ω is the beam radius on the lens. For a beam composed of high order modes, the focal spot radius becomes

$$\omega_0 = \frac{\mathrm{M}^2 \lambda f}{\pi \omega}. \tag{2.17}$$

M^2 is a measure of how well a beam will focus in addition to being a measure of how closely the spatial profile resembles a perfect Gaussian mode, therefore making it a measure of beam quality.

Nonlinear distortions can be prevented by ensuring that the beam's cross section is large enough to keep the peak intensity low as the pulse propagates through the material and recompresses. For high pulse repetition rate systems, the beam size required for

this is typically smaller than would be required to prevent thermal distortions in a conventional grating compressor. The material path length in the amplifier system itself is also moderate compared with the final compression material's path length to ensure that the pulse does not compress significantly during amplification. Given these considerations, the DPA approach is particularly suited to high repetition rate, high average power, broadband Ti:sapphire laser amplifier systems. It has been recognized that, in parametric amplification of signal pulses with positive chirp, the idler is emitted with negative chirp and can be compressed by material dispersion [51]. DPA would also be appropriate for optical parametric CPA (OPCPA) schemes [52]. Following this initial work, OPCPA using downchirped pulse amplification has been implemented [53, 54].

Chapter 3

Down-chirped pulse amplification experiments

3.1 Down-chirped pulse amplification

The previous chapter described the motivation for the down-chirped pulse amplification (DPA) scheme. This section describes the first demonstration of a DPA based laser system [38]. A schematic of the DPA experimental setup is shown in Figure 3.1. Pulses with a FWHM bandwidth of 85 nm, at a repetition rate of 88 MHz [55], and with a pulse energy of 6 nJ, are stretched to 20 ps through a 2-stage pulse stretcher before being injected into the amplifier. The first stage of pulse stretching consists of a pair of 600 g/mm gratings separated by a distance of 7.5 cm, with the laser beam incident on these gratings at an angle of 70°. The second stage consists of a pair of SF18 prisms with a tip-to-tip separation of 123 cm, through which the beam makes four passes. The second prism is inserted into the dispersed spectrum such that the tip corresponds to a wavelength of ∼700 nm. The grating pair provides most of the stretch while the prism pair precompensates for a third-order dispersion of 4.81×10^4 fs^3 introduced by the material-based pulse compressor (SF18).

Prior to amplification, the laser beam also passes through a Pockels cell pulse selector, which selects a single pulse from the pulse train at a repetition rate adjustable from 7–10 kHz. The downchirped pulses are then injected into a single stage, 12-pass, ring amplifier that employs a cryogenically cooled, Ti:sapphire amplifier crystal [35, 36]. The 6 mm thick, Brewster angle, Ti:sapphire crystal is enclosed in a vacuum cell and

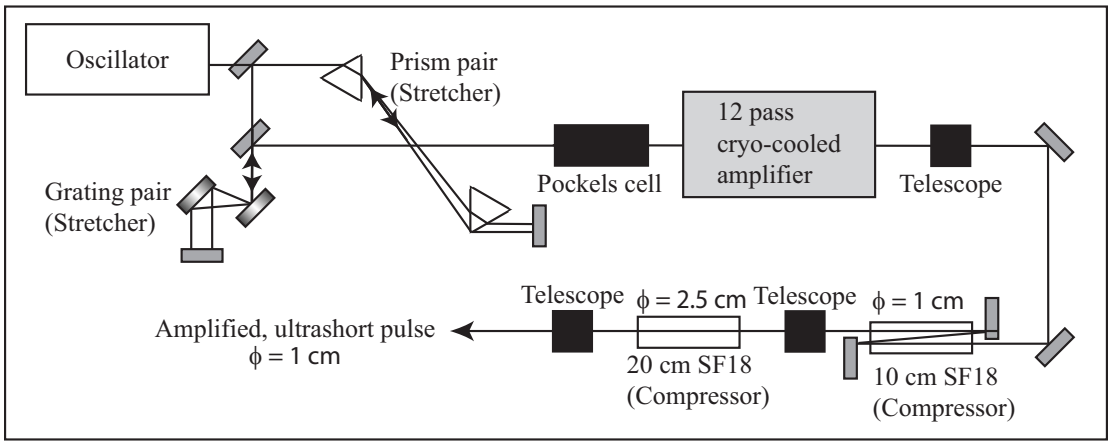

Figure 3.1: Experimental setup schematic for downchirped pulse amplification.

cooled using a closed-cycle helium refrigerator to a temperature of 73 K.

The amplifier is pumped at a repetition rate of 7–10 kHz with a 100 W average power, Q-switched, 532 nm laser (Quantronix Eagle). The amplifier ring uses two 1 m radius of curvature mirrors and a high angle of incidence, flat mirror. Following amplification, the 4 mm diameter laser beam is then sent into the first of two telescopes. The first telescope is constructed of two converging lenses with a pinhole at the focus. This configuration expands the beam to a diameter of 1 cm and serves as a spatial filter, removing high spatial frequencies from the beam profile. The first lens of the spatial filter takes the input beam and generates the Fourier Transform of the spatial profile at the focus. The pinhole at the focus acts as a low-pass filter and the second lens reconstructs the filtered spatial frequencies into an almost perfect Gaussian profile. The beam then makes three passes through a 10 cm long block of SF18 material to reduce the pulse duration to 4.3 ps. The laser beam diameter is expanded to a diameter of 2.5 cm and pulse compression is completed by passing the beam through another 20 cm of SF18. SF18 was chosen as the compressor material because it has a large amount of group velocity dispersion (GVD) per length and a small nonlinear index, n_2. A large amount of GVD per length allows for less glass in the compressor. The second and third order dispersion (TOD) are calculated from Eqs. 2.4 and 2.5. The wavelength dependent index of refraction can be calculated from the Sellmeier equation [56] and the Sellmeier coefficients for a given material [57, 58]. Typical values of second order dispersion and third order dispersion per length for different materials at 800 nm are given in Table 3.1.

3.1.1 Results

After 12 passes through the Ti:sapphire amplifier crystal, the output pulse energy is 1.1 ± 0.1 mJ, corresponding to an extraction efficiency of 12 %. After passing through the material compressor, the result is a recompressed pulse width of 29 ± 1 fs in a 1.1

Material	GVD (fs^2/cm)	TOD (fs^3/cm)
Fused Silica	363	277
BK7	448	323
Sapphire	583	425
SF18	1548	973

Table 3.1: Values of GVD per length and TOD per length for typical transparent optical materials at 800 nm.

mJ energy pulse. The pulse duration (Fig. 3.2) was measured using frequency resolved optical gating [59] based on second harmonic generation (SHG-FROG). Residual high order dispersion is the main factor preventing full recompression to the transform-limited pulse duration of 25 fs. To compensate this high order dispersion, a DPA based laser system can include a pulse shaper, such as an LCD [60], acousto-optic modulator [61], or deformable mirror set-up [62].

Figure 3.3 shows the average power of the compressed output pulses as a function of amplifier repetition rate. For repetition rates of 7–10 kHz, the pump pulse energy was maintained at 8.85 mJ. The average output power increased with increasing repetition rate and the highest average power recorded was 10.7 W at 10 kHz, which corresponds to an output pulse energy of 1.1 mJ. The pulse energy was between 1.0 and 1.1 mJ for all repetition rates measured. The compressed extraction efficiency was 11–12% over the entire repetition rate range tested. Most importantly, the throughput of the pulse compressor is 90%, including a 5% loss in the spatial filter and surface losses. Typical throughput of grating-based pulse compressors is 60%.

Limiting nonlinear effects in the compression stage is critical. As mentioned previously, nonlinear phase accumulation, represented by the B-integral (Eq. 2.12), can lead to beam distortions which adversely affect beam quality and focusability. Calculations show that the B-integral for the entire amplifier system ($n_2 = 5.0 \times 10^{-16}$ cm^2/W for SF18), is 0.76 rad, with 0.44 rad accumulating in the first stage of compression where the beam is 1 cm in diameter. The B-integral accumulated in the amplifier itself is only

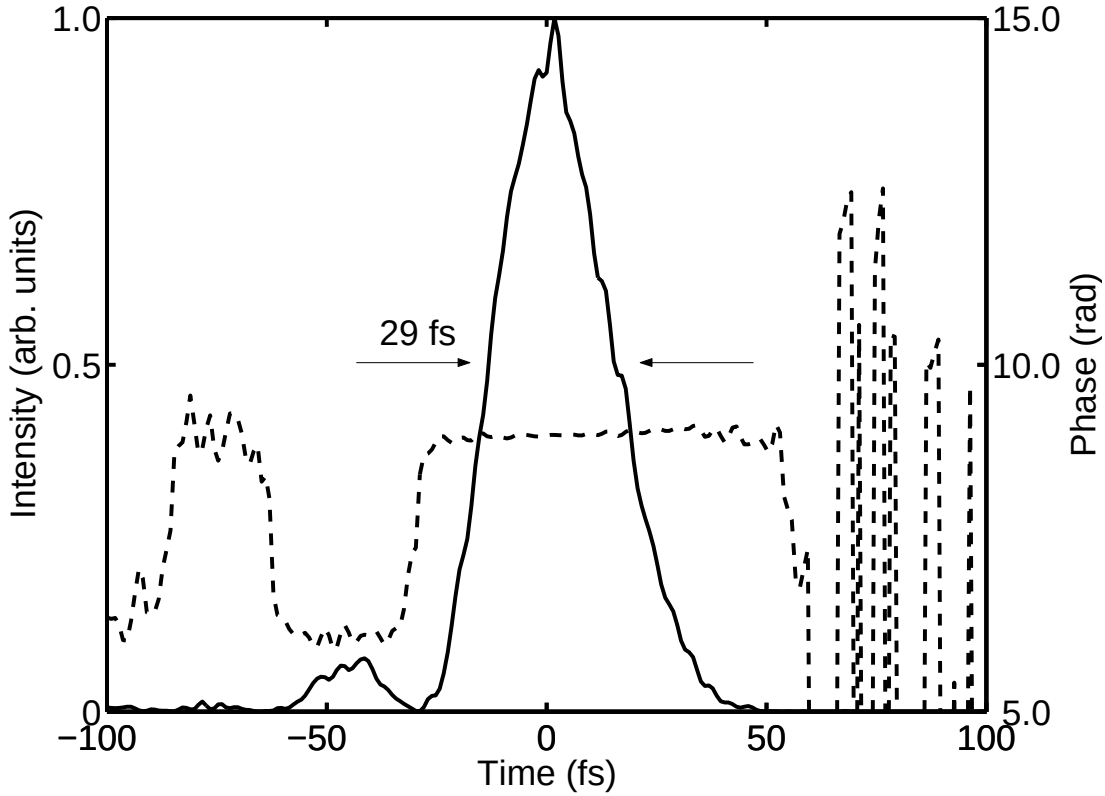

Figure 3.2: Temporal intensity (solid) and phase (dotted) of 1.1 mJ, 29 fs, amplified output pulse measured using SHG-FROG.

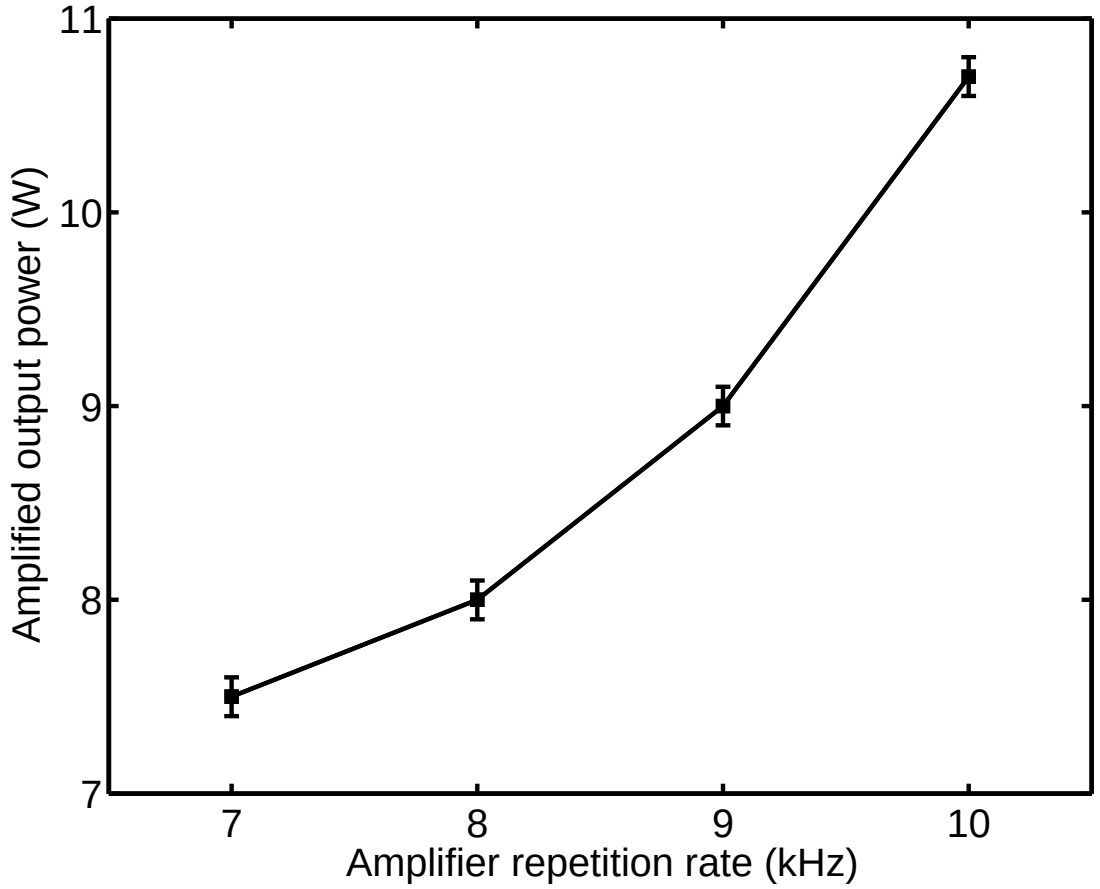

Figure 3.3: Average output power of the DPA system as a function of pulse repetition rate.

0.32 rad. The B-integral of 0.76 rad does not adversely influence focusing of the beam, as shown in the focused spot size and beam profile (Figs. 3.4a and 3.4b). Using f/104 focusing optics, a waist diameter of 106 μm is expected for a perfect gaussian beam. The measured M^2 of the amplified beam was 1.57, increasing the expected waist diameter to 166 μm. This is in very good agreement with the 164 $\pm$ 5 μm waist diameter measured. It should be noted that in the course of this work, no beam distortions were observed that could be attributed to energy absorption or thermal effects in the pulse compressor. Total energy absorption in the compressor is $<<1$ W, distributed over a large volume.

3.1.2 Discussion

In designing and constructing this downchirped pulse amplifier, a number of issues arose relating to dispersion management. Early designs of the DPA system made it clear that a simple grating pair would not suffice as a stretcher, due to the large TOD of the glass. Thus, the two stage stretcher was developed to precompensate for this large TOD. Unfortunately, optimization of this two stage stretcher was difficult due to the large number of independent parameters (grating angle, grating separation, prism separation, and minimum wavelength transmitted by the prism pair). Therefore, a LabVIEW program, written by Dr. Sterling Backus, was used to find the optimal configuration for the grating pair and prism pair. Minor experimental variations necessitated the adjustment of the stretcher from this optimal configuration to obtain an amplified, compressed pulse, but these adjustments were very minor.

In addition to the issue of optimizing the stretcher, another issue that arose was determining how long to stretch the pulse. Large stretch factors meant large amounts of glass and large amounts of TOD, while small stretch factors meant possible nonlinear effects and damage in the amplifier. Preliminary experiments showed that small stretch factors ($<$10 ps stretched pulse width) resulted in lower amplifier efficiency. This effect

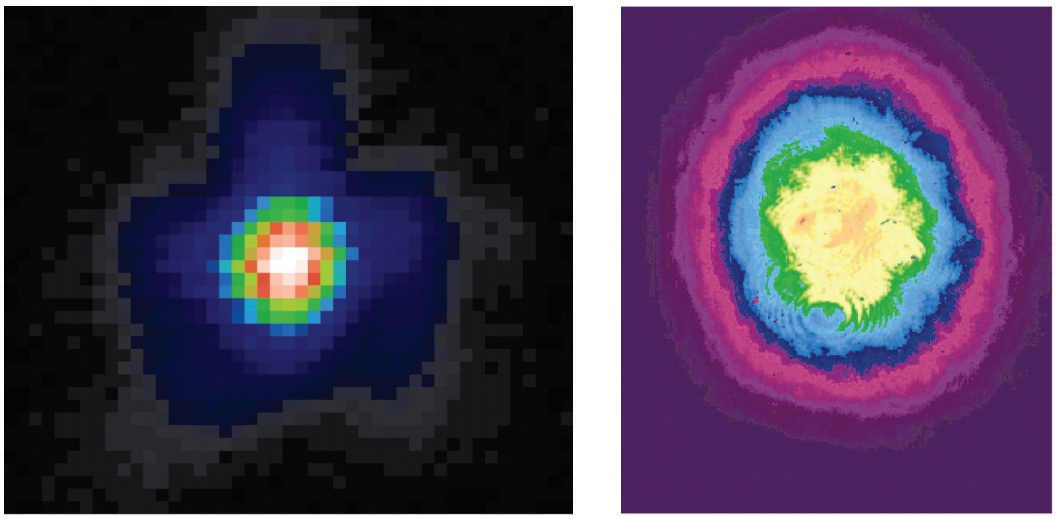

(*a*) (*b*)

Figure 3.4: Beam profiles of (a) focused beam waist using f/104 focusing, where the beam diameter is 164 microns; (b) 2.5 cm diameter, unfocused, compressed output beam, showing the good focusability of the amplified beam.

is due to the finite lower state lifetime of Ti:sapphire, as will be shown later in this chapter. Therefore, the 20 ps stretched pulse width was a compromise between extraction efficiency and recompression.

3.1.3 Conclusion

This downchirped pulse amplification system produced 29 ± 1 fs pulses, at repetition rates from 7–10 kHz, with pulse energies in excess of 1 mJ. Based on this performance, DPA is a viable alternative to standard CPA systems. DPA eliminates the problems associated with prism- and grating-based compressor designs commonly found in standard CPA systems. Grating-based compressor designs suffer from low energy throughput (50–60%), limited bandwidth throughput, high sensitivity to alignment which can lead to high order dispersion and spatial-chirp, and, in high-power laser systems, thermal loading. Prism-based compressors do not suffer from high throughput losses, but, like the grating-based compressors, they do have a limited bandwidth throughput and are highly sensitive to alignment. Unlike grating compressors, prism compressors have the added problem of spectrally dependent nonlinear phase (B-integral) accumulation in high-power laser systems. The material-based compressor used in DPA does not spectrally disperse the laser pulse, therefore eliminating the problems of alignment sensitivity and spectrally dependent nonlinear phase. In addition to this, the material compressor has virtually no throughput losses, extremely large bandwidth throughput (limited only by the transparency of the material used), and no thermal loading.

The main issue with material-based compressors is nonlinear phase accumulation. This effect can be minimized by ensuring a large beam size, and thus a low beam intensity. The appropriate beam size is no larger than that which would be required by a prism-based compressor. By using a material compressor, DPA systems increase compressor simplicity and energy and bandwidth throughput without significantly adding to

stretcher complexity. Despite this increase in stretcher complexity, stretcher alignment is somewhat easier than a grating-based, positive dispersion stretcher. In particular, this implementation of the downchirped amplification scheme resulted in the highest average power, single stage Ti:sapphire amplifier system at the time of demonstration. This DPA approach is particularly suited to very high repetition rate, high average power, laser amplifier systems where the beam diameter required to avoid nonlinear distortion effects is small and where the chirps required are modest.

3.2 High repetition rate down-chirped pulse amplification

Despite the usefulness of CPA and DPA, a gap has remained in ultrafast technology at pulse repetition rates of 20–100 kHz and pulse energies of ∼0.1 millijoule. CW laser-pumped systems have output pulse energies of ∼5 μJ, which is marginal or insufficient for many applications, such as pumping multiple OPA's, or for efficient high-order harmonic generation. On the other hand, systems using pulsed pump lasers are generally engineered to generate millijoule pulses. Many experiments are compelled to use these kilohertz systems but only use a small fraction of the total energy output. Recently, a 100 kHz regenerative amplifier based on DPA was demonstrated, producing 28 μJ, 39 fs pulses [63]. In addition, Yb-fiber laser amplifiers have been demonstrated that operate at $>$ 10 kHz and have a pulse energy of ∼140 μJ [64], but only compress to 220 fs. In other work, fiber amplifiers have produced very short (∼43 fs) pulses [65], but fiber systems have not been demonstrated that encompass all three properties: $>$10 kHz repetition rate, sub-50 fs pulses, and $>$100 μJ pulse energy.

A few papers report fractional millijoule CPA systems running at ∼10 kHz repetitions rates [66, 67]. However, use of these systems has been limited, despite the fact that high power frequency-doubled Nd:YAG lasers operating at 20–50 kHz and with average powers of 100 W are readily available. The reason is that, as mentioned before, thermal lensing (Eq. 2.10) is a serious limitation on performance.

This section will describe a cryogenically-cooled laser amplifier designed to be scalable to very high repetition rates [68]. A modified multipass amplifier design was used to ensure the scalability of the system. The new amplifier was designed to use pulse energies significantly less than the 8–10 mJ required in past designs. Since commercial green pump lasers are limited to ∼100 W average power, this energy requirement has limited the repetition rate of such a single stage, single pump laser amplifier to 10–15 kHz. To overcome this limitation, the new design makes use of tighter focusing in the amplifier ring to achieve the same single pass gain as previous systems. Due to the tighter focusing, shorter focal length mirrors were employed and a new optical design was incorporated to greatly reduce accumulated astigmatism in the amplified beam. Finally, these new optical designs were combined with downchirped pulse amplification (DPA), rather than conventional CPA, to reduce compressor losses [38]. The result is a compact, single stage amplifier design that is scalable to tens of kHz and produces moderate pulse energy with excellent beam quality. The use of a cavity-dumped seed laser eliminates the need for a Pockels cell for pulse selection, which can also limit the repetition rate due to power dissipation limitations of the electronic components.

3.2.1 Experimental setup

In DPA, the seed pulse is stretched using negative dispersion and then compressed using positive dispersion by passing the beam through a block of glass. In this work, two different experimental setups (Figs. 3.1 and 3.5) were used. Initially, a two-stage stretcher, as described in the previous section, was used to determine the beam quality (M^2) of the amplifier output with the old and new ring designs. Then the two stage stretcher was replaced with a one stage stretcher based on grisms [69], which was used for all subsequent measurements.

Grisms are optical elements that combine the properties of prisms and gratings. They have the interesting property that they can be designed such that the ratio of

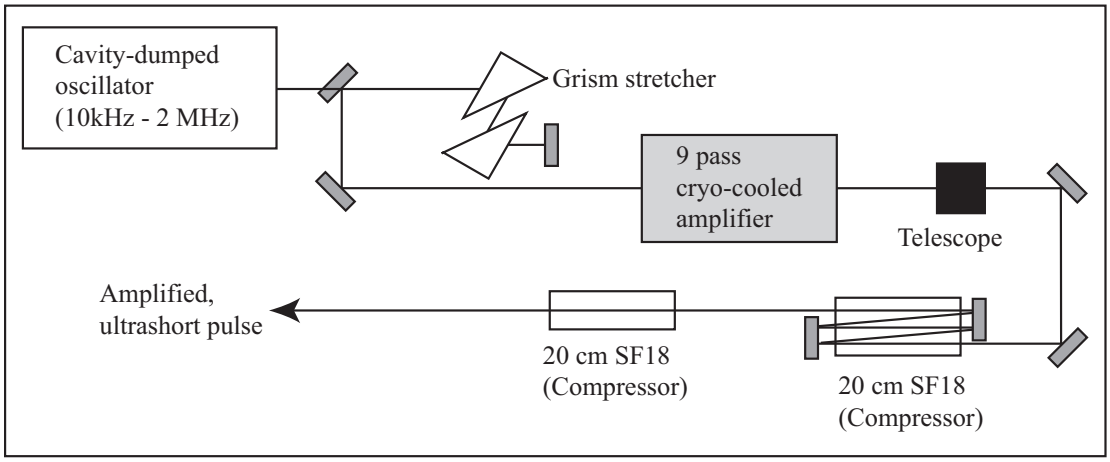

Figure 3.5: Experimental setup schematic for grism-based downchirped pulse amplification.

third order dispersion (TOD) to second order dispersion, or group velocity dispersion, (GVD) is equal in magnitude to that of most dispersive materials [70]. This, combined with the fact that both the TOD and GVD of the grisms is opposite in sign to that of material, makes the grisms better optimized for compressing femtosecond pulses than either grating or prism pairs.

The front end of the amplifier system is a cavity-dumped oscillator with a repetition rate that is variable up to 2 MHz. At repetition rates of 10–15 kHz, the cavity-dumped energy is ∼15 nJ per pulse with a spectrum that can support a 12 fs pulse. The pulse from the grism stretcher is adjustable from 5–30 ps, and has a pulse energy of ∼1 nJ. Due to the finite size (1") of the grisms, when the pulse is stretched to ∼30 ps, the spectrum is clipped and can only support a ∼16 fs pulse. The beam is near Brewster's angle on all of the entrance and exit faces, which reduces the loss through the stretcher without the need for anti-reflection (AR) coatings. These grisms were fabricated using off-the-shelf aluminum coated gratings, which limited the double pass stretcher efficiency to ∼10%; however, the use of optimized gold coated gratings will increase this to $> 75\%$. Nevertheless, the high input energy of the cavity-dumped seed laser allowed us to demonstrate saturated gain of the amplifier.

After the stretcher, the beam is sent into an amplifier consisting of a seven-mirror, nine pass multipass ring and a cryogenically cooled Ti:sapphire amplifier crystal. To obtain a smaller focal spot in the amplifier crystal, mirrors with a smaller (75 cm) radius of curvature (ROC) are used in this ring, compared with the standard 1.0 m ROC mirrors used previously [71]. However, use of shorter ROC mirrors in the original multipass design causes a degradation of the output mode and beam quality (Fig. 3.7a) due to increased astigmatism. A new amplifier ring (Fig. 3.6b) design was therefore implemented to minimize the incident angle of the beam on the curved mirrors. The incidence angle on the curved mirrors was dramatically reduced, as evident in Fig. 3.6b, and resulted in virtually no astigmatism in the output beam (Fig. 3.7b).

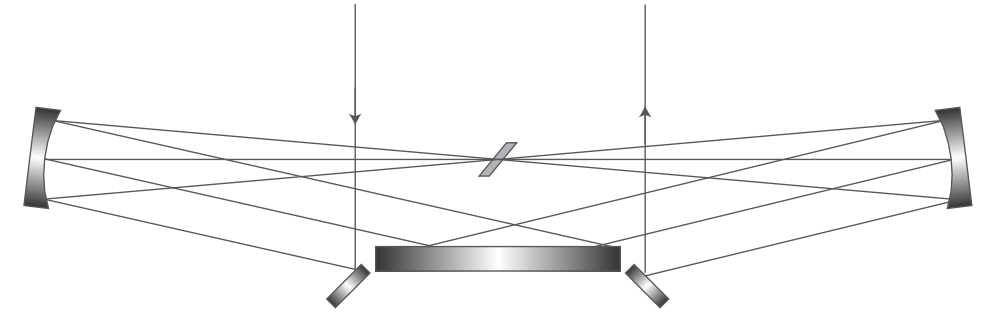

(*a*)

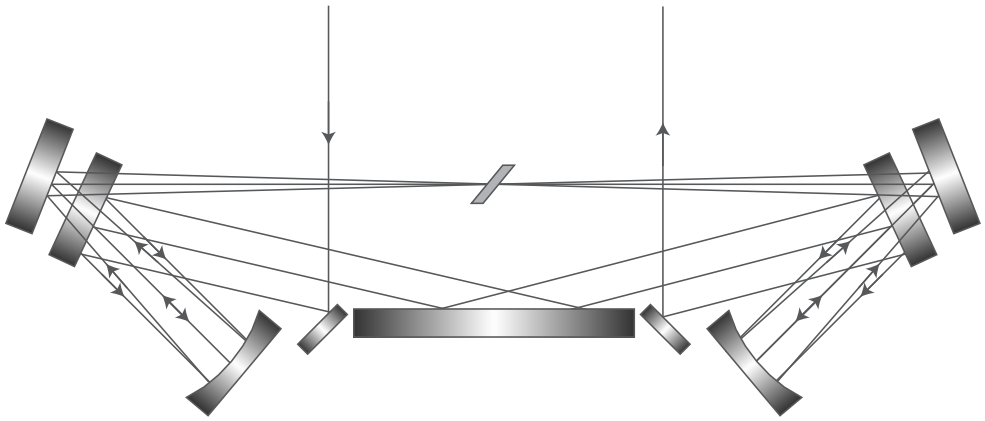

(*b*)

Figure 3.6: Schematic diagram of (a) original amplifier ring and (b) astigmatism-minimized amplifier ring. Only three passes are shown, but up to 10 passes can be employed with minimal astigmatism.

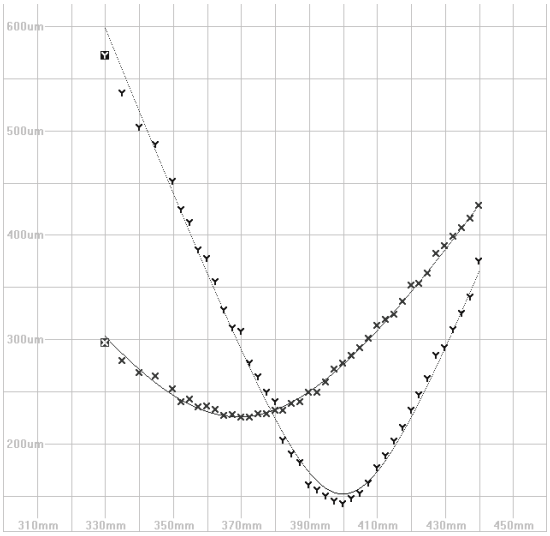

(*a*)

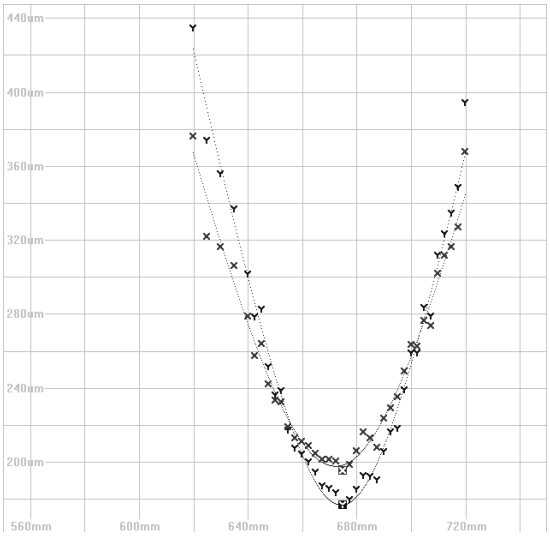

(*b*)

Figure 3.7: M^2 measurement of the amplified beam with (a) old ring design and (b) new ring design showing the dramatic reduction in astigmatism. The output of the old design has an M^2 of 1.14 and 1.24 in the x- and y-directions, respectively, while the new design has an M^2 of 1.18 and 1.26 in the x- and y-directions, respectively.

The 6 mm amplifier crystal is housed in a ultra-high vacuum cell and cooled to 50 K using a closed loop helium cryocooler. The system was pumped by a commercially available, doubled Nd:YAG laser (Quantronix Condor at 532 nm) capable of running at 5–20 kHz with up to 50 W average power. The pump pulse energy was limited to 2.3 mJ to allow this system to be scaled to >40 kHz. After the amplifier, the beam is sent into a telescope to provide a beam that slowly diverges from ∼1 cm to ∼2 cm diameter as the beam passes through the compressor material. This divergence minimizes the B-integral in the compressor while also allowing for a smaller block of glass for the compressor. This telescope also serves as a spatial filter, which ensures a spatial mode close to TEM_{00} with a throughput of 90%. The compressor consists of 120 cm of AR-coated SF18 glass. This 120 cm of path length was obtained with 5 passes each through two 10 cm long slabs and then a single pass through two 10 cm long, 1 inch diameter rods. The large number of surfaces (20) the beam encounters on the slabs reduces the throughput of the compressor from the theoretical value of 98% to 60% in this work.

3.2.2 Results

The stretched pulses in the DPA scheme are significantly shorter in duration (<40 ps) than those in typical CPA amplifiers (∼150 ps). Because of this, the lower state lifetime of Ti:sapphire can not be assumed to be much less than the stretched pulse length and will, therefore, effect the output power of the amplifier. A model of the amplifier, based on the Frantz-Nodvik equations (Eqs. 3.1, 3.2, and 3.3) [72], was developed to extract the lower state lifetime from the measured data. The Frantz-Nodvik equations are used to describe the propagation of a laser pulse in an amplifier medium. They consist of the photon transport equation and the rate equations for the levels of the amplifier medium.

$$\frac{\partial n}{\partial t} + c\frac{\partial n}{\partial z} = \sigma c n (N_2 - N_1) \tag{3.1}$$

$$\frac{\partial N_1}{\partial t} = \sigma c n (N_2 - N_1) \tag{3.2}$$

$$\frac{\partial N_2}{\partial t} = -\sigma c n (N_2 - N_1) \tag{3.3}$$

3.2.2.1 Amplifier simulation

The Ti:sapphire amplifier was simulated as a four level laser system as shown Figure 3.8, where P is the pumping rate, N_1, N_2, and N_3 are the populations of level 1, 2, and 3, respectively, and $A_i = 1/\tau_i$ is the transition rate for i^{th} level ($i = 1, 3$) and τ_i is the lifetime of the i^{th} level.

Since the model is for a pulsed amplifier, the following assumptions can be made:

- The pumping rate (P) is negligible over the duration of the pulse being amplified.
- τ_3 is sufficiently short enough that the population N_3 is negligible.
- The lasing transition between N_2 and N_1 is the only mechanism that depopulates N_2.
- The absorption (σ_{abs}) and stimulated emission (σ) cross-sections are different and related to each other by the g-factor ($g = \sigma_{abs}/\sigma$).

Using these assumptions, the Frantz-Nodvik equations can be modified to yield equations 3.4, 3.5, and 3.6.

$$\frac{\partial n}{\partial t} + c\frac{\partial n}{\partial z} = \sigma c n (N_2 - g N_1) \tag{3.4}$$

$$\frac{\partial N_1}{\partial t} = \sigma c n (N_2 - g N_1) - \frac{N_1}{\tau_1} \tag{3.5}$$

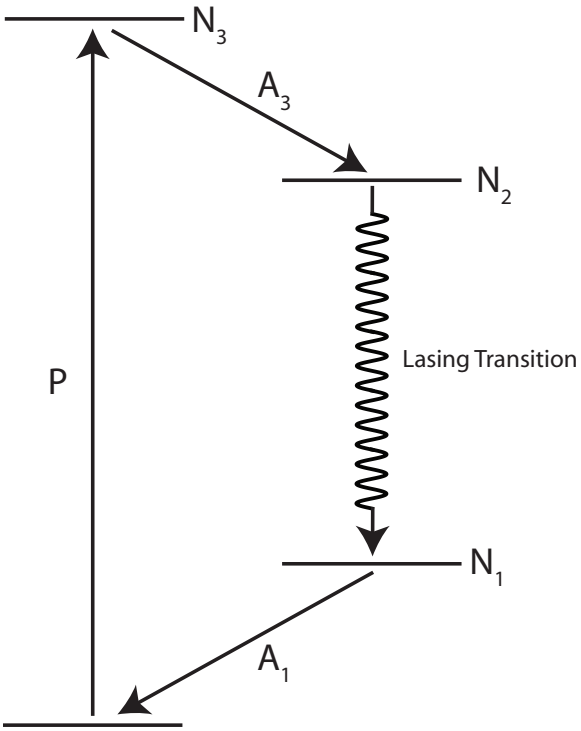

Figure 3.8: Four level energy diagram used to model the Ti:sapphire amplifier. The pumping rate (P), transition rates (A_1 and A_3) and level populations (N_1, N_2 and N_3) are shown.

$$\frac{\partial N_2}{\partial t} = -\sigma c n (N_2 - g N_1) \tag{3.6}$$

where n is the photon density, t is time, c is the speed of light in sapphire, z is the length of sapphire used, σ is the stimulated emission cross-section, g is the ratio of absorption cross-section to stimulated emission cross-section, and N_1, N_2 and τ_1 are defined above. Making the transformation of variables:

$$x = z \tag{3.7}$$

$$\tau = t - z/c \tag{3.8}$$

yields a simpler set of equations:

$$\frac{\partial n}{\partial x} = \sigma c n (N_2 - g N_1) \tag{3.9}$$

$$\frac{\partial N_1}{\partial \tau} = \sigma c n (N_2 - g N_1) - \frac{N_1}{\tau_1} \tag{3.10}$$

$$\frac{\partial N_2}{\partial \tau} = -\sigma c n (N_2 - g N_1) \tag{3.11}$$

The output power of the amplifier can be determined by numerically solving these equations, subject to the following constraints:

- The seed pulse makes 9 passes through the amplifier.
- The pumping rate is significant between passes of the amplifier and results in the populations $N_2 = N_0$ and $N_1 = 0$ before the seed enters the amplifier on each pass. N_0 is the initial population inversion, determined by the measured small signal, single pass gain.
- After each pass through the amplifier, the seed pulse energy is decreased by 10% to account for the mask in the amplifier.

- The effect of dispersion on the seed pulse (i.e. shortening of the seed pulse) is taken into account.

Since both g and τ_1 are unknown, these are the only fit variables in our calculation and the simulation is run for a large number of (g, τ_1) pairs. For each (g, τ_1) pair, a range of seed pulse widths is simulated. The results are then compared to the measured data to determine which pairs provide the best agreement with the data. The results of the simulation that provide the best agreement with the experimental data are shown in Figure 3.9.

3.2.2.2 Experimental results

As described above, the new ring design virtually eliminated astigmatism in the ring. After measuring the beam quality out of the amplifier with the old and new ring designs, the two stage stretcher was replaced with a one stage, grism stretcher (supplied by HORIBA Jobin-Yvon Inc.). Before any amplifier measurements were taken with the grism stretcher, the stretched pulse durations were measured using a 60 GHz fast photodiode and a sampling oscilloscope to generate a calibration curve for the grisms. After calibration, the uncompressed, amplified output power was measured as a function of seed pulse duration by adjusting the grism separation (Fig. 3.9). The output power varies greatly with input seed pulse duration, reaching a maximum around 22 $\pm$ 3 ps. The results of the simulation described above and the measured data are in very good agreement when a lower state lifetime in the range of 0.25–5 ps is assumed. The variation in the lifetime is due to the unknown ratio of the upper to lower level degeneracy in Ti:sapphire (g). Because both g and τ_1 are constants that depend only on the material properties, the product of the two should be a constant as well. When the product of this degeneracy ratio with the lower state lifetime ($g\tau_1$) is 25, and τ_1 is 0.25–5 ps, the simulation results provide a best fit with the data. In addition to running the simulation with the seed pulse widths obtainable with the grism stretcher, much longer

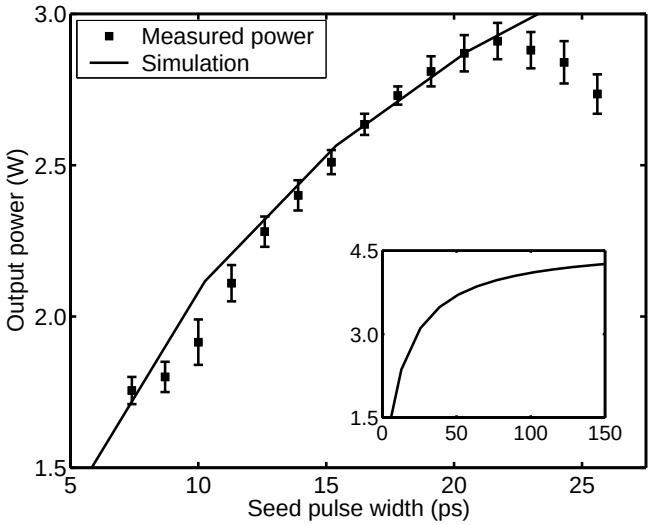

(a)

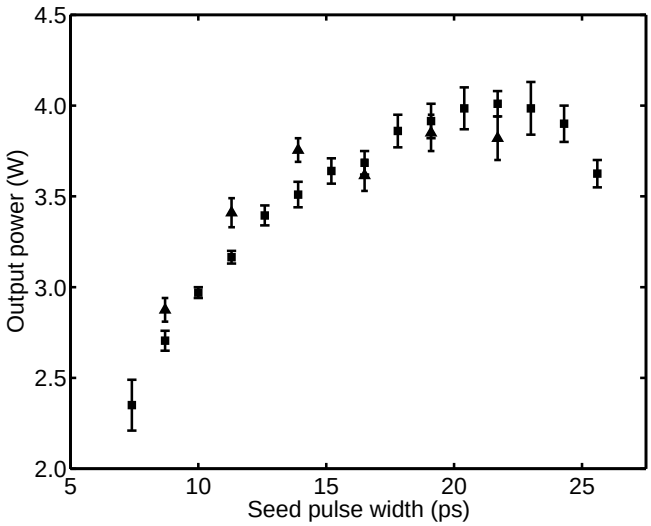

(b)

Figure 3.9: Power before compression as a function of seed pulse length for (a) 10 kHz repetition rate and (b) 15 kHz repetition rate. Data was taken while only adjusting grism separation (squares) and while adjusting both grism separation and timing between pump and seed pulses (triangles). Simulation results are shown as solid line in (a) and in (a) inset, which extrapolates the model to estimate the pulse duration required for efficient energy extraction from Ti:sapphire.

pulse widths, up to 150 ps, were simulated. The simulation (Fig. 3.9a inset) shows that the output energy starts to saturate at a seed pulse width of ∼75 ps. For the measured data, the drop in efficiency at longer pulse lengths is an artifact of the experimental setup. The gratings of the grisms are only one inch square, which limited the amount of stretch that could be applied before spectral clipping of the amplified spectrum was observed (Fig. 3.10).

The maximum output pulse energy of the amplifier is 290 μJ at 10 kHz and 270 μJ at 15 kHz, with a pulse-to-pulse intensity stability of 1.7% and 3.0% rms at 10 and 15 kHz, respectively. The pulse-to-pulse stability was measured with a photodiode, boxcar, and digitizing electronics. The integrated intensity of each pulse was measured for 1, 10, 30, and 60 seconds and the rms error was calculated for each integration time. The stability measurements reported above are the average of the four measured values. The stability is worse at higher repetition rates due to a longer pump pulse duration. At 10 kHz, the duration of the pump pulse is ∼150 ns. This increases to ∼200 ns at 15 kHz, allowing more time for amplified spontaneous emission (ASE) to build up and lower the effective gain. At 15 kHz, the grism separation was adjusted and the relative timing of the pump and seed pulses was reoptimized (Fig. 3.9b, triangles). This resulted in slightly higher energies at the shorter seed pulse lengths.

The pulse duration from the amplifier was measured using frequency resolved optical gating based on second harmonic generation (SHG–FROG). Figure 3.11 shows the reconstructed pulse and phase, with a FWHM of 36 ± 1 fs, while Figure 3.12 shows the measured and reconstructed FROG traces. The transform limit of the amplified spectrum is ∼28 fs. FROG measurements taken at different radial positions of the beam profile reconstruct to the same value, showing that the center and edges of the divergent beam do not traverse significantly different amounts of material. The output beam quality is good, as can be seen by the M^2 of the beam (Fig. 3.7b), which was measured to be 1.18 and 1.26 in the x- and y-directions, respectively. Nonlinear effects,

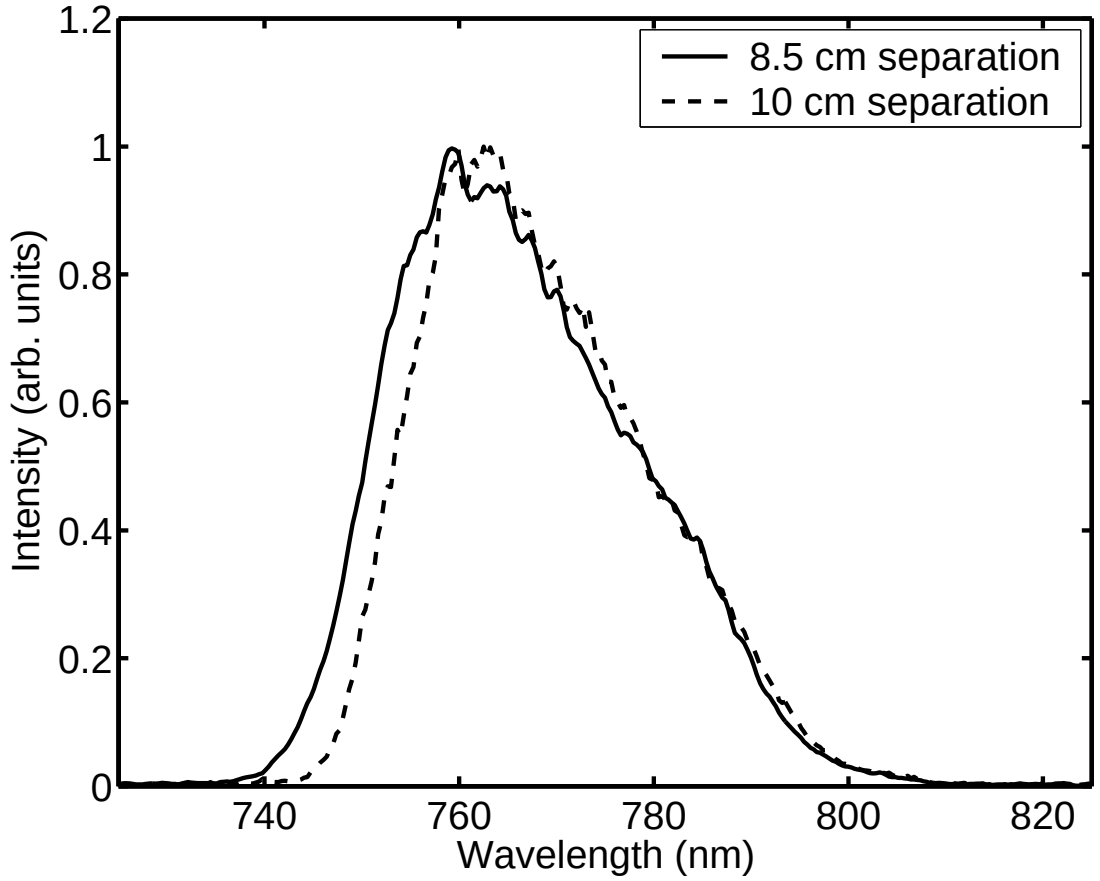

Figure 3.10: Measured amplified spectra at grism separations of 8.5 cm (solid) and 10 cm (dashed) showing evidence of spectral clipping. At larger grism separations the shorter wavelengths are clipped due to the small physical size of the grisms. Grism separations of 8.5 cm and 10 cm correspond to stretched pulse lengths of 22 ps and 25 ps, respectively.

such as B-integral, would distort the beam profile, leading to a large M^2 value. Since the M^2 is close to unity in both directions, it can be concluded that nonlinear effects in the compressor are negligible. This is consistent with calculations that the B-integral should be less than 0.5 in this configuration.

3.2.3 Conclusion

In conclusion, a laser amplifier system based on downchirped pulse amplification that can be scaled to medium energies and very high repetition rates has been demonstrated. Despite various other laser amplifier systems having been demonstrated in the 10–100 kHz range, this system is the only one that encompasses all three criteria for a versatile, high repetition rate system: >10 kHz repetition rate, sub-40 fs pulses, and >100 μJ pulse energy. The modified design makes use of a tighter focus amplifier ring capable of achieving saturated gain at lower pump pulse energies. Due to the tighter focusing, a new multipass ring design was necessary to greatly reduce accumulated astigmatism. This new ring design produces an amplified beam with virtually no astigmatism and excellent beam quality ($M^2 < 1.3$ in both the x- and y-direction). In addition to the new ring design, this amplifier used all-reflective grisms as the stretcher, greatly simplifying the amplifier. The grisms allowed the output power to be measured over a large range of pulse widths ($\sim$ 10–30 ps). These measurements, along with a detailed simulation of the amplifier, permitted the calculation of a range of values for the lower state lifetime of the lasing transition of Ti:sapphire. This work resulted in a compact, single stage amplifier that is scalable to 40 kHz or greater repetition rate. The output of the amplifier is a 36 fs, $\sim$300 μJ pulse, with excellent beam quality and pulse-to-pulse stability. Such a system will provide a pulse energy and peak power sufficient for many applications, at higher pulse repetition frequencies than are currently available.

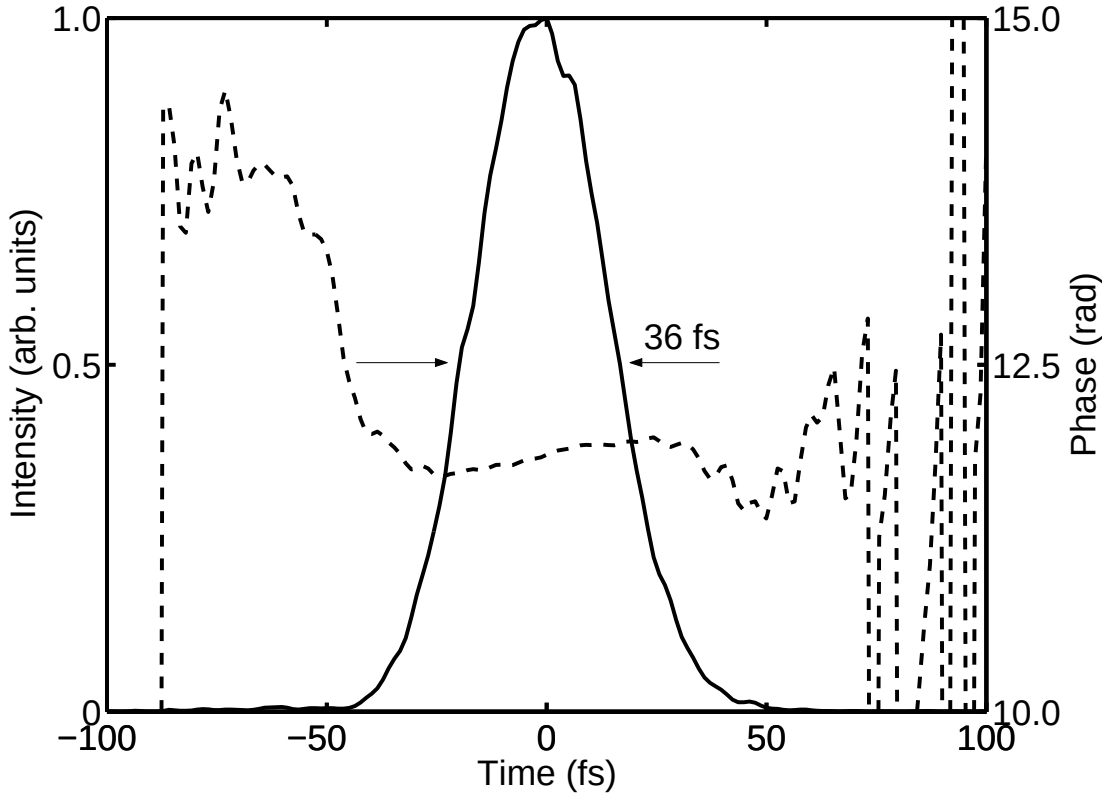

Figure 3.11: Temporal profile (solid) and phase (dotted) of amplified pulse as measured with FROG showing a FWHM of 36 fs.

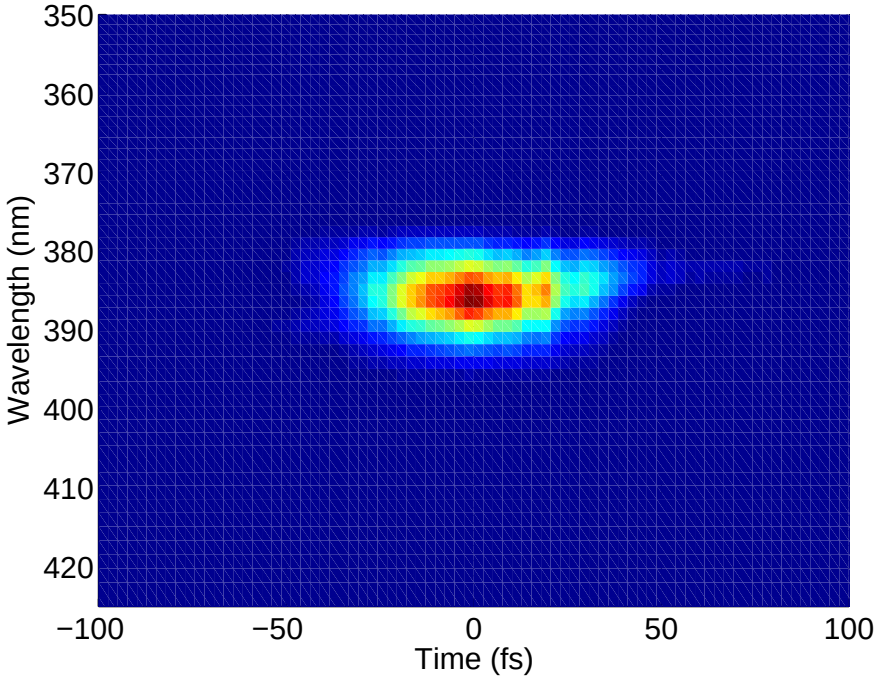

(a)

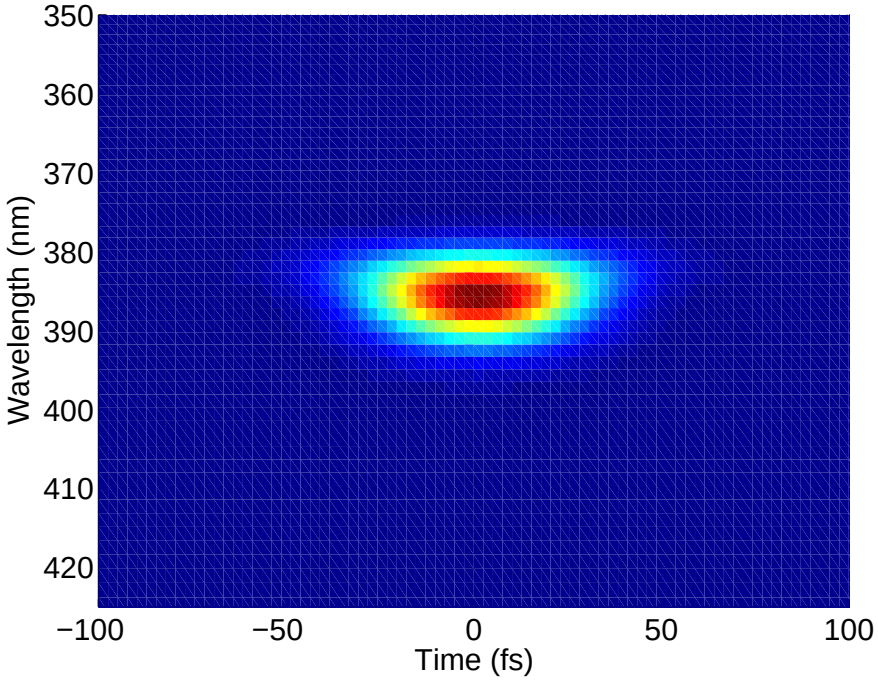

(b)

Figure 3.12: Measured and reconstructed FROG traces for the 36 fs pulse shown in Fig. 3.11.

Chapter 4

High-order harmonic generation and plasma waveguides

4.1 Introduction

Recent years have shown an increased interest in the extreme-ultraviolet (EUV) and soft x-ray regions of the electromagnetic spectrum for a variety of reasons. First, this light allows for the imaging of smaller features since the resolution of an optical system is proportional to the wavelength of the light. Therefore, EUV and soft x-ray light can improve the resolution of an optical system by several orders of magnitude when compared with visible imaging. Second, EUV and soft x-ray light allows for the writing of smaller patterns via photolithography, for similar reasons. Lastly, most elements have core shell absorption edges in this region of the spectrum, so using EUV and soft x-ray radiation allows for chemical and elemental sensitivity in most experiments.

Unfortunately, it can be difficult to generate light in this region of the spectrum. There are three main options for EUV sources: synchrotrons, EUV lasers, and high harmonic generation. Synchrotrons generate tunable radiation over a very large range of wavelengths, but require stadium sized facilities. In addition, experimental beam lines are limited at synchrotrons, so this is not a solution for most experimentalists. The second main source is the EUV laser. These devices are compact, usually occupying less than 1 m^2 of optical table space, and produce EUV pulses with high energy. The drawbacks to EUV lasers is that they produce long (ns) pulses, making them unsuitable for time-resolved studies, and the wavelength selection is limited to the lasing transitions

of ions.

The last viable EUV source is high harmonic generation. High harmonic generation requires a compact, high-power, short pulse laser system and a small (a few cm) generation cell, making this a table-top EUV source. These HHG sources produce extremely short pulses with low energy and are tunable from the VUV to the keV region of the electromagnetic spectrum. These characteristics make HHG the ideal method for the efficient generation of short wavelength light. Unfortunately, there are three roadblocks preventing the realization of a short pulse, tunable, efficient HHG source: ionization loss, ionization induced defocusing, and phasematching, all of which will be described later in this chapter. Use of a plasma waveguide can reduce or eliminate the first two of these roadblocks.

This chapter will provide the background and theoretical framework of high-order harmonic generation (HHG) and plasma waveguides that are needed to understand the results of the subsequent chapter.

4.2 High-order harmonic generation

4.2.1 What is HHG?

High-order harmonic generation (HHG) is a term used to describe the nonlinear interaction between an intense laser pulse and a medium (usually a gas) that results in the generation of harmonics of the driving laser field. It can be distinguished from low-order (2^{nd}, 3^{rd}, etc.) harmonic generation in that it cannot be described by perturbation theory. There are three significant characteristics that are unique to HHG spectra:

(1) Intense low-order harmonics where the intensity follows perturbation theory (i.e. the harmonic intensity is proportional to I^q where I is the driving laser intensity and q is the harmonic order).

(2) A long plateau of harmonics whose intensities are approximately equal.

(3) A very sharp cutoff where the HHG signal drops rapidly.

These characteristics are observed in all HHG experiments and have been validated by current HHG theory.

4.2.2 History of HHG

HHG was first observed by McPherson *et. al*, in 1987 [20] when they observed up to the 17^{th} harmonic of a 248 nm driving laser in neon gas. The published HHG spectrum [20] shows the low-order intensity drop as a function of harmonic order and the plateau of relatively uniform intensity harmonics that are indicative of high-harmonic generation.

Their work was followed by the demonstration of high-order harmonic generation in rare gases by IR ($\sim$1064 nm) [21, 73–76] and near-IR (800 nm) laser light [77], by shorter ($<$ 30 fs) pulses [78, 79], by phase matched generation in a hollow waveguide [80, 81], and by self-guided laser beams [82, 83]. Coherent control of the harmonic generation process has been demonstrated [84–86] as well as generation in noble gas-like ions [87], noble gas ions [88] and preformed, underdense plasmas [89]. Recent work has demonstrated the spatial coherence of high-order harmonics generated in a waveguide [17], HHG pulses with energy in the μJ range [90], quasi-phase matching techniques in the soft x-ray region [91], and the generation of harmonics with $\sim$ keV energy [92, 93].

In addition to the large body of experimental work on high harmonic generation, there has been significant progress in the theory of high harmonic generation using quantum mechanical models [22, 23, 94–104], semi-classical models [22, 23, 99, 105], and models based on Volkov states [106]. Although a fully quantum mechanical model is needed to observe the nuances in the high harmonic generation process, the semi-classical model predicts the main features of HHG outlined above.

4.2.3 Theory of high-order harmonic generation

The spectrum that is observed from the high harmonic generation process is the result of two separate processes: generation of harmonic light from a single atom and the subsequent propagation in the medium. The single atom response is accurately predicted by a semi-classical model while the propagation effects are predicted by classical electrodynamics.

4.2.3.1 Single atom response

The semi-classical model [22, 99] describes the single atom response as a three step process:

(1) Ionization of the atom/ion.

(2) Classical acceleration of the free electron by the laser field.

(3) Recombination of the electron.

Each of the three steps above has an associated probability. The harmonic emission from a single atom or ion is calculated by multiplying the probabilities of the three steps.

The first step in the HHG process is the ionization of the electron. There are three ways in which an atom can be ionized: multiphoton ionization, tunnel ionization, and above-barrier ionization (Fig. 4.1). The Keldysh parameter (Eq. 4.1) is defined as the ratio of the laser frequency to the tunneling frequency and determines which mechanism is dominant.

$$\gamma = \frac{\omega_{laser}}{\omega_{tunnel}} = \sqrt{\frac{I_p}{2\ U_p}}, \tag{4.1}$$

where I_p is the ionization potential of the atom/ion being ionized and U_p is the ponderomotive energy. The ponderomotive energy is the classical kinetic energy gained by

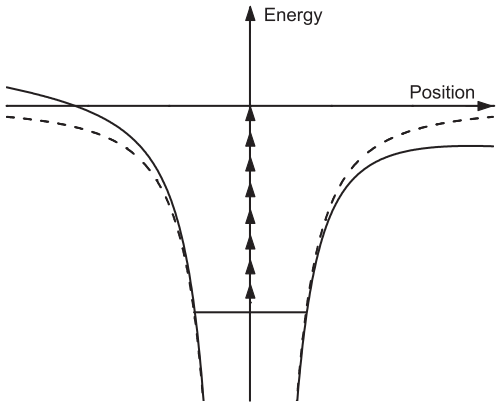

(a)

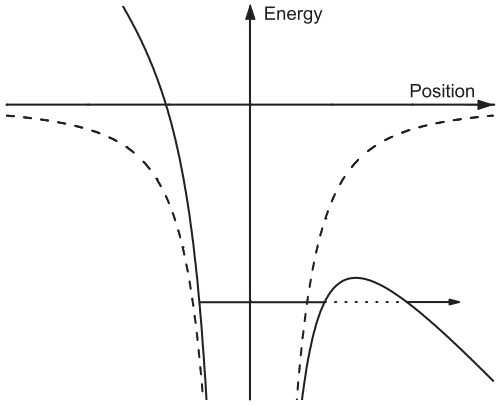

(b)

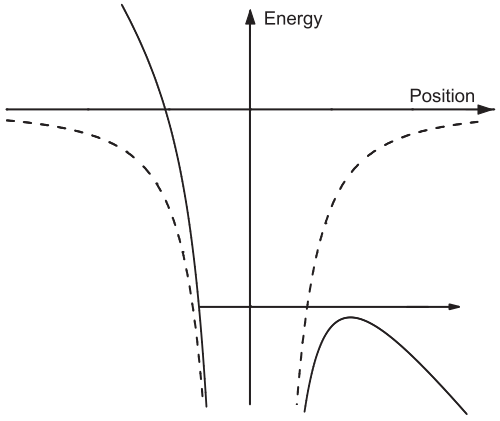

(c)

Figure 4.1: Plots of the Coulomb potential (dotted line) and Coulomb potential modified by the laser field (solid line) for (a) multiphoton ionization ($\gamma > 1$), (b) tunnel ionization ($\gamma < 1$), and (c) above-barrier ionization ($\gamma << 1$).

an electron in an oscillating field and is given by Eq. 4.2.

$$U_p = \frac{e^2 E_0^2}{4m\omega^2} = \frac{e^2 c\mu_0 I}{2m\omega^2}, \tag{4.2}$$

where e is the electron charge, E_0 is the electric field strength, m is the electron mass, ω is the laser angular frequency, c is the speed of light in a vacuum, μ_0 is the permeability of free space, and I is the laser intensity. In terms of the laser intensity and wavelength, the ponderomotive energy, in electronvolts, is given by $U_p \approx 9.33\ 10^{-14}\ I\ \lambda^2$, with intensity in W/cm^2 and wavelength in μm.

When the laser intensity is small, $\gamma >> 1$ which indicates that multiphoton ionization is dominant. In this regime, the effective potential is only slightly modified from the Coulomb potential by the laser field and ionization occurs by the absorption of N photons (Fig. 4.1(a)). In this multiphoton regime, the ionization can be treated as a perturbative process. At larger laser intensities, $\gamma < 1$ and tunnel ionization becomes the dominant mechanism (Fig. 4.1(b)). In this regime, the effective potential is severely distorted by the laser field, allowing the electron to tunnel out of the atom/ion. For the typical situation of neutral argon ($I_p = 15.76$ eV) interacting with an 800 nm laser, tunnel ionization becomes the dominant mechanism for intensities $> 10^{14}$ W/cm^2. Typical intensities in HHG experiments are $\sim\ 10^{14}$–10^{16} W/cm^2, making tunnel ionization the dominant ionization mechanism. An expression for the tunnel ionization probability of an atom or ion in an oscillating field was developed by Ammosov, Delone, and Kraĭnov [107]. This tunnel ionization probability (also known as the ADK ionization rate or, simply, the ADK rate), is derived using a quasi-static approximation where the DC tunneling rates are used for the AC field. This approximation is valid when the field is approximately constant during the tunneling time (i.e. the tunneling time is less than the oscillation period). This is true when $\gamma \leq 1/2$. For very short and very intense optical pulses, the Coulomb barrier may be suppressed below the ionization potential

while there still exists a large population in the ground state (Fig. 4.1(c)). This is called above-barrier ionization and occurs for field strengths in excess of the critical field strength:

$$E_{cr} = \frac{\pi \epsilon_0 I_p^2}{Ze^3} \tag{4.3}$$

where ϵ_0 is the permittivity of free space, I_p is the ionization potential of the atom/ion, Z is the charge after ionization, and e is the charge on the electron. For fields above this critical field, the ADK rates may overestimate the ionization rate [79, 108]. This overestimate is small for longer pulses ($> 20fs$) and increases as the pulses approach the single-cycle limit. But the overestimate of the fractional population is still less than a factor of 2 for pulses close to a single cycle [79].

The ADK rate from the ground state is given in SI units by [79]:

$$\omega(t) = \omega_p |C_{n^*}|^2 \left(\frac{4\omega_p}{\omega_t}\right)^{2n^*-1} \exp\left(-\frac{4\omega_p}{3\omega_t}\right) \tag{4.4}$$

with

$$\begin{aligned} \omega_p &= \frac{I_p}{\hbar} \\ \omega_t &= \frac{eE_l(t)}{(2mI_p)^{1/2}} \\ n^* &= Z\left(\frac{I_{ph}}{I_p}\right)^{1/2} \\ |C_{n^*}|^2 &= 2^{2n^*}[n^*\Gamma(n^*+1)\Gamma(n^*)]^{-1}. \end{aligned}$$

In the above equations, I_p is the ionization potential of the atom or ion, $\hbar$ is Planck's constant divided by 2π, e is the charge of the electron, $E_l(t)$ is the laser electric field, m is the mass of the electron, Z is the ion charge after tunnel ionization, I_{ph} is the ionization potential of the hydrogen atom, and $\Gamma(x)$ is the Gamma function. The fraction of ionized atoms/ions can be calculated by

$$n(t) = 1 - \exp\left[-\int_{-\infty}^{t} \omega(t')dt'\right]. \tag{4.5}$$

Figure 4.2 shows the result of some sample calculations. The fractional populations of the first few ionization states of argon as well as the actual ADK rates, weighted by the fractional populations, are shown. These calculations correspond to a peak laser intensity of 10^{15} W/cm^2, a full-width half-maximum (FWHM) pulse duration of 25 fs, and a central laser wavelength of 800 nm.

The second step of the three step model is the acceleration of the electron in the laser field. In this step of the model, the electron and field, due to the large number of states available to the electron, may be treated classically, with the electric field given by $E(t) = E_0\cos(\omega t)\hat{\mathbf{e}}_x + \alpha E_0\sin(\omega t)\hat{\mathbf{e}}_y$, where E_0 is the field strength, ω is the laser frequency and α is the ellipticity (0 for linearly polarized light, ± 1 for circularly polarized light), and the electron's equations of motion (Eqs. 4.6–4.9) are obtained by integrating $F(t) = eE(t)$ (e is the charge on the electron).

$$v_x(t) = \frac{eE_0}{\omega m}\sin(\omega t) + v_{0x} \tag{4.6}$$

$$v_y(t) = -\frac{\alpha eE_0}{\omega m}\cos(\omega t) + v_{0y} \tag{4.7}$$

$$x(t) = -\frac{eE_0}{\omega^2 m}\cos(\omega t) + v_{0x}t + x_0 \tag{4.8}$$

$$y(t) = -\frac{\alpha eE_0}{\omega^2 m}\sin(\omega t) + v_{0y}t + y_0 \tag{4.9}$$

where v_{0x}, v_{0y}, x_0, and y_0 can be evaluated from the initial conditions of the tunneling electron. For the purposes of the simulation, when the electron tunnels out of the barrier, it is assumed to enter the continuum with zero velocity ($v_x(0) = v_y(0) = 0$) at the position where the effective potential (Coulomb potential + laser potential) equals the ionization potential. Typical values of this position are a few Å, whereas the electron's excursion in the field is a few nm, so this value is considered negligible and the electron is considered to be at the origin when it tunnels into the continuum. From Eqs 4.6–4.9,

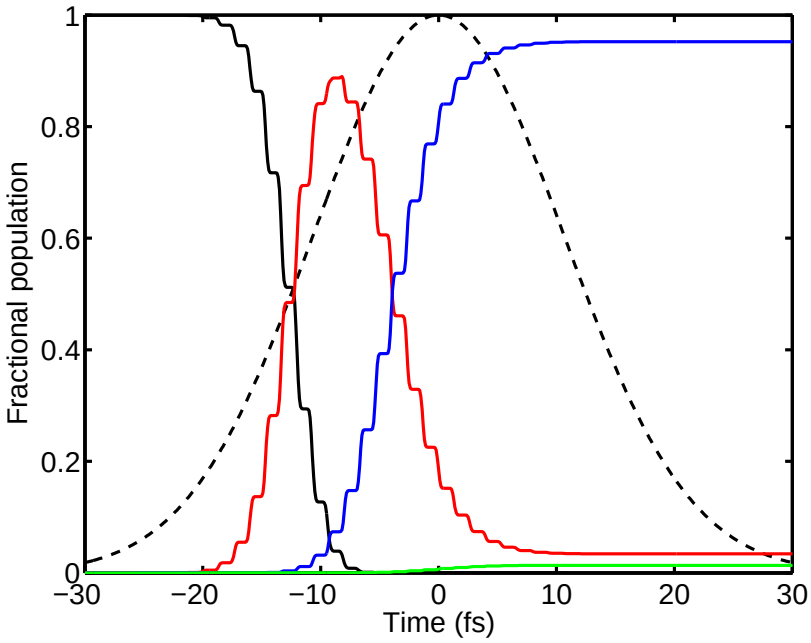

(a)

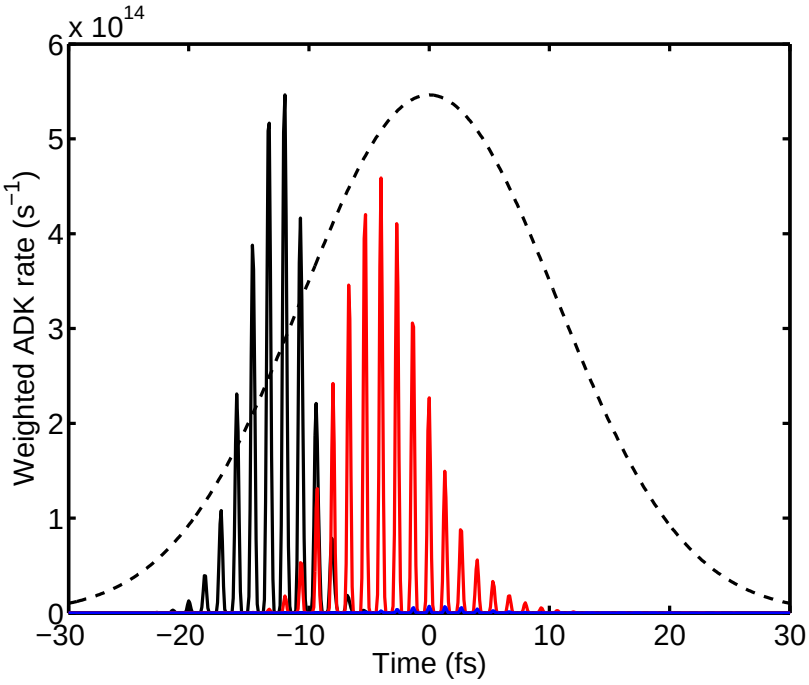

(b)

Figure 4.2: (a) Fractional populations of neutral Ar (black), Ar^+ (red), Ar^{2+} (blue), and Ar^{3+} (green). (b) ADK ionization rates for neutral Ar (black), Ar^+ (red), and Ar^{2+} (blue), weighted by their respective fractional populations. The temporal pulse envelope (black dotted) is shown for reference. These calculations correspond to a peak laser intensity of 10^{15} W/cm^2, a full-width half-maximum (FWHM) pulse duration of 25 fs, and a central laser wavelength of 800 nm.

it can be seen that the electron will not return to the position of the ion if the light is circularly polarized ($\alpha = \pm 1$). Since it is the process of high harmonic generation that is of interest, an electron must return to the parent ion in order to emit a high energy photon. Therefore only linearly polarized light will be considered for the remainder of this chapter.

In a linearly polarized laser field, the electron's energy, upon return to the parent ion, can be calculated as a function of when the electron tunnels through the barrier. Even though this step of the model treats the electron classically, the quantum nature of the electron cannot be completely ignored. As the electron propagates in the laser field, the electron wavepacket will spread in a direction transverse to its motion and at a rate of ~ 1.5 Å/fs [99]. Atomic sizes are approximately 1-2 Å, so after 2.6 fs (i.e. one laser cycle at 800 nm) the electron wavepacket is larger than the parent ion. This wavepacket spreading reduces the probability of recombination and this probability is lower the longer the electron is in the laser field. Therefore the greatest recombination probability, and thus the largest contribution to the HHG emission, is for electrons that return to the parent ion within one cycle. For this reason, the following analysis is restricted to electrons that return within one laser cycle.

Figure 4.3 shows the energy of the returning electron, in units of the ponderomotive potential (U_p), as a function of the phase of the laser pulse when the electron tunnels. The maximum energy that an electron can gain in the laser field is $\approx 3.17U_p$, which occurs when the electron is released into the field at $\approx 18°$. When the release phase is greater than 90°, the electron never returns to the position of the parent ion. Electrons that are emitted between 0 and 90° phase will return to the ion in the subsequent laser period following ionization. Figure 4.4 shows the probability per cycle per eV that an electron will tunnel ionize from Ar^+, accelerate in the laser field, and return to the parent ion with an energy E for a laser cycle with a peak intensity of 10^{15} W/cm^2. It can be easily seen from Figs. 4.3 and 4.4, that an electron cannot gain more than

3.17 U_p of energy in the laser field. It is possible for an electron to gain more energy than this, but that requires the electron to stay in the laser field longer than one cycle or that the electron is released at a phase of $\approx 180^{\circ}$, where the ionization probability is very low [22]. Therefore, if the electron recombines with the parent ion in the ground state and emits a photon, conservation of energy dictates that the photon cannot have more energy than $I_p + 3.17U_p$. This is the well known high harmonic generation cutoff rule (Eq. 4.10) and it determines the maximum photon energy that can be emitted in the high harmonic generation process, according to the semi-classical model. In actuality, this cutoff rule is not as simple as described here. This semi-classical model ignores many important quantum mechanical effects. When these effects are taken into account, a more complicated cutoff rule is derived [23]. Also, this cutoff rule is for the single-atom response. There are a variety of macroscopic effects that prevent the observed spectra from following this rule exactly [75].

$$h\nu_{max} = I_p + 3.17U_p, \tag{4.10}$$

where h is Planck's constant and ν_{max} is the maximum harmonic frequency that can be emitted.

The last step in the semi-classical model is the recombination process. An electron returning to the parent ion can interact with this ion in a number of ways. The electron can collisionally ionize the ion, scatter elastically, or emit a photon via recombination with the ion. The emission of light upon recombination can be calculated by the dipole operator $d(t) = \langle\psi|e\ r(t)|\psi\rangle$. A complete description of how to evaluate the dipole operator based on the semi-classical model of high harmonic generation is given in Ref. [99]. The phase of the dipole operator, known as the intrinsic phase, plays a very important role in the high harmonic generation process. This phase, given by $\exp[-iS(t_i, t_f)]$, where $S(t_i, t_f)$ is the quasi-classical action (Eq. 4.11) [109], is the

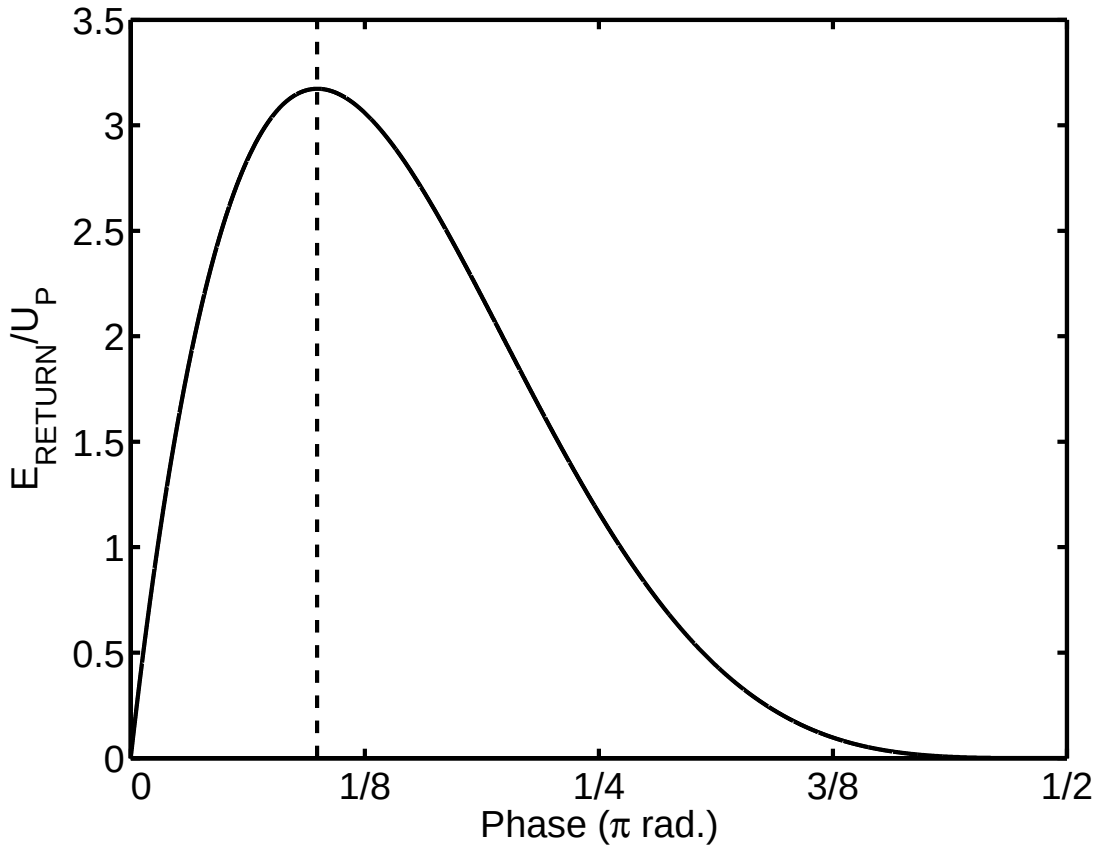

Figure 4.3: Energy of the returning electron as a function of laser phase at the time of tunneling. The dotted line shows the position of the peak of the curve ($\approx 18°$).

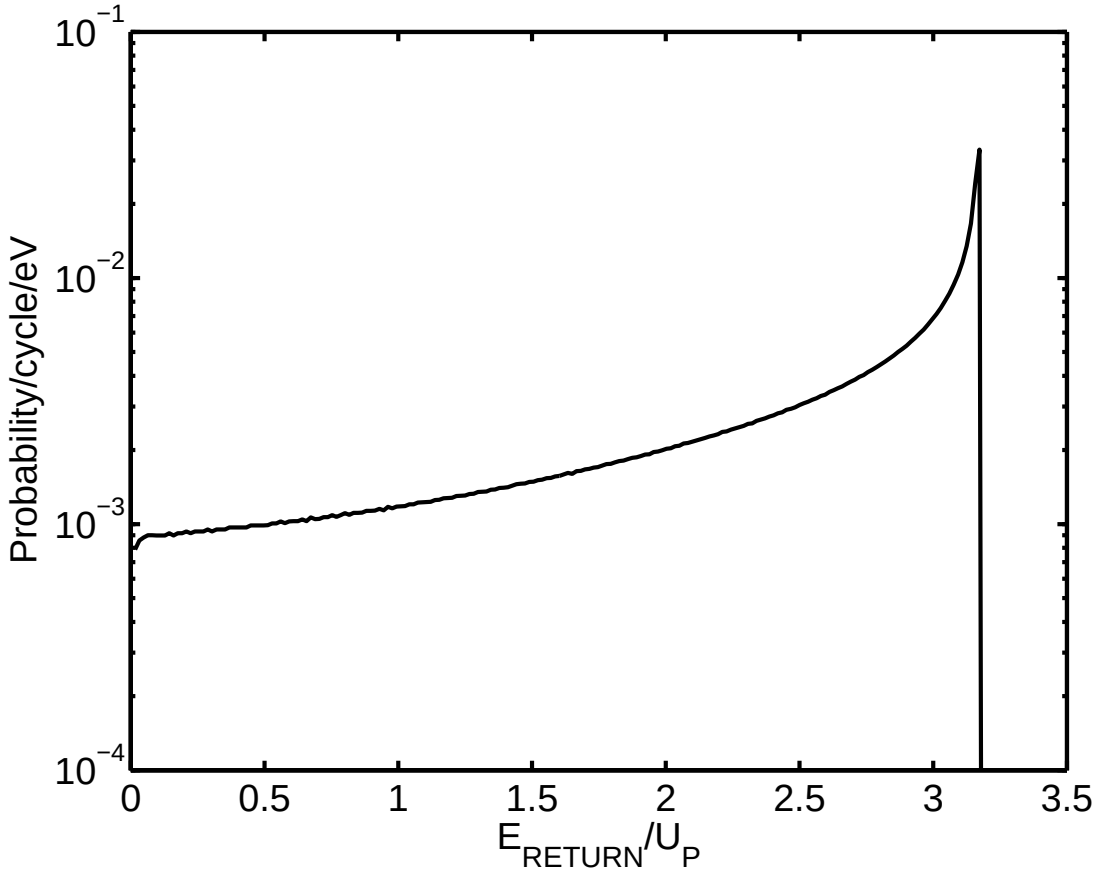

Figure 4.4: Probability distribution for electrons, which are ionized and return to the position of the nucleus, to have a given energy upon return. These calculations correspond to the probability for an electron ionized from an Ar^+ ion with a peak laser intensity of 10^{15} W/cm^2 and a central laser wavelength of 800 nm.

phase accumulated by the electron in the laser field.

$$S(t_i, t_f) = \int_{t_i}^{t_f} dt'' \left(\frac{[\mathbf{p}(t_i, t_f) - \mathbf{A}(t'')]^2}{2} + I_p \right) \tag{4.11}$$

where t_i and t_f are the ionization and recombination times, respectively, $\mathbf{p}(t_i, t_f)$ is the momentum corresponding to an electron ionized at t_i and recombined at t_f, $\mathbf{A}$ is the vector potential of the laser field, and I_p is the ionization potential of the atom/ion. The stationary points of this phase determine which trajectories have the most significant contribution to the dipole moment. For a given harmonic, the dominant contribution comes from two trajectories: one with a short return time $(t_f - t_i)$ and one with a long return time. These correspond to the two classical trajectories that give rise to an electron with a specific energy (Fig. 4.3). Not only does the quasi-classical action determine which trajectories are significant, it also determines the phase of the emitted harmonic [110]:

$$\Phi_{at} = q\omega t_f - S(t_i, t_f)/\hbar \tag{4.12}$$

where q is the harmonic order and ω is the driving laser angular frequency. Equation 4.12 shows that the phase of the emitted harmonics is intensity dependent. It should be possible to adjust the phase relation between the driving field and the harmonic field by modulating the laser intensity, thus affecting phase matching (described below).

The simulated single atom response is proportional to the absolute square of the Fourier Transform of the dipole operator ($d(\omega) = F\{d(t)\}$). Plots of $|d(\omega)|^2$ shown in both [22] and [99] show the same qualitative behavior of high harmonic generation: perturbative behavior for the low order harmonics, a long plateau, and a sharp cutoff. Also, this semiclassical model has been validated by more elaborate, fully quantum mechanical models [22, 23]. Tempea and Brabec [105] give a concise explanation of this single atom dipole moment as the product of three probability amplitudes (one for

each of the three steps), as well as providing equations for each of the three probability amplitudes, in atomic units.

The three-step process will repeat itself for every half cycle of the laser pulse. Therefore, in an isotropic material (such as a gas) this will produce a harmonic spectrum of odd harmonics of the driving field only. If the symmetry is broken, for example, by introducing a second pulse of a different wavelength, it is possible to generate all the harmonics of the driving field [111].

4.2.3.2 Macroscopic effects

Macroscopic effects play a large role in the signal observed from high harmonic generation. The four main macroscopic effects that influence the observed signal are self-phase modulation of the driving laser field, loss of laser energy due to ionization of the medium, plasma-induced defocusing, and phase matching of the driving laser and the harmonic signal.

Self-phase modulation (SPM) is a process where the spectrum of the laser pulse is changed due to the interaction of the laser with the medium. More specifically, the laser pulse, via effects such as the Kerr effect, causes a change in the index of refraction of the medium through which it is propagating. Since this change in index is caused by the pulse, it is necessarily a function of time and a time varying index of refraction modulates the phase of the laser pulse. For typical ultrashort pulses (< 30 fs), the phase modulation is significant since the intensity change is very rapid. This modulation gives rise to a change in the instantaneous frequency of the laser and, consequently, a change in the laser spectrum. There are two mechanisms by which a laser pulse can change the index of refraction of a material.

The first mechanism is caused by the intensity dependence of the index of refraction. The strength of this dependence is called the nonlinear index and is denoted n_2. With this dependence, the full index can be written as

$$n(t) = n_0 + n_2 I(t), \tag{4.13}$$

where n_0 is the standard index of refraction and $I(t)$ is the laser pulse intensity. The phase of a laser pulse propagating through a transparent material is given by

$$\phi(t) = \omega_0 t - \frac{2\pi n(t) L}{\lambda_0} \tag{4.14}$$

where L is the length of the medium, ω_0 is the central angular frequency and λ_0 is the vacuum laser wavelength. The instantaneous frequency of the pulse is the time derivative of the phase

$$\omega(t) = \frac{d\phi(t)}{dt} = \omega_0 - \frac{2\pi L}{\lambda_0}\frac{dn(t)}{dt} = \omega_0 - \frac{2\pi L n_2}{\lambda_0}\frac{dI(t)}{dt}, \tag{4.15}$$

which clearly shows that the intensity envelope of the pulse changes the spectrum of the pulse. Since most ultrashort pulses are Gaussian in intensity, this type of SPM results in a symmetric broadening of the laser spectrum and is often used to generate sub-5 fs pulses from Ti:sapphire laser systems [112].

The second mechanism for SPM is the rapid ionization of a gaseous medium due to the laser pulse. For peak laser pulse intensities $> 10^{14}\mathrm{W/cm}^2$, the tunnel ionization probability for a gas is very large on the leading edge of the pulse leading to significant fractional ionization per laser cycle on the leading edge. This rapid change in electron density causes a rapid change in the index of refraction. The index of a neutral plasma is dominated by the electron density and can be calculated from Maxwell's Equations in a vacuum:

$$\nabla \cdot E = \frac{\rho}{\epsilon_0} \tag{4.16}$$

$$\nabla \cdot B = 0 \tag{4.17}$$

$$\nabla \times E = -\frac{\partial B}{\partial t} \tag{4.18}$$

$$\nabla \times B = \mu_0 J + \frac{1}{c^2}\frac{\partial E}{\partial t} \tag{4.19}$$

Taking the cross product of Eq. 4.18 yields

$$\nabla \times (\nabla \times E) = -\frac{\partial}{\partial t}(\nabla \times B) \tag{4.20}$$

$$\nabla(\nabla \cdot E) - \nabla^2 E = -\frac{\partial}{\partial t}(\mu_0 J + \frac{1}{c^2}\frac{\partial E}{\partial t}) \tag{4.21}$$

$\nabla \cdot E = 0$ since this derivation assumes a neutral plasma ($\rho = 0$). The current density is due to the motion of the free electrons (Eq. 4.22) and this motion is mainly governed by the electric field of the propagating wave (Eq. 4.23). This leads to the following expression for the time derivative of the current density

$$J \equiv N_e e\dot{r} \tag{4.22}$$

$$m_e\ddot{r} = eE \tag{4.23}$$

$$\frac{\partial J}{\partial t} = N_e e\ddot{r} \tag{4.24}$$

$$\frac{\partial J}{\partial t} = \frac{N_e e^2 E}{m_e} \tag{4.25}$$

where N_e is the electron density, e is the electron charge, $\dot{r}$ is the velocity of the electron, $\ddot{r}$ is the acceleration of the electron, E is the electric field, and m_e is the mass of the electron. Substituting this into Eq. 4.21 and assuming the plasma is illuminated by a plane wave ($E = E_0 e^{i(kx-\omega t)}$) yields the dispersion relation for a neutral plasma

$$-\nabla^2 E = -\frac{\mu_0 N_e e^2 E}{m_e} - \frac{1}{c^2}\frac{\partial^2 E}{\partial t^2} \tag{4.26}$$

$$k^2 E_0 e^{i(kx-\omega t)} = -\frac{\mu_0 N_e e^2}{m_e} E_0 e^{i(kx-\omega t)} + \frac{\omega^2}{c^2} E_0 e^{i(kx-\omega t)} \tag{4.27}$$

$$k^2 = -\frac{\mu_0 N_e e^2}{m_e} + \frac{\omega^2}{c^2} \tag{4.28}$$

$$k^2 = -\frac{N_e e^2}{\epsilon_0 c^2 m_e} + \frac{\omega^2}{c^2} \tag{4.29}$$

$$\left(\frac{k}{\omega}\right)^2 = \frac{1}{c^2}\left(1 - \frac{N_e e^2}{\omega^2 \epsilon_0 m_e}\right) \tag{4.30}$$

The phase velocity of the propagating light is k/ω which is equal to the index of refraction divided by the speed of light ($k/\omega = n/c$). The index of refraction of a plasma can be determined by substituting this into the dispersion relation.

$$\left(\frac{n}{c}\right)^2 = \frac{1}{c^2}\left(1 - \frac{N_e e^2}{\omega^2 \epsilon_0 m_e}\right) \tag{4.31}$$

$$n^2 = 1 - \frac{N_e e^2}{\omega^2 \epsilon_0 m_e} \tag{4.32}$$

$$n = \sqrt{(1 - \frac{N_e e^2}{\omega^2 \epsilon_0 m_e})} \tag{4.33}$$

If the electron density is changing, as is the case during the rising edge of an ionizing laser pulse, the time dependent index of refraction of a plasma is

$$n_p(t) = \sqrt{1 - \frac{\omega_p^2(t)}{\omega^2}} \tag{4.34}$$

$$\omega_p^2(t) = \frac{N_e(t) e^2}{\epsilon_0 m_e} \tag{4.35}$$

where ω is the laser angular frequency, $\omega_p(t)$ is the plasma frequency, $N_e(t)$ is the electron density, and ϵ_0 is the permittivity of free space. By equating the laser frequency and the plasma frequency, we can define the critical density, N_{crit}, as $\frac{\epsilon_0 \omega^2 m_e}{e^2}$. At the critical density, the index goes from real to imaginary and light will no longer propagate in the plasma. Using this definition, Eq. 4.34 becomes

$$n_p(t) = \sqrt{1 - \frac{N_e(t)}{N_{crit}}} \tag{4.36}$$

For 800 nm, $N_{crit} \approx 1.75 \times 10^{21}$ cm^{-3}. In most cases, $N_{crit} >> N_e$, so Eq. 4.36 can be rewritten as

$$n_p(t) \approx 1 - \frac{N_e(t)}{2N_{crit}} \tag{4.37}$$

Therefore, the total index of refraction for a gas in the process of being ionized by a laser pulse is

$$n(t) = (1 - \eta(t)) \left(1 + \frac{P}{P_{atm}}\delta_n\right) + \eta(t) \left(1 - \frac{PN_{atm}}{2P_{atm}N_{crit}}\right) \tag{4.38}$$

where $\eta(t)$ is the fractional level of ionization, P is the gas pressure, P_{atm} is atmospheric pressure, $\delta_n = n_{gas} - 1$ is the deviation of the neutral gas index of refraction from that of a vacuum, and N_{atm} is the gas density at atmospheric pressure. The instantaneous frequency of the laser pulse can be calculated as for Eq. 4.15:

$$\begin{aligned} \omega(t) &= \frac{d\phi(t)}{dt} \\ &= \omega_0 - \frac{2\pi L}{\lambda_0}\frac{dn(t)}{dt} \\ &= \omega_0 + \frac{2\pi L}{\lambda_0}\frac{d\eta(t)}{dt}\left(\frac{P}{P_{atm}}\delta_n + \frac{PN_{atm}}{2P_{atm}N_{crit}}\right) \end{aligned} \tag{4.39}$$

Since the fractional electron population only increases on the rising edge of the pulse, this type of SPM introduces a blueshift in the laser frequency.

The next macroscopic effect that can influence the observed harmonic spectrum is the loss of pulse energy due to ionization of the gas. As a laser pulse propagates through a gas (either in free space or a waveguide), it will ionize the gas if the intensity is high enough. This ionization causes the pulse to lose energy as it propagates. Figure 4.5 illustrates the severity of this effect on the pulse energy and the corresponding harmonic cutoff energy for neutral argon. For these simulations, an 800 nm, 25 fs laser pulse was propagated down a 5 cm long, 150 μm diameter, hollow dielectric waveguide in the EH_{11} mode ($J_0(r)$ Bessel function mode [113]) with an initial peak intensity of 10^{15} W/cm^2. The waveguide was assumed to be filled with 5 Torr of argon.

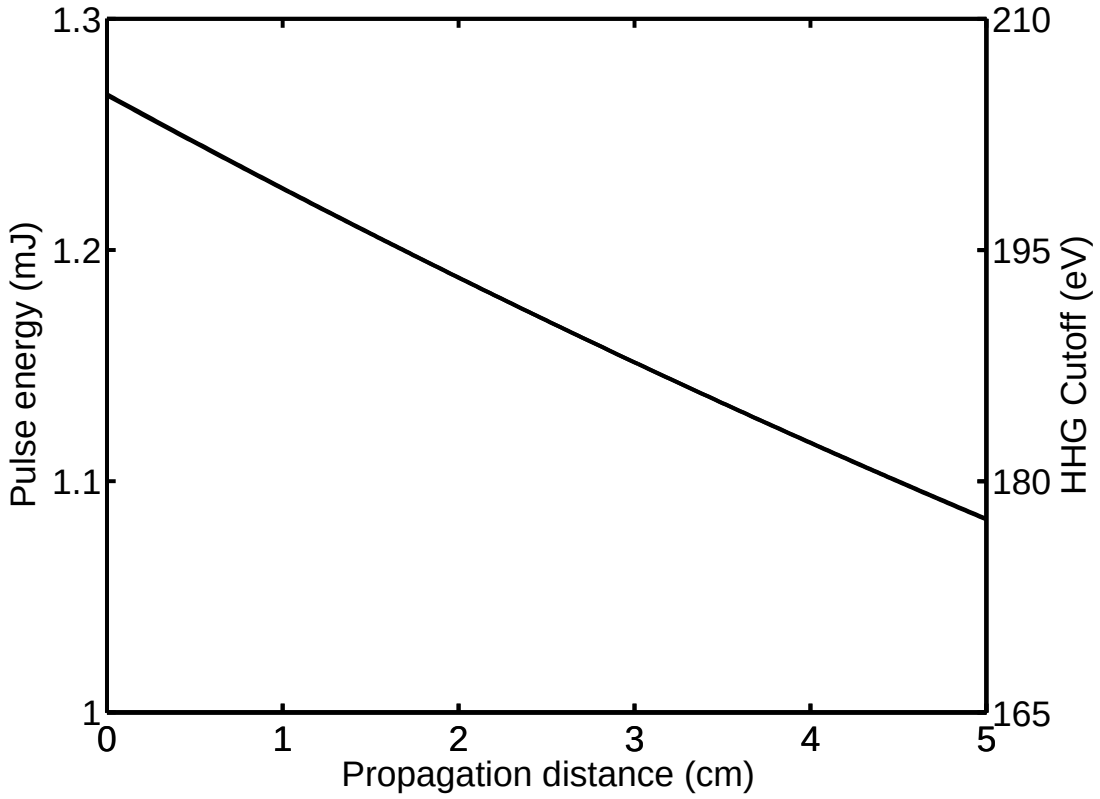

Figure 4.5: Simulation illustrating the energy lost to ionization and the corresponding drop in cutoff energy as a pulse propagates through an argon filled hollow dielectric waveguide.

In addition to the energy loss that accompanies ionization of a gas by a laser pulse, ionization-induced defocusing [114] is another mechanism that can lower or limit the peak laser intensity, thus lowering the cutoff harmonic energy. When a laser pulse ionizes a gas, the spatial profile of the laser is mapped to the spatial distribution of electrons, through the intensity dependent ionization rate. For a beam with a Gaussian or Bessel function profile, this leads to an electron density that is maximum on the propagation axis and minimum at the profile edge, resulting in an index of refraction that is minimum on axis and maximum near the profile edge, as can be seen by Eq. 4.36, where the electron density and index are now functions of space and not time. The strength of this effect is measured by the "defocusing length", Eq. 4.40 [114], which corresponds to a doubling of the beam divergence. When this length is shorter than the Rayleigh range (Eq. 4.41), plasma defocusing should be the dominant effect regarding the laser propagation.

$$l_D = (\lambda/2)(N_{crit}/N_e) \tag{4.40}$$

$$z_R = \frac{\pi\omega_0^2}{\lambda} = \frac{4\lambda}{\pi}(F\#)^2 \tag{4.41}$$

where λ is the laser wavelength, $\omega_0 = (\lambda f)/(\pi\omega)$ is the focal spot radius in a vacuum, f is the lens focal length, ω is the beam radius on the lens, and $F\# = f/(2\omega)$ is the f-number of the focusing system. In terms of the critical density, plasma defocusing becomes dominant when $N_e \approx 4 \times 10^{-5}\ N_{crit}$ for typical focusing where $F\# \approx 100$. This is approximately 10^{16}–10^{17} cm^{-3} for 800 nm light, which corresponds to $\sim$ 1–10 Torr of an ideal gas.

The last, and possibly most significant, macroscopic effect on the observable harmonic signal is phasematching. In phase sensitive nonlinear processes, such as frequency doubling, sum- and difference-frequency mixing, and high harmonic generation, the sig-

nal will be maximal when the generated fields add coherently at every point along the direction of propagation in the nonlinear medium. This requirement is satisfied if the phase velocities (and consequently the wave vectors) of the driving and generated fields are equal. If they are not equal, the fields generated at different locations along the propagation direction will add constructively and destructively, as illustrated in figure 4.6.

From classical nonlinear optics, the field of the q^{th} harmonic, after propagating through a nonlinear medium of length L, is

$$E_q \propto \int_0^L E_f^n \; d(z) \; e^{-i\Delta k z} dz \tag{4.42}$$

where E_f is the driving (fundamental) field, n is the effective order of the nonlinear process, $d(z)$ is the nonlinear coefficient, $\Delta k = qk_f - k_q$ is the phasemismatch, and k_f and k_q are the wave vectors of the fundamental field and the q^{th} harmonic, respectively. The intensity of the q^{th} harmonic at the exit of the medium is maximized when $\Delta k = 0$, as can be seen in Figure 4.7. Assuming E_f^n and $d(z)$ are independent of the propagation direction z, performing the integration in Equation 4.42 leads to the following relation between the intensity of the q^{th} harmonic and the phase mismatch,

$$E_q \propto L^2 \mathrm{sinc}^2(\frac{\Delta k L}{2}). \tag{4.43}$$

Even if perfect phase matching is not possible, minimizing the phase mismatch will result in the largest harmonic signal. Figure 4.8 shows the harmonic signal growth as a function of material length for different phase mismatch values. The harmonic intensity will grow quadratically with medium length when $\Delta k = 0$, but will oscillate due to a non-zero phase mismatch. These oscillations can be described in terms of a characteristic length, the coherence length (Eq. 4.44), which is defined as the length necessary for a phase shift of π to develop between the signal generated at two different

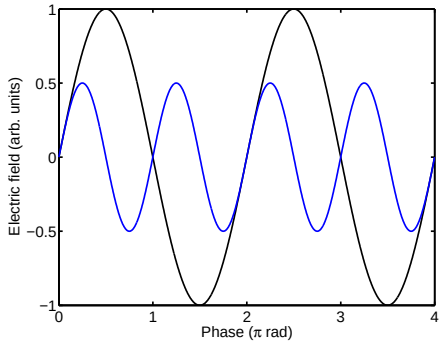

(a)

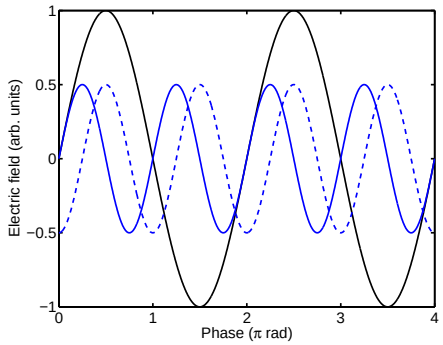

(b)

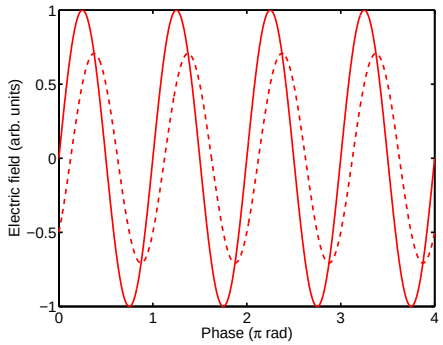

(c)

Figure 4.6: Illustration of phase matched and non-phase matched signal generation. (a) Relation between driving (black) and generated (blue) fields at every position for phase matched signal generation. (b) Relation between driving field (black) and fields generated at a previous position (dashed blue) and the current position (solid blue) for non-phase matched signal generation. (c) Total generated signal for phase matched (solid red) and non-phase matched signal generation (dashed red).

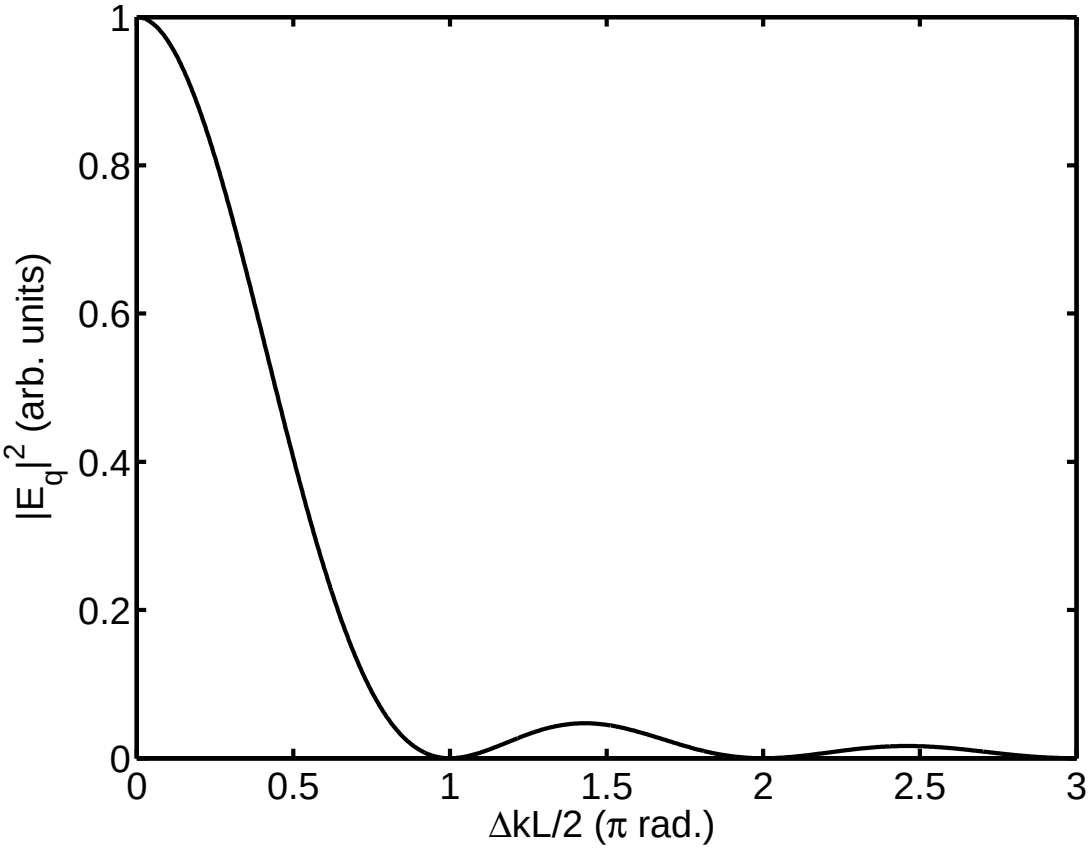

Figure 4.7: Normalized harmonic intensity as a function of phase mismatch for a medium of length L.

positions along the propagation direction. It is also the length over which the harmonic signal increases before being converted back into the fundamental field. As is evident from Figure 4.8, larger phase mismatch results in shorter coherence lengths which results in less harmonic output.

$$L_{coh} = \frac{\pi}{\Delta k} \tag{4.44}$$

For harmonic generation in a hollow waveguide, the phase mismatch originates from three dispersion mechanisms: the neutral gas (Δk_n), the free electrons (Δk_p) and the waveguide (Δk_w). It is assumed that the neutral gas has an index of refraction ≈ 1 at the harmonic wavelengths and that the harmonic signal is generated with a sufficiently small spatial profile such that it does not interact with the waveguide. With these assumptions, the phase mismatch in a hollow waveguide is

$$\begin{aligned} \Delta k &= \Delta k_n + \Delta k_p + \Delta k_w & (4.45) \\ &= \frac{2\pi q P \delta_n (1-\eta)}{\lambda P_{atm}} - \frac{\eta P N_{atm} r_e}{P_{atm}} \left(q\lambda - \frac{\lambda}{q} \right) - \frac{q u_{nm}^2 \lambda}{4\pi a^2} & (4.46) \end{aligned}$$

where q is the harmonic order, λ is the fundamental wavelength, r_e is the classical electron radius, u_{nm} is a constant corresponding to the propagation mode in the waveguide, a is the waveguide radius, and P, P_{atm}, N_{atm}, δ_n, and η are defined above. For the EH_{11} mode of the hollow waveguide, u_{11} is equal to the first zero of the Bessel function J_0. For small values of η, there exists a pressure for which $\Delta k = 0$, but for large η (usually a few percent) phase matching is not possible and quasi-phase matching techniques are necessary [91, 115].

4.3 Plasma waveguides

Hollow, dielectric waveguides have been used to increase the interaction length between laser pulses and a target gas for the purposes of phasematched high harmonic

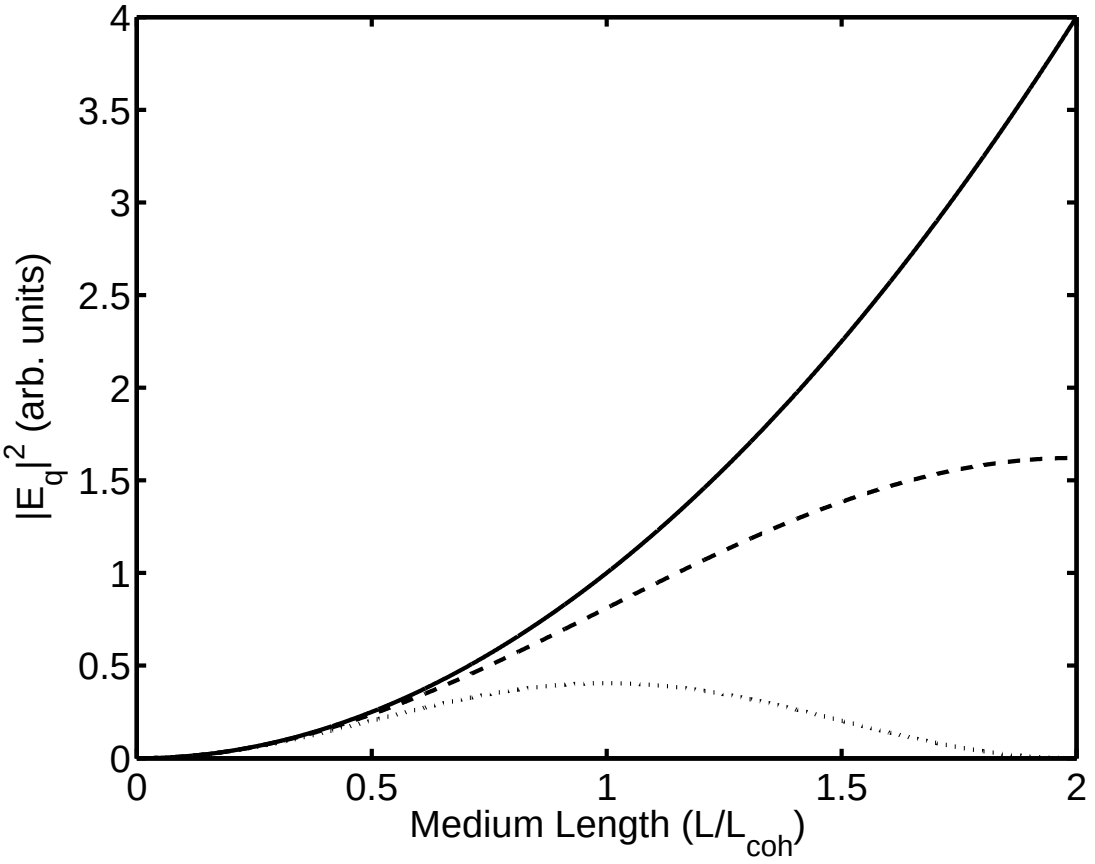

Figure 4.8: Harmonic intensity as a function of material length for $\Delta k = 0$ (solid), $\pi/(2L_{coh})$ (dashed) and $\pi/(L_{coh})$ (dotted).

generation [80] and ultrashort (< 5 fs) pulse generation [112]. The amount of laser energy that can be guided by this type of waveguide is limited due to ionization-induced defocusing [114] and ablation of the waveguide by the high intensity laser pulse. Other techniques for guiding high intensity laser pulses through ionizing gases and plasmas have been developed, such as self-guiding [116–122] and pre-formed plasma waveguides [25–28,123–125]. Self-guided laser pulses, requiring very high intensities ($\sim 10^{18}\mathrm{W/cm}^2$) rely on a balance of diffraction, plasma defocusing and relativistic self-focusing to guide a pulse over many Rayleigh lengths. This process relies on a delicate balance between a number of nonlinear phenomena, making it extremely susceptible to instabilities. In addition, it is impossible to tailor the properties of the guide and the laser pulse separately since the pulse, in essence, creates the waveguide.

Both dielectric and pre-formed plasma waveguides have the benefit of separating the creation of the guide and the laser pulse that is to be guided. In the case of pre-formed waveguides, the properties of the guide can be dynamically tuned. Whether these pre-formed guides are created by a laser pre-pulse [25,123,124] or by a capillary discharge [26,28,125], the basic principle is the same: a plasma is created with a density minimum on axis and maximum near the edge of the waveguide. In the case of a laser pre-pulse focused into a low density gas, the pre-pulse ionizes and heats the electrons in the axially-extended focus. This ionization and heating creates a pressure gradient, causing the electrons to travel radially outwards, dragging the ions with them and leaving a minimum in the plasma density on axis. In the case of a fast capillary discharge-driven plasma waveguide, a hollow dielectric waveguide is filled with a low density gas and a low simmer current is applied. A fast rising current pulse is then discharged down the pre-ionized gas, ionizing it further and heating the plasma. A large $\vec{\mathbf{v}} \times \vec{\mathbf{B}}$ force causes a rapid compression, and further collisional ionization, of the plasma column. The plasma column compresses from the edge towards the center, giving rise to a plasma density that is maximum at the edge of the compressed region and minimum on axis, resulting

in a plasma waveguide whose diameter is shrinking.

To analyze the effect of the plasma waveguide, the index of refraction is assumed to be dominated by the free electron density, which is assumed to be much less than the critical density corresponding to the wavelength of the driving laser. These assumptions lead to Eq. 4.37 as the index of the plasma. The final assumption is that the electron density has a parabolic radial profile (Eq. 4.47).

$$N_e(r) = N_0 + \Delta N \left(\frac{r}{r_0}\right)^2 \tag{4.47}$$

where N_0 is the electron density on axis, ΔN is the change in density from the center to the edge of the waveguide, r is the radial position, and r_0 is the radial extent of the waveguide. It has been shown [123] that Equation 4.47 is a good approximation to the actual electron density profiles. The transverse modes of an infinite, parabolic plasma waveguide can be determined by solving the wave equation (Eq. 4.48) with cylindrical symmetry.

$$\nabla^2 E_\perp + (n(r)^2 k^2 - \beta^2) E_\perp = 0, \tag{4.48}$$

where $E_\perp$ is the transverse electric field profile, $n(r)$ is the index profile, k is the vacuum wavenumber, and β is the wavenumber in the direction of propagation. The result is an infinite number of LaGuerre-Gaussian modes, with the lowest order solution being a Gaussian profile. For a truncated waveguide, ($N_e(r) = N_0 + \Delta N$ for $r > r_0$), there are a finite number of bound modes. For real plasma waveguides, the electron density drops off for $r > r_0$, resulting in modes that leak into this low density region. Low-order modes are still guided well by this leaky waveguide (and the parabolic assumption is valid), but higher order modes are not. A laser pulse with a Gaussian spatial profile will be guided by a capillary discharge (Eq. 4.47) at a constant radius (ω_0) when that radius is matched to the plasma waveguide. This matched radius (see Appendix C),

r_M, is given by [125]

$$r_M = \left[\frac{r_{ch}^2}{\pi r_e \Delta N}\right]^{\frac{1}{4}} \tag{4.49}$$

where r_{ch} is the diameter of the capillary discharge, $r_e = e^2/4\pi\epsilon_0 mc^2$ is the classical electron radius, and ΔN is the change in electron density from the center to the edge of the capillary discharge. Figure 4.9 shows the electron density and the radial intensity profile for a laser pulse matched to a 300 μm diameter capillary discharge with an on-axis plasma density (N_0) of 10^{17} cm^{-3} and $\Delta N = N_0$. Such capillary discharge plasmas are ideal for high harmonic generation, as will be seen in the next chapter.

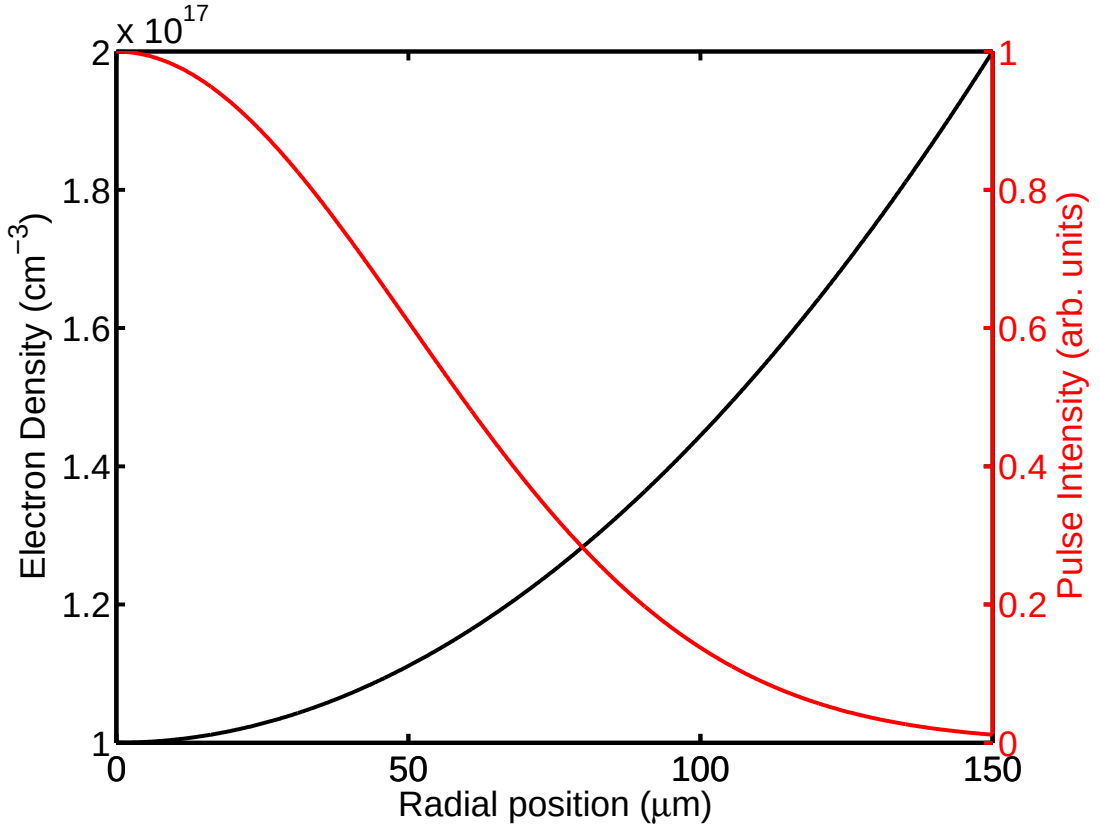

Figure 4.9: Plot showing the relation between the electron density (black) and radial laser intensity (red) for a laser pulse matched to a 300 μm capillary discharge with $N_0 = \Delta N = 10^{17}$ 5cm^{-3}.

Chapter 5

High-order harmonic generation from ions in a capillary discharge

5.1 Introduction

In recent years, high-harmonic generation (HHG) research has been directed toward the production of higher photon flux at shorter wavelengths. There has been much success with the use of short ($<$ 20 fs) laser pulses [78, 92, 93] to extend the harmonic cutoff to much shorter wavelengths as well as the use of quasi-phasematching techniques [91,115] to increase the photon flux, particularly in the water window ($\sim$284–532 eV). In order to generate high-order harmonics in this region of the soft x-ray spectrum, noble gas atoms with very large ionization potentials are used. According to the three-step, semi-classical model, atoms with large ionization potentials will require a higher laser intensity to ionize, thus releasing an electron into a larger electric field. The electron will gain more energy in this larger electric field and, upon recollision with the parent ion, can release a higher energy photon. From the cutoff rule (Eq. 4.10), it can be seen that atoms with lower ionization potentials will necessarily emit photons with lower energy. Therefore large ionization potentials are required for the generation of high-order harmonics with very short wavelengths. Unfortunately, atoms with larger ionization potentials (He, Ne) tend to have lower effective nonlinear susceptibilities than atoms with smaller ionization potentials (Ar, Kr, Xe) [126]. This lower effective susceptibility leads to lower harmonic signal [74].

Therefore, the problem of efficiently generating short wavelength harmonics re-

duces to the problem of combining the large ionization potential of the lighter atoms with the large polarizabilities of the heavier atoms. One very interesting solution is to use the ions of the heavier gas atoms. These ions will, necessarily, have a larger ionization potential than their respective neutral atoms, approaching the ionization potentials of the lighter atoms ($I_p = 21.60$ eV for Ne, $I_p = 21.21$ eV for Xe^+). In addition, since the ion is large, it should have a large recollision cross section, increasing the probability that an electron will recombine upon returning to the ion. It has been shown theoretically [88, 97] that the magnitude of the single atom response is approximately equal for neutral atoms and their ions, except that the cutoff for ions occurs at much higher photon energies.

Initial work on generating high harmonics from ions was performed with ions created through the ablation of a solid target [127]. Other work used a KrF (248 nm) laser to generate harmonics from rare-gas-like ions (Li^+, Na^+, K^+), also created from a solid target [128,129]. From these early experiments, it was concluded that rare-gas-like ions were superior to the rare gas atoms for high harmonic generation when a short wavelength driving laser was used. These experiments did not have a well characterized target species and thus emission from the neutrals and ions could not be distinguished. Moreover, these experiments did not benefit from any waveguide effect and as a result, no dramatic extension of cutoff was observed. Harmonic generation using a near-IR (784 nm) laser [76] produced spectra from argon and xenon which suggested the emission was from ions, but it was not extensively investigated. Further experiments generated harmonics from rare-gas-like ions ablated from a solid target [87] as well as underdense aluminum plasmas illuminated with a UV laser pulse train [89], but these experiments concluded that the HHG from the ions was less than that of comparable neutral gas atoms. Wahlström *et al.* [87] suggested that the reduction in signal with the ions was due to ionization-induced defocusing. Recent work [88] has shown that the effect of ionization-induced defocusing can be minimized, but not eliminated, by the use of a

hollow capillary waveguide, and harmonic photons up to ∼250 eV can be generated by argon ions. However, the effects of ionization-induced refraction of the laser beam are still significant, as are the effects of energy loss due to ionization and phase matching. The first two effects lead to significant losses in the waveguide, ultimately limiting the laser intensity and cutoff photon energy.

In this work, xenon was used as the target gas because it has a very large effective susceptibility. The highest photon energy generated from xenon to date with an 800 nm driving laser was ∼70 eV [76] and was attributed to xenon ions. Emission from xenon ions could extend the HHG cutoff to substantially higher photon energies. However, because of the low ionization potential of Xe (12.13 eV), there is significant energy loss due to ionization and ionization-induced defocusing as well as poor phase matching conditions due to the large electron density. As previously mentioned, a capillary discharge can provide an ionized medium where ionization-induced defocusing and energy loss due to ionization are virtually eliminated, leaving phase matching as the last limitation to efficient generation of harmonics from ions.

Capillary discharges are capable of generating elongated plasma columns with a radial concave electron density profile, which efficiently guide high intensity laser pulses [28,130,131] and reduce the effects of plasma defocusing. Moreover, the degree of ionization can be tuned by changing the discharge current, as seen in Figure 5.1. This is important for HHG since the driving laser can then interact with a tailored, preformed, completely ionized plasma, minimizing the plasma defocusing and energy loss due to ionization.

In order to take advantage of the guiding behavior of the capillary discharge, the operating parameters (gas pressure, peak current, current pulse width, etc.) need to be optimized. Due to the large parameter space involved, a simulation of the capillary discharge was developed at Colorado State University to provide insight into the correct parameter combination. Once an optimal set of parameters was chosen, the simulation

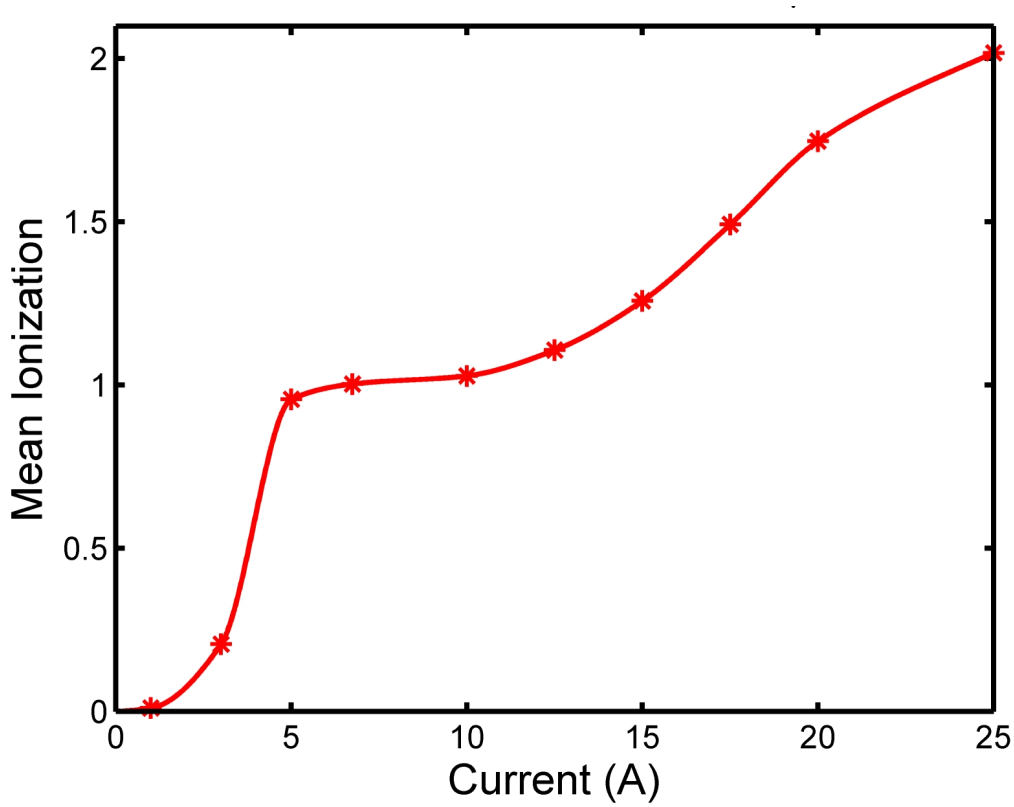

Figure 5.1: Simulation of the mean on-axis ionization as a function of peak discharge current ($\sim$2 μs decay time) for a 175 μm diameter capillary discharge, filled with $\sim$3 Torr of xenon.

was used to predict the laser spot size that would be guided by the plasma waveguide. In addition to predicting the plasma waveguide parameters, the simulation was used to predict the spatial and temporal ion populations. A direct measurement of the ion populations is difficult given the fact that the plasma is confined by the capillary.

5.2 Capillary discharge simulation

The program used to simulate the capillary discharge was developed by Berrill and Rocca [132] and is explained in detail in Mark Berrill's senior design thesis [133]. Originally developed to model the EUV laser capillary discharge, the code was also used to model the low current capillary discharge used in these experiments. The code is a magneto-hydrodynamic (MHD) code that incorporates an advanced atomic model to calculate the collisional ionization rates. Results of the simulation can be seen in Figs. 5.1, 5.9, 5.11.

5.3 Experimental setup

The high harmonic generation experiment, illustrated schematically in Figs. 5.2 and 5.3, was conducted by focusing pulses from a 10 Hz chirped pulse amplification Ti:sapphire laser system [134], constructed for these experiments, into a plasma column generated by an electrical discharge in a 175 μm diameter bore, fused silica capillary. The 10 Hz CPA system begins with a typical 88 MHz Ti:sapphire oscillator, followed by a grating-based stretcher, which stretches the pulse to $\sim$150 ps. Following the stretcher is a Pockels cell which drops the repetition frequency to 10 Hz. After the Pockels cell, the pulses are sent into the first stage amplifier, which consists of a nine pass, Ti:sapphire amplifier and a four pass, bow tie second stage amplifier, which increases the pulse energy to 40–50 mJ. After the second stage, a vacuum spatial filter is used to improve the beam quality while only reducing the pulse energy by $\sim$10%. The optics of the spatial filter also serve as a telescope to expand the beam to avoid damage to the

compression gratings. The amplifier pulses are compressed to ∼28 fs and then directed into the capillary discharge.

This capillary discharge (Figs. 5.4 and 5.5) was designed and constructed at Colorado State University and is a low peak current version of the ones used as EUV lasers [32]. Laser pulses, with a pulse duration of 28 fs and an energy of 5 mJ, were focused in vacuum to a waist diameter of ∼100 μm at the entrance of the capillary. Two holes drilled 3 mm from the ends of the capillary serve as gas inlets and help maintain a uniform gas pressure in the 4.5 cm long central region. The total length of the capillary is $\sim$ 4.7 mm, leaving two 1 mm end sections for differential pumping. The pressure in front of and behind the capillary was less than 1×10^{-4} Torr and 5×10^{-5} Torr, respectively, when the capillary was filled with 2.9 Torr of xenon. The front gas inlet was surrounded by a hollow cathode, while the anode consisted of a metal plate at the end of the capillary, with a through-hole to allow the harmonic light to exit.

The compact discharge was mounted on an X-Y positioning stage supported by a 2-axis tilt platform to facilitate alignment with the laser pulse. The HHG spectrum was measured using a flat field EUV spectrometer and an x-ray CCD camera. Thin aluminum or Al-coated zirconium filters (Lebow Company) were placed between the spectrometer and the CCD camera to block the fundamental laser light. Two 200 nm thick aluminum filters were used to observe the EUV spectrum below 72 eV and two 200 nm thick zirconium filters were used to observe the spectrum between 60 and 200 eV. A thin, 25 nm layer of aluminum was deposited on the front zirconium filter to increase the attenuation of, and prevent damage from, the fundamental (800 nm) laser light. The acquired spectra were calibrated using two methods, depending on the spectral region. For spectra taken through the aluminum filters, the aluminum edge (72.8 eV) was used in conjunction with the well resolved harmonic peaks to calibrate the photon energy axis. Since the low order harmonics are typically generated early in the pulse, where the intensity and ionization is low, one can safely assume the peaks are

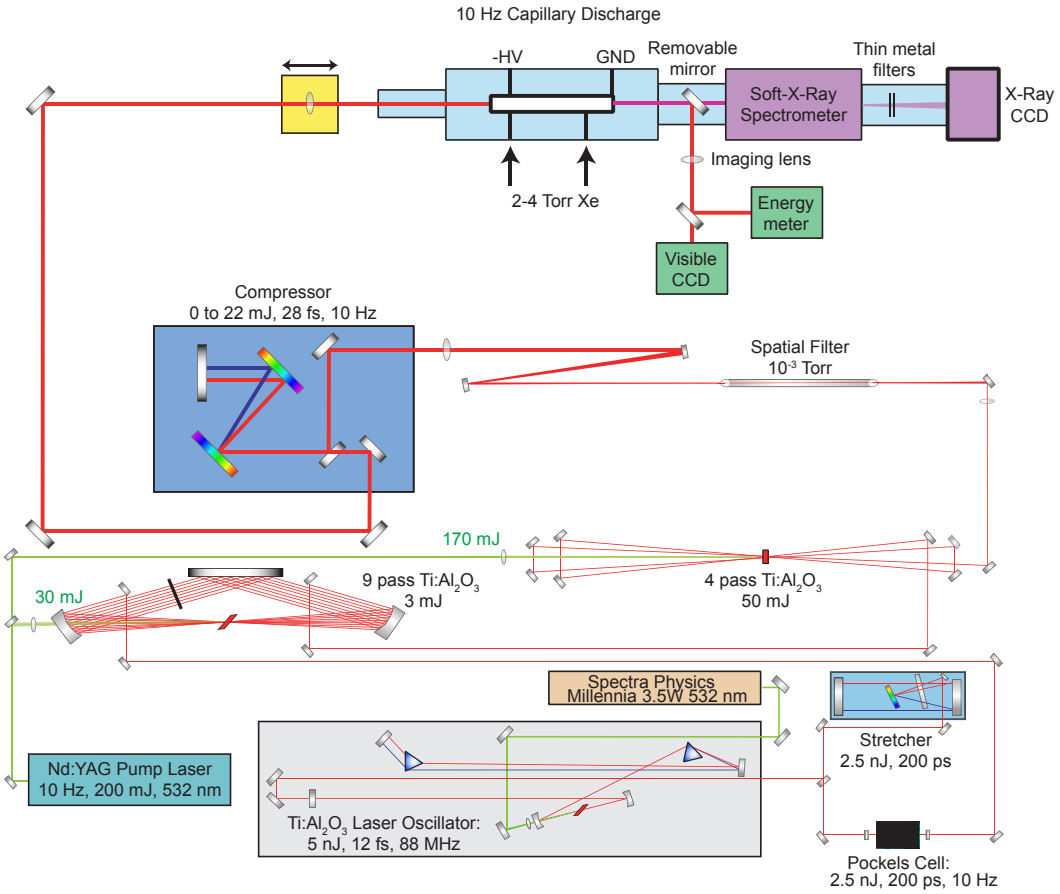

Figure 5.2: Schematic of the 10 Hz laser system and capillary discharge.

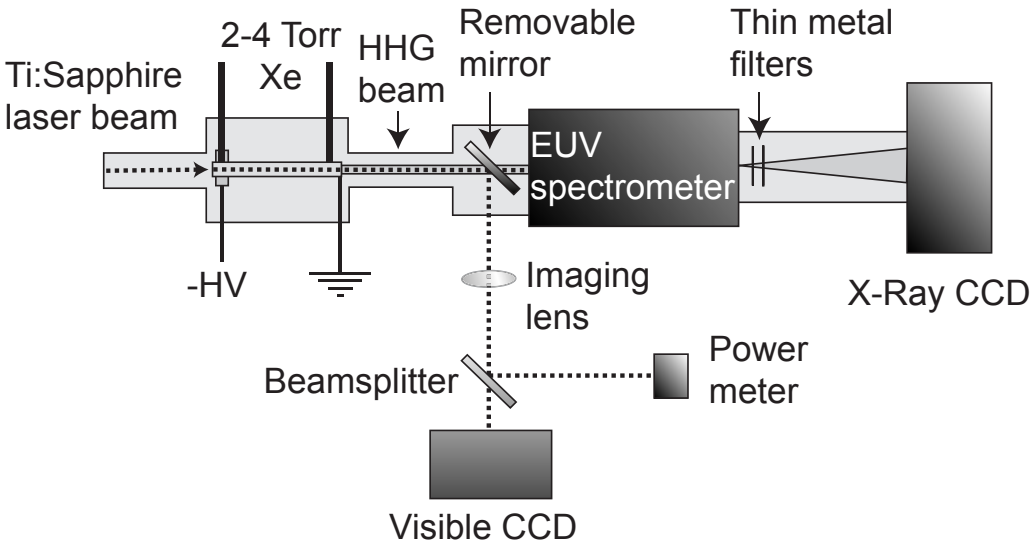

Figure 5.3: Enlarged schematic of the experimental set-up. (Adapted from Fig.1 of [1])

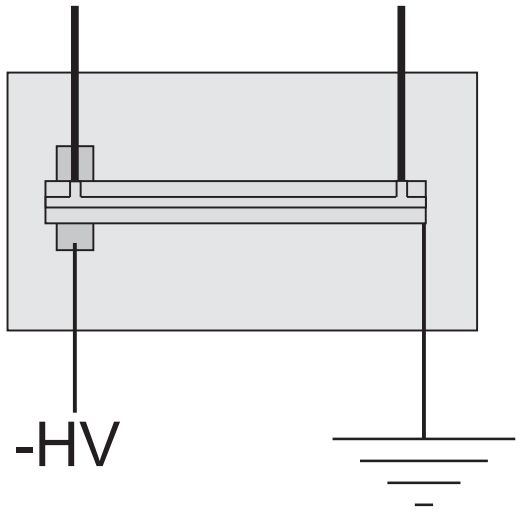

Figure 5.4: Schematic of the capillary discharge.

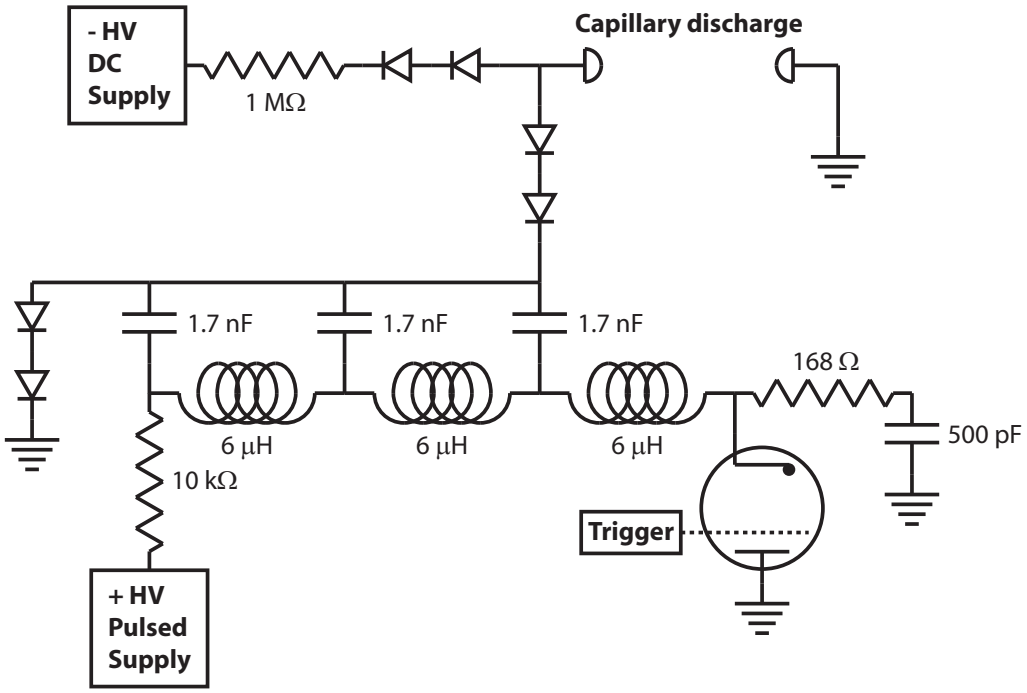

Figure 5.5: Circuit diagram of the capillary discharge electronics.

separated by twice the driving photon energy (∼1.55 eV). For spectra measured through the aluminum-coated zirconium filters, a 200 nm aluminum filter and a 400 nm silicon filter, with an absorption edge at 100 eV, were used to calibrate the energy axis. The calibration data was taken with argon as the generation gas, since the signal from argon is brighter at the higher photon energies. A typical integration time for the calibration spectra was 60 seconds. In contrast, the integration time for the xenon spectra was 600 seconds. In addition, the spatial mode and pulse energy of the laser light exiting the capillary was measured by inserting a removable mirror after the capillary and directing the laser light into an imaging system and power meter.

The capillary was filled with 2–4 Torr of xenon gas, and a continuous DC simmer current of ∼10 mA was used to maintain a low degree of ionization to predictably initiate the pulsed discharge. By applying a current pulse of varying amplitude with rise time ∼350 ns and a decay constant of ∼2 μs, a pre-formed plasma consisting of predominantly Xe II or Xe III can be created (Fig. 5.1). The combination of ohmic heating and heat conduction to the capillary walls creates a plasma column with maximum temperature on axis. Pressure balance gives rise to a concave electron density profile with a minimum on axis constituting an index waveguide [130]. The HHG results reported here were obtained using a 5 A peak current, as measured by a Rogowski coil. The discharge was operated at 10 Hz and was synchronized to the laser. Time resolved visible spectroscopy on the discharge was performed by replacing the EUV spectrometer with a 0.6 meter visible spectrometer (50–100 μm entrance slit) and a gated, intensified, diode array.

5.4 Guiding of high intensity lasers with a capillary discharge

Since guiding of high intensity laser pulses in a fast capillary discharge has been demonstrated in the past [27, 28], the first experiment conducted with this equipment was to verify guiding of a high intensity laser pulse. Verification of laser guiding also allowed for the validation of the capillary discharge simulation. For these experiments a

250 μm diameter, hollow bore capillary was filled with 5–7 Torr of argon and driven with a 1 μs, 50 A, square current pulse. Laser pulses with 1–5 mJ of energy were injected into the plasma waveguide at varying times with respect to the rise of the current pulse. The laser mode was imaged onto a visible CCD while the energy was simultaneously measured with a laser power meter. A wire mesh grid, originally used to support a thin metal filter purchased from the Lebow Company, was used to provide a calibration of the beam profile imaging system and to ensure the imaging system was in focus. According to the Lebow Company, this standard mesh grid has 70 lines per inch, corresponding to a center-to-center wire spacing of $\sim$363 μm (Fig. 5.6), which gives a calibration of 2.56 μm/pixel. This calibration was used to determine the $1/e^2$ diameter of the beam profiles.

Figures 5.7 and 5.8 show the performance of the capillary discharge as a plasma waveguide. Before the current pulse is initiated, the throughput of the system is $\sim$30 % for a 5 mJ pulse and 5 Torr argon. Approximately 200 ns after the rise of the current pulse, the transmission increases to $\sim$66 % and remains at this level until the current pulse starts to decay, around 800 ns. The beam profiles, taken with a pulse energy of $\sim$ 1 mJ and 6.7 Torr argon, show the same behavior. Before a delay of 200 ns, the beam profiles show some structure and have low intensity. Between 200 and 800 ns, the intensity increases and the mode improves significantly. After 800 ns, the mode slowly degrades to a mode similar to that observed before the onset of the discharge. Images taken with a 5 mJ laser pulse show the same behavior. During optimal guiding conditions, the exiting beam has a diameter of 130 $\pm$ 5 μm. This diameter was determined from the measured images by directly determining the $1/e^2$ points as well as using a 90-10 knife edge technique. Both methods result in similar diameters.

Figure 5.9 shows the predicted electron density profile for a 50 A, 1 μs square pulse driving 10 Torr of argon, at a delay of 800 ns. Calculating the matched radius (Eq. 4.49), from this profile gives a diameter of 122 μm. Recalculating the matched radius

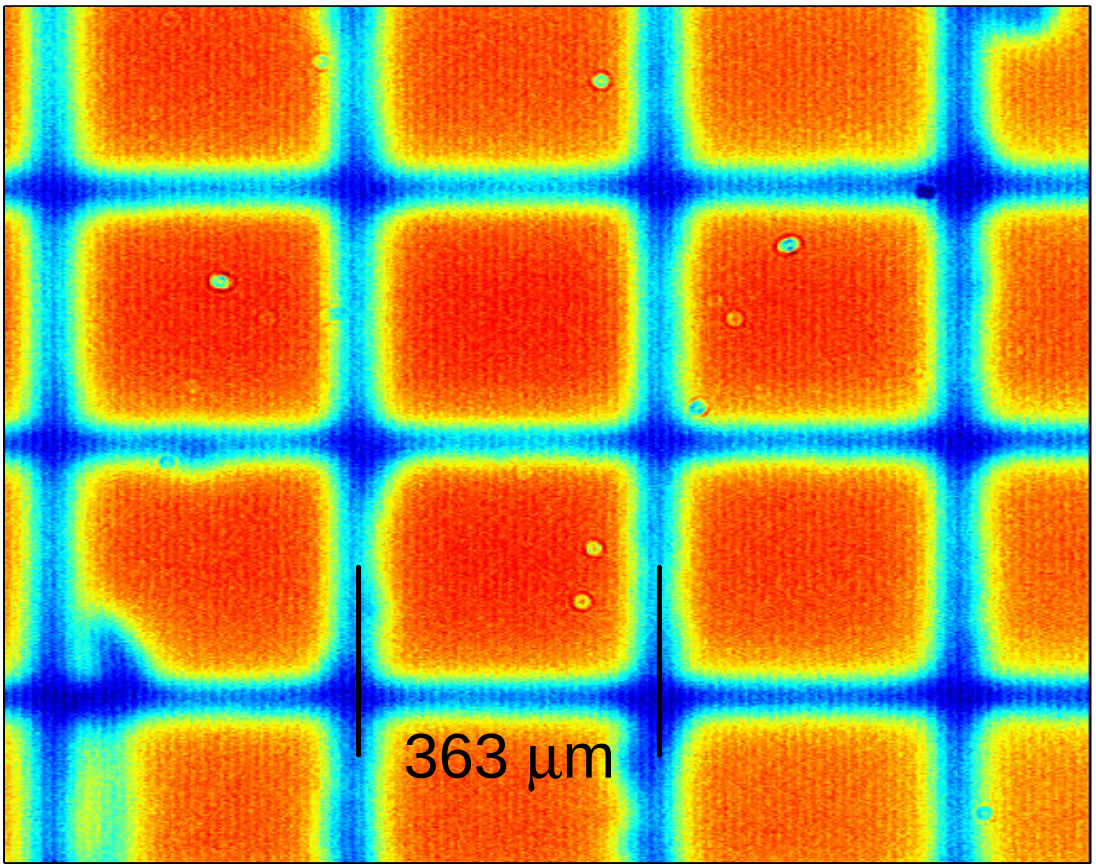

Figure 5.6: Wire grid image used to calibrate beam profile imaging system.

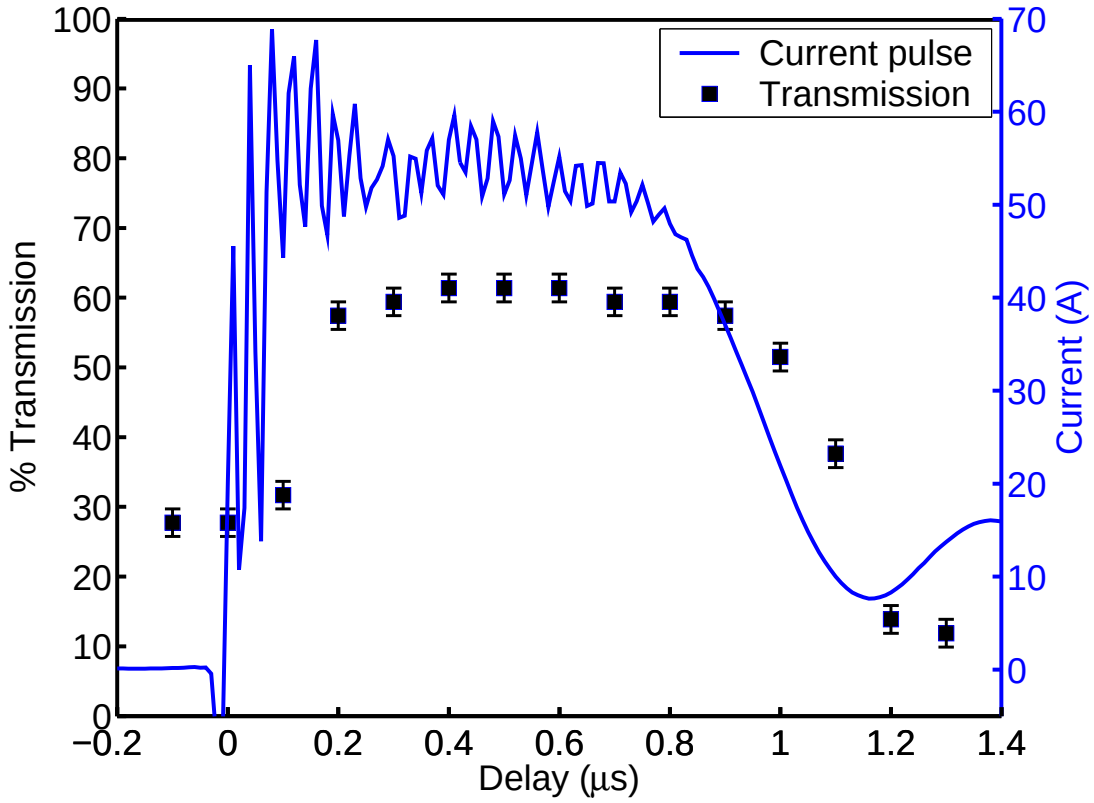

Figure 5.7: Percent transmission of a 5 mJ laser pulse as a function of delay between the rise of the current pulse and the injection time. The current pulse is shown in blue for reference.

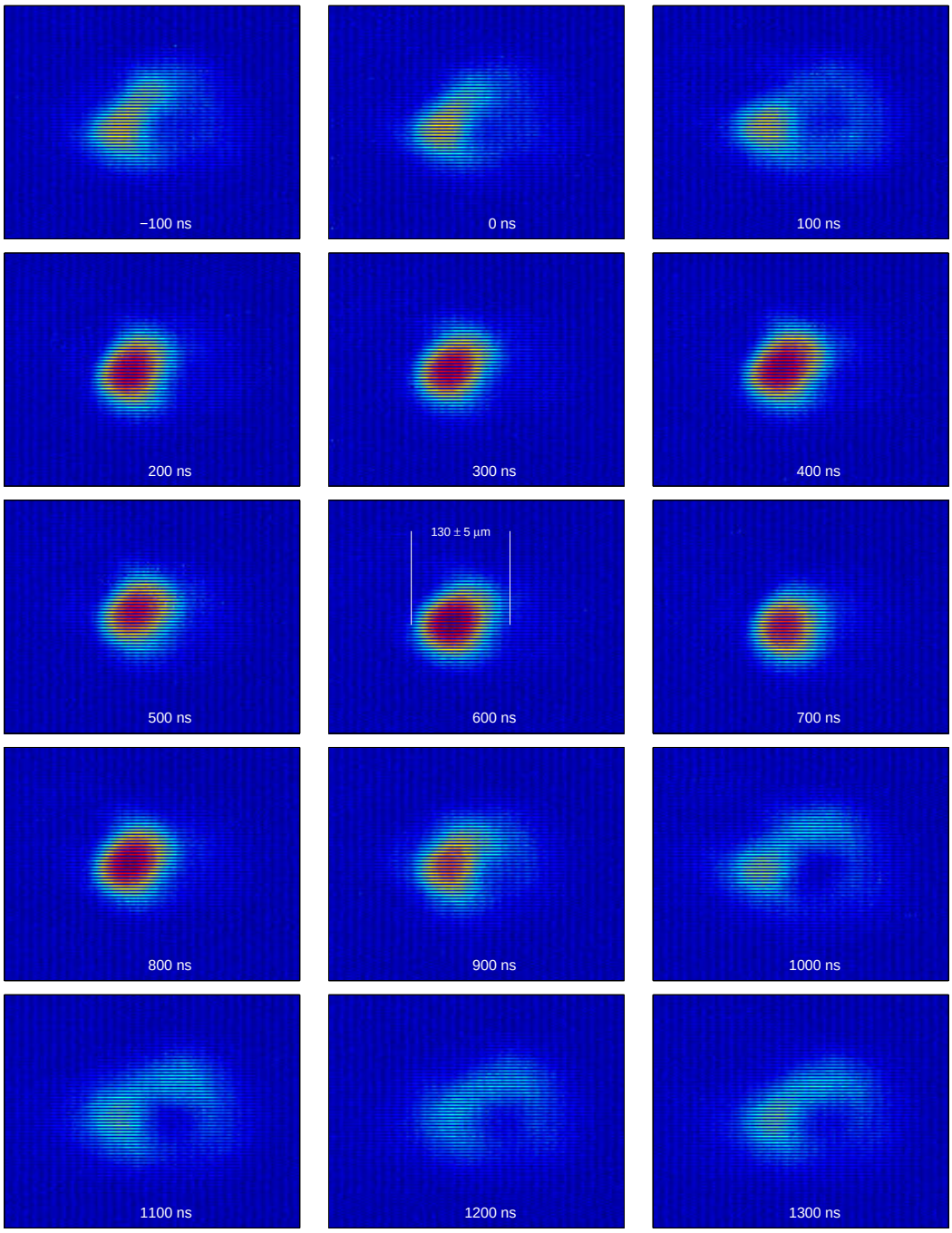

Figure 5.8: Beam profiles at the exit of the capillary discharge as a function of delay.

for 6.7 Torr of argon, by simply scaling the electron density, gives a matched radius of 134 μm, providing excellent agreement between the simulation and experiment.

5.5 High harmonic generation from ions

The three main limitations to generating very high-order harmonics from ions are ionization-induced defocusing, energy loss due to ionization, and poor phasematching. The capillary discharge addresses the first two limitations by creating a preionized plasma with a concave electron density profile. The plasma created by the discharge significantly suppresses energy loss due to ionization-induced defocusing of the laser beam and maintains a high laser intensity in the interaction region. The characteristics of this plasma column were optimized for optimal HHG cutoff, by adjusting the discharge current, the xenon gas pressure, and the delay of the laser pulse with respect to the rising edge of the discharge current. The HHG emission was then monitored, both with and without the discharge current. Under optimal conditions, the cutoff energy can be dramatically extended, as shown in Fig. 5.10 [1]. These spectra were obtained at a xenon pressure of 2.9 Torr with the laser being injected 2 μs after the onset of current pulse.

A typical high harmonic spectrum from xenon has a cutoff around 35–40 eV, but previous measurements have observed a cutoff as high as 70 eV [76]. In this experiment, the observed HHG cutoff in xenon ions was first extended from the previously observed 70 eV to 95 eV using high harmonic generation in a gas filled hollow waveguide (Fig. 5.10, red). This initial extension of the cutoff compared with past work is due to a partial reduction of ionization-induced defocusing in the guided geometry. The short defocusing length in a gas jet, given by Eq. 4.40, would otherwise defocus the laser beam and lead to a reduction in intensity in a distance of under 7 mm [88, 114]. The observed maximum photon energy was then extended further, to 150 eV, by generating the harmonics in a completely ionized xenon plasma column created by the capillary

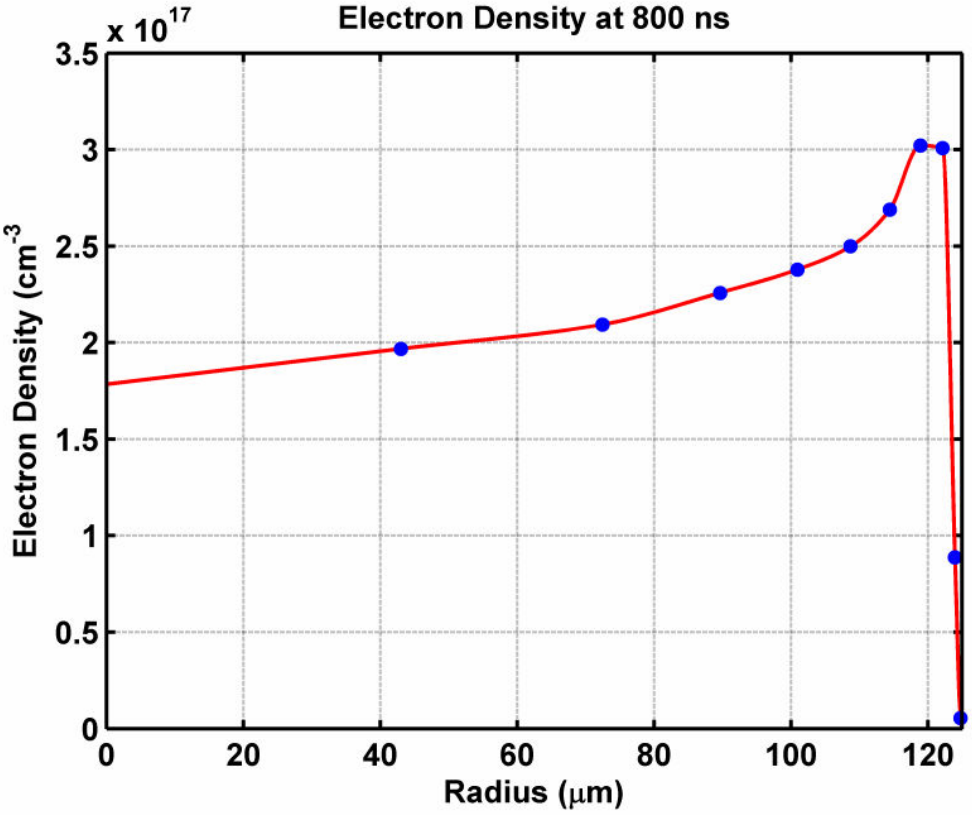

Figure 5.9: Electron density profile predicted for a 250 μm diameter capillary, filled with 10 Torr of argon, and driven with a 1 μs, 50 A, square pulse.

discharge (Fig. 5.10, blue).

The observed photon energies of 150 eV from xenon ions far exceeds the accessible photon energies that can be generated from neutral krypton or xenon atoms and represents greater than a factor of two increase in cutoff energy, when compared to previous work [76]. In addition to the extension of the cutoff photon energy, preionizing with a capillary discharge increases the HHG flux in xenon around the cutoff in a hollow waveguide ($\sim$95 eV) by nearly two orders of magnitude. This technique is not limited to xenon and can be implemented with any of the gases typically used in HHG (He, Ne or Ar). As a result, use of a capillary discharge plasma as a medium for high harmonic generation shows great promise for increasing harmonic flux in addition to extending efficient harmonic generation to much shorter wavelengths.

The extension of the cutoff and the enhancement of the harmonic flux in the presence of the discharge plasma are due to the capillary discharge plasma. First, the discharge creates a concave plasma density profile that is completely ionized on axis prior to the arrival of the laser pulse. Figure 5.11 shows the simulation results of the electron density profile and ion species distribution for the measured current pulse (5 A peak) driving 3 Torr of xenon in a 175 μm diameter hollow capillary. In the center section of the capillary, the electron density has a noticeable concave shape and the matched radius for this profile is $\sim$70 μm. Optimal coupling into the fundamental mode of the hollow waveguide occurs for a gaussian pulse with a radius of $\sim$60 μm. Since neither radii is significantly greater than the other, the beam cannot be guided solely by the hollow waveguide nor the plasma waveguide. This is a situation of "hybrid" guiding. Therefore, the density profile aids in guiding the driving laser pulse and mitigates ionization-induced refraction, while the completely ionized media will reduce the laser energy lost to ionization. Our measurements show that the transmission efficiency of the fundamental light through the waveguide increases from 31% without the discharge to 62% with the discharge on. These effects result in a higher laser intensity throughout the capillary

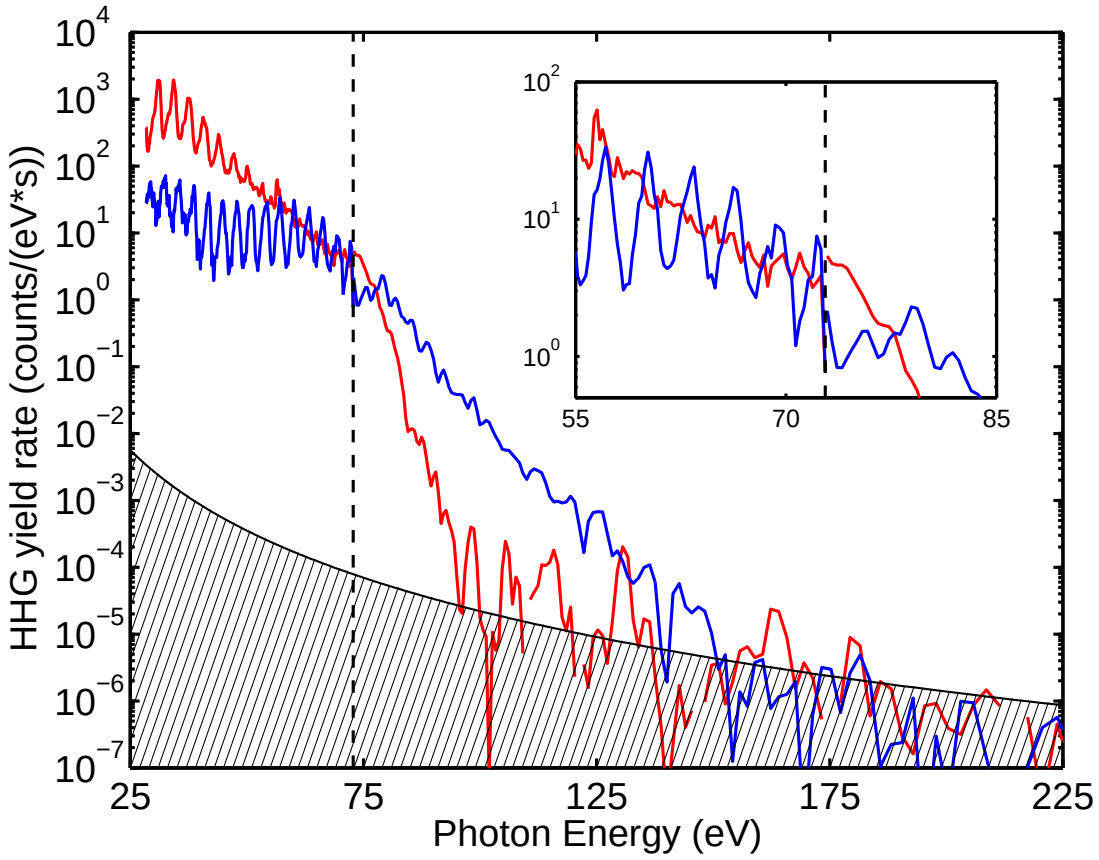

Figure 5.10: High harmonic spectra on a log scale with (blue) and without (red) the preionizing discharge. The vertical dotted line shows the split between data taken through two 200 nm aluminum filters (low energy) and two 200 nm zirconium filters coated with 25 nm of aluminum (high energy). The shaded area represents our noise floor. Inset: harmonic generation in the 55–85 eV spectral region, showing that individual harmonic peaks are much better resolved when the discharge is used to preionize the xenon, thereby reducing ionization-induced modulation of the laser. The integration time for this data was 600 seconds. (Adapted from Fig. 2 of [1])

and therefore, from the cutoff rule, lead to higher harmonic photon energies.

In addition to the reduced ionization-induced defocusing and ionization loss, the presence of xenon ions can also increase the measured HHG signal. The xenon ions created by the capillary discharge exhibit a dramatically lower absorption cross section than neutral xenon atoms in the ∼80–150 eV range [135, 136]. The neutral absorption cross section in this photon energy range is > 5 Mb (10^{-22} m^2), with a peak of ∼30 Mb around a photon energy of 100 eV. In contrast, the partial absorption cross section for singly ionized xenon is 1–2 Mb for 80–100 eV and drops dramatically from ∼1 Mb at 100 eV to ∼0.05 Mb at 150 eV. This large difference in photoionization cross section can result in different amounts of EUV radiation exiting the capillary. For the situation without the preionizing discharge, the highest harmonics are assumed to be generated near the entrance of the capillary, due to the short defocusing length (∼6 mm). These harmonics then propagate through a few centimeters of neutral xenon, attenuating the signal. When the discharge is used to preionize the gas, the absorption is reduced due to the presence of xenon ions, which results in more harmonic emission exiting the capillary.

5.5.1 Blueshift of HHG spectrum

Another prominent feature in the data of Fig. 5.10 (and magnified in the inset) is the fact that, in the 55–85 eV spectral region, the individual harmonic peaks are much better resolved when the discharge is used to preionize the xenon. Without the discharge, the lack of resolved harmonic peaks results from self-phase modulation (SPM) of the fundamental laser pulse that would be expected to accompany the rapid ionization of the neutral xenon by the laser. The rapid ionization causes the central wavelength of the driving laser to shift toward shorter wavelengths. This shift is continuous as the pulse propagates down the entire length of the capillary. Therefore, the central wavelength of the harmonic spectrum, and thus the spectrum itself, is different

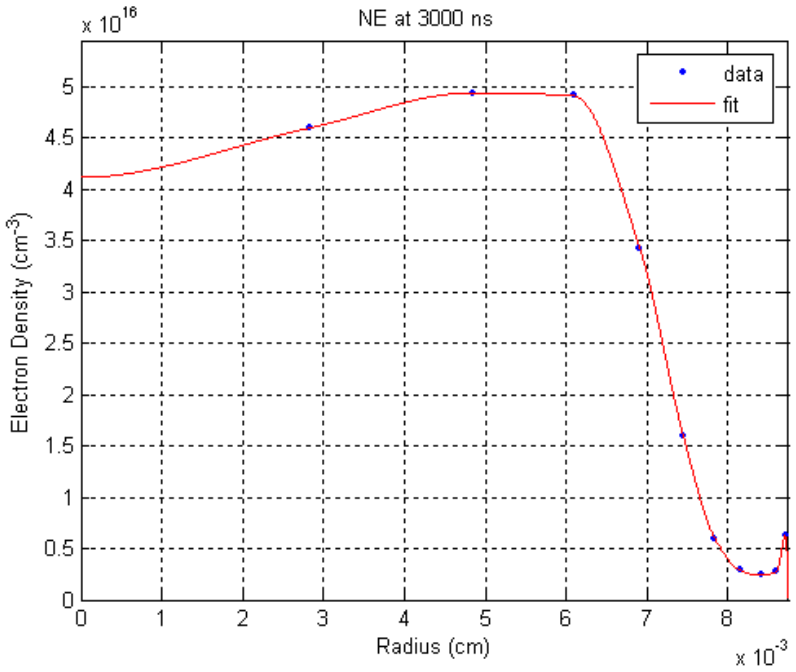

(a)

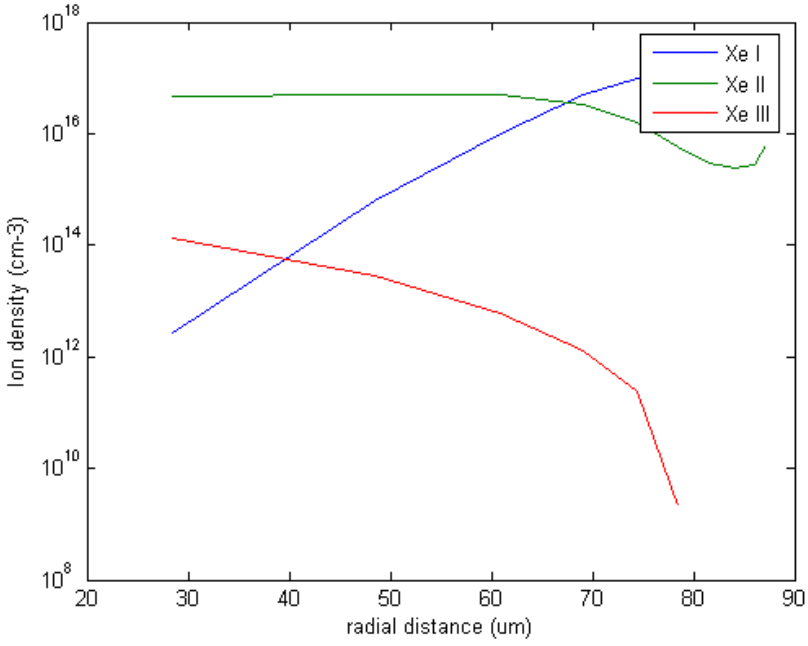

(b)

Figure 5.11: (a) Predicted electron density profile and (b) ion species distribution for a 5 A peak discharge current in a 175 μm capillary filled with 3 Torr of xenon.

at different locations along propagation. This causes the observed harmonic spectrum to smear, resulting in the relatively smooth spectrum of Fig. 5.10. When the discharge preionizes the xenon, phase modulation of the laser is dramatically reduced, and occurs only through ionization of the ions. This reduced phase modulation leads to better resolved harmonic peaks, due to little or no shift in the central wavelength of the driving laser. Spectral measurements of the laser after the capillary show significant spectral broadening and blueshifting without the discharge, as shown in Fig. 5.12. In contrast, when the discharge is running, the fundamental laser spectrum shows a very small change in spectrum from that observed from an evacuated capillary.

5.5.2 FROG measurements

Frequency resolved optical gating (FROG) measurements of the exiting pulse were taken for the same conditions as the harmonic spectra. Figure 5.13 shows the reconstructed pulse intensities for an evacuated capillary and for the discharge at the optimal time delay with full-width-half-maximum (FWHM) measurements of 32 and 22 fs, respectively. The FROG errors were fairly high (1–2%) for all the reconstructions, mainly due to the low dynamic range of the CCD camera used for recording the FROG traces. A comparison of the measured and reconstructed FROG traces shows that they exhibit the same main features, but due to slight differences the estimated measurement error is ± 5 fs. FROG measurements were taken for a xenon filled, hollow waveguide without the discharge. The intensity of the pulses was large enough, and the SPM so severe, that the pulse would break up temporally, resulting in an inability to reconstruct the measured FROG traces. Therefore, a comparison could only be made between the evacuated capillary and the xenon filled capillary with the preionizing discharge. These results show that the discharge does not aversely affect the temporal structure of the driving laser and it may shorten the pulse duration.

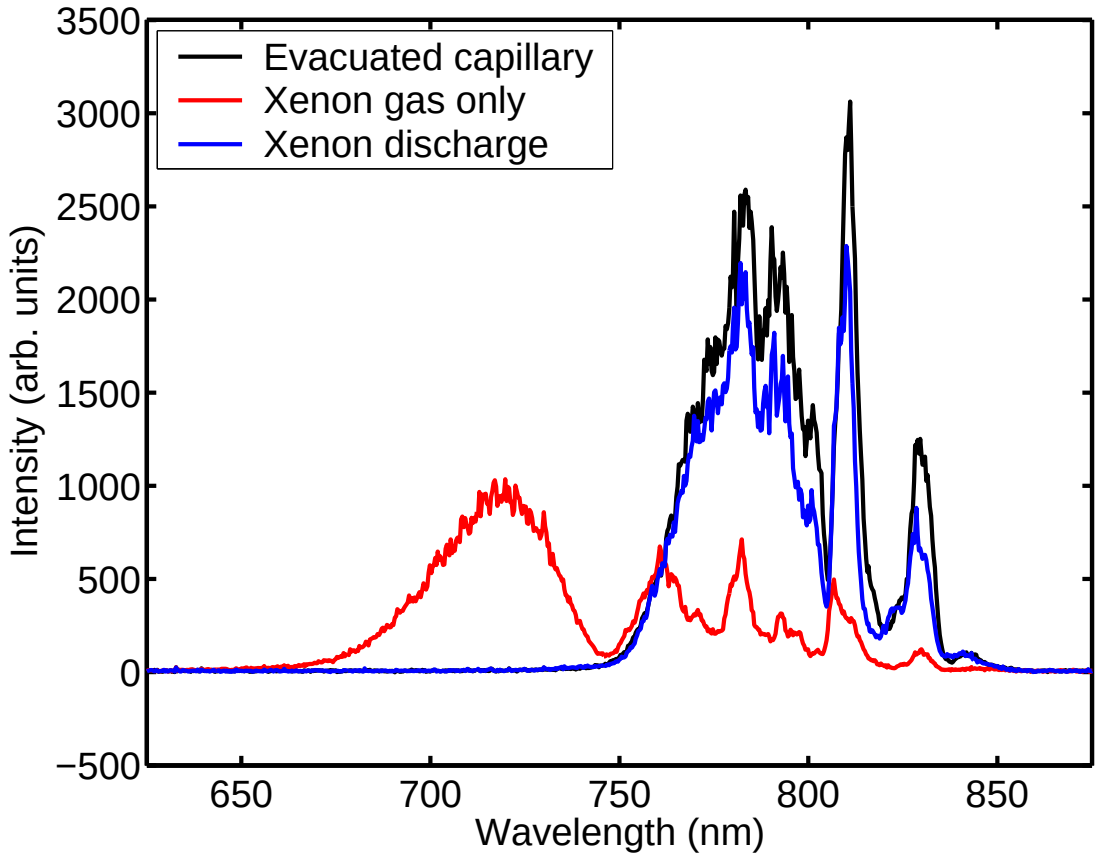

Figure 5.12: Spectral measurements of the driving laser field through an evacuated capillary (black), a xenon filled capillary with no discharge (red), and a xenon filled capillary with discharge at the optimal time delay (blue). (Adapted from Fig. 3 of [1])

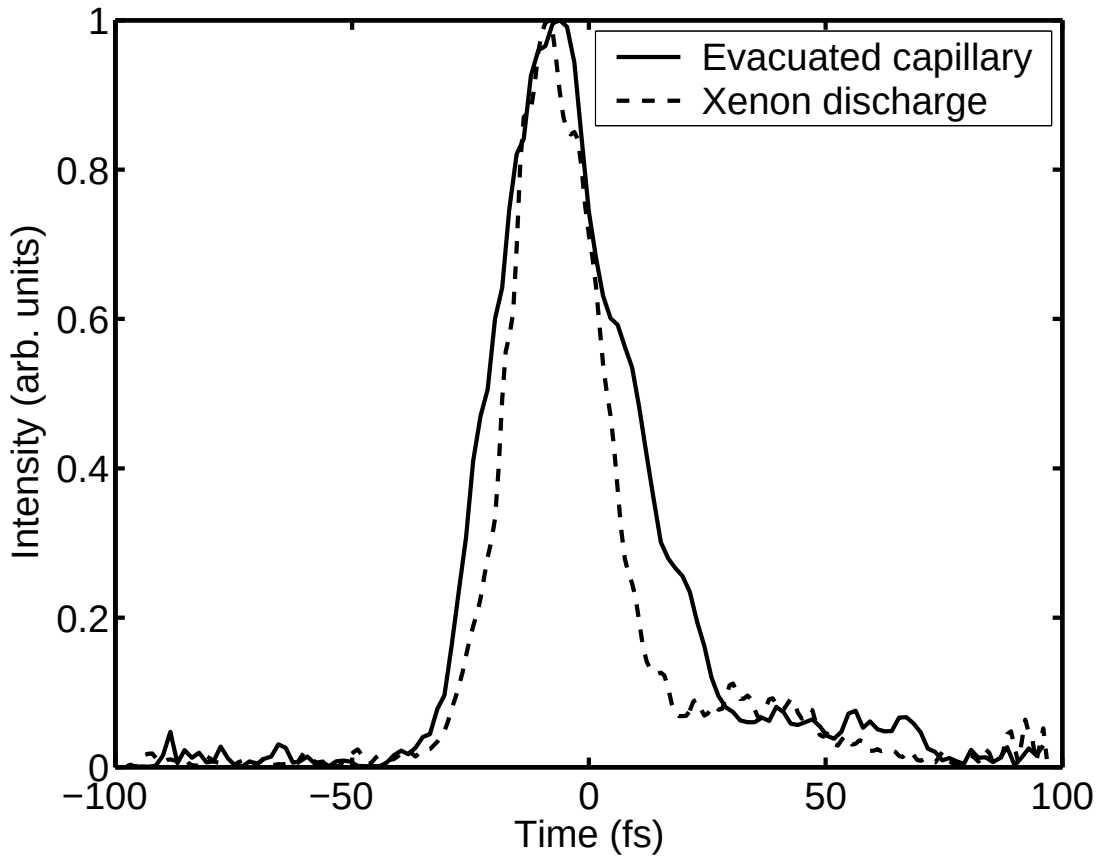

Figure 5.13: Reconstructed FROG pulse intensities for an evacuated capillary (solid) and for the discharge at optimal timing (dashed).

5.5.3 Phasemismatch of lower order harmonics

Another feature of the data in Fig. 5.10 is that, at the lowest photon energies (<50 eV), the harmonic signal decreases substantially with the discharge. In this spectral region, harmonic emission without the discharge is primarily from ionization of neutrals. However, when the discharge is initiated under these conditions, the neutral atom population is depleted. Although HHG from ions will also generate photons in this energy range with comparable single-atom response, the emission occurs in a plasma with significantly shorter coherence length (∼1 mm with the discharge on as opposed to ∼5 mm without the discharge for the 19th harmonic) than in a neutral gas, thereby reducing the overall efficiency.

5.5.4 Temporal evolution of the harmonic extension

Figure 5.14 further illustrates the optimum plasma conditions for harmonic generation. Figure 5.14(a) shows the harmonic signal at 120 ± 2 eV, together with the current pulse temporal profile. It is clear that the efficient generation and detection of the highest photon energies is well localized within the time of the current pulse. The intensity of this harmonic signal is zero before the onset of the current pulse, increases after this onset, reaches a peak at a delay of 2 μs, and then quickly decays back to zero. As mentioned before, this increase is due to a minimization of defocusing and ionization losses. This localization within the time window of the discharge current pulse is an indication that the highest observable harmonics are generated solely from ions. This clearly shows the advantages of generating harmonics in a capillary discharge. One might expect the most efficient generation of the highest photon energies to occur when the ion population is at a maximum (i.e. near the rising edge of the current pulse), but the data indicates that the most efficient generation is delayed with respect to the rising edge. It is possible that the delay of the maximum HHG signal is due to the

presence of plasma non-uniformities caused by the fast rise time of the current pulse. These non-uniformities can hinder or disrupt the generation of the harmonic signal.

5.5.5 Time resolved visible spectroscopy

In order to further verify that the extended harmonic signal is from ions, the time resolved visible spectra of the discharge plasma were measured (Fig. 5.15) using the same conditions as the HHG experiment. The spectrometer was tuned to the blue region of the visible spectrum (∼425 nm) for the spectral lines of Xe II and III, and it was tuned to the red region (∼825 nm) for the spectral lines of Xe I. A BG-39 filter was used to prevent contamination of the Xe II and III signal by the 2^{nd} order of the Xe I lines. Due to much lower signal, the gate window width and integration times for these spectra were 100 ns gate, 10 s integration for the blue spectra and 500 ns gate, 50 s integration for the red spectra. The strength of different atomic spectral lines for different ion species was measured as a function of time delay after the onset of the discharge current pulse. Figure 5.14(b) shows selected visible emission lines from Xe I (823.16 nm), II (418.01 nm), and III (410.92 nm) on the same time scale. These lines were chosen for the strength of the signal and the distance from the spectral lines of other species, making identification unambiguous. All the spectra were normalized to the signal of the strongest ion signal, Xe III in this case. It can be seen that the signal from neutral xenon is fairly weak throughout the current pulse, while the Xe II and III signal follows the contours of the current pulse fairly closely. Early in the current pulse there is a significant population of Xe III, which may be another cause of the peak harmonic signal being delayed with respect to the peak of the visible ion spectroscopy. The over-ionized plasma results in an increased electron density and, therefore, a larger phase mismatch between the driving laser pulse and the generated harmonics. The strongest harmonic signal is observed when the visible ion signal has dropped to $\sim 1/2$ of the peak value.

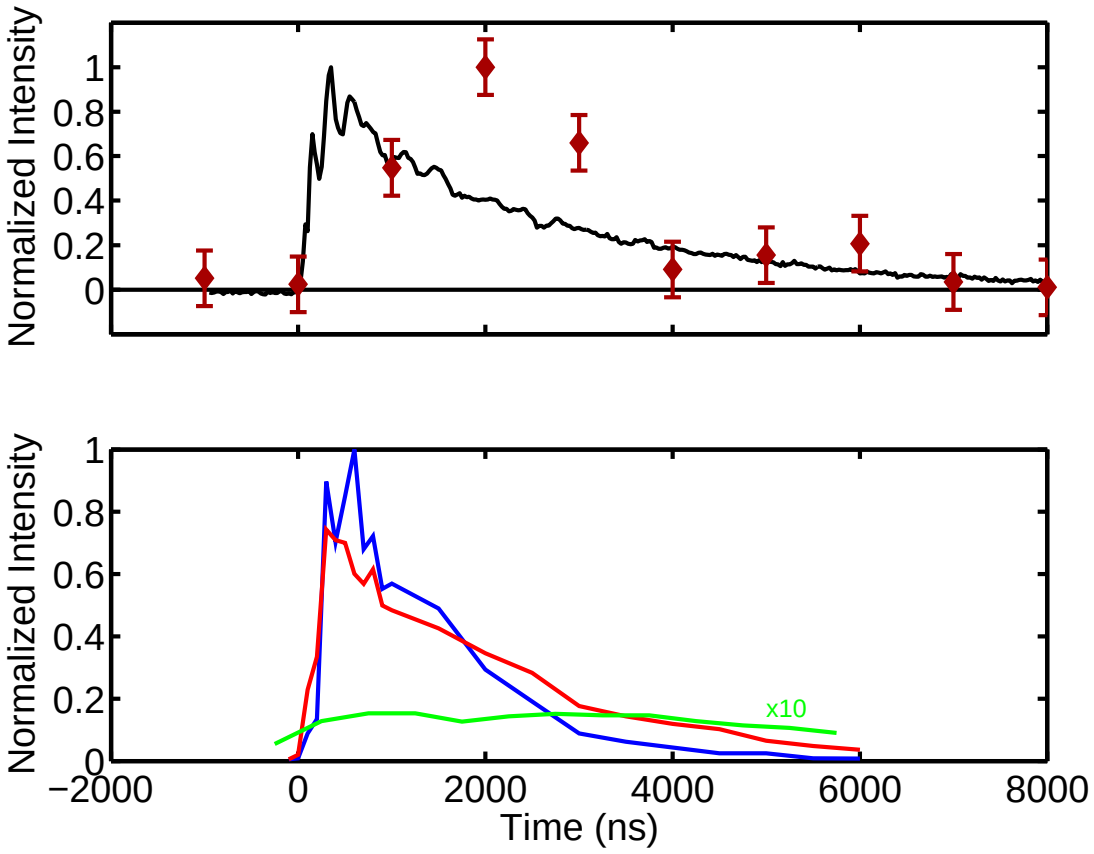

Figure 5.14: (a) Time evolution of the harmonic signal at 120 ± 2 eV (maroon diamonds). The current pulse is shown for reference (black). (b) Time evolution of the visible emission lines from Xe I (823.16 nm) (green), Xe II (418.01 nm) (red), and Xe III (410.92 nm) (blue). (Adapted from Fig. 4 of [1])

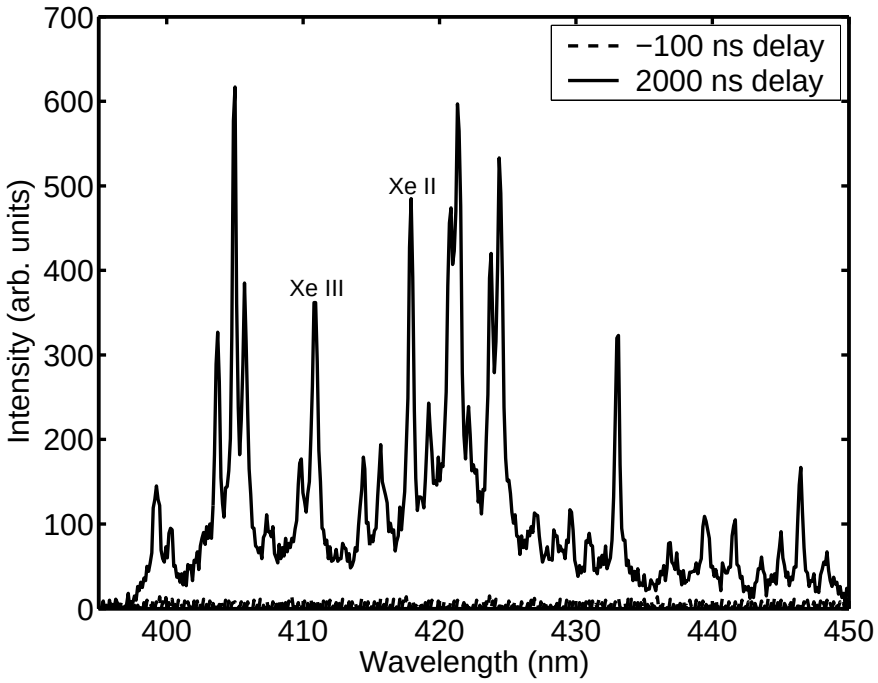

(a)

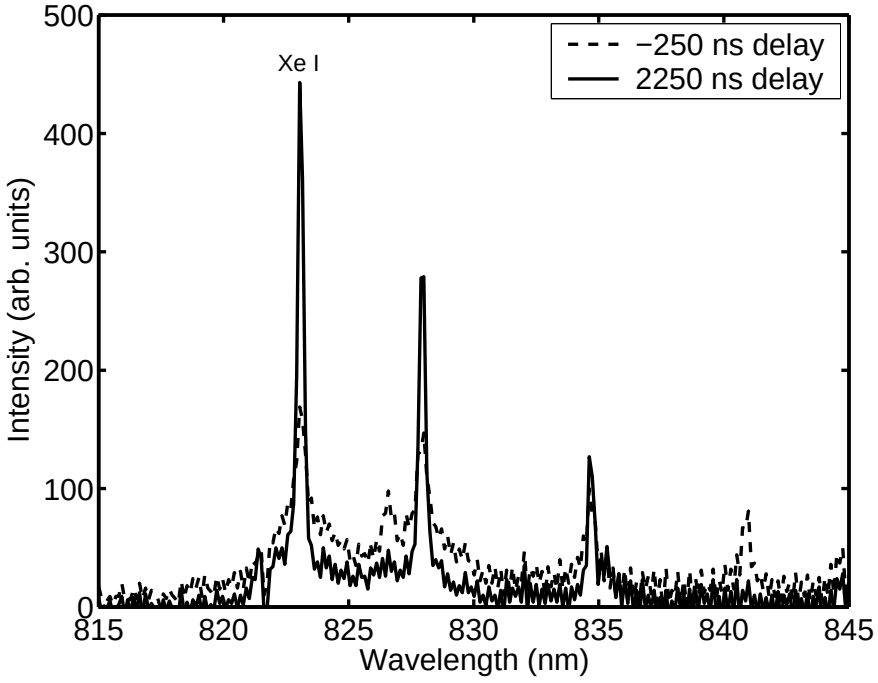

(b)

Figure 5.15: (a) Sample visible blue spectra at -100 ns delay (dashed) and 2000 ns delay (solid).(b) Sample visible red spectra at -250 ns delay (dashed) and 2250 ns delay (solid). These spectra show the large change in spectral lines associated with xenon ions, while the neutral spectral line emission does not change significantly. The spectral lines used for Figure 5.14 are noted.

These spectroscopic measurements and model calculations with a combined hydrodynamic and atomic physics code developed at Colorado State University [132] show that the discharge plasma is completely ionized in the center region of the capillary at a time delay of 2 μs, corresponding to the observed maximum of the harmonic signal. The model is consistent with the relative Xe I, Xe II, and Xe III line intensity measurements of figure 5.14(b). In contrast to the spectroscopy of the pulsed discharge, the spectrum of the plasma created by the small simmer current shows very strong Xe I lines, with weaker Xe II and III lines. Finally, calculation of well established ADK strong-field ionization rates show that all harmonics from xenon gas at energies > 75 eV are produced under conditions where the neutral xenon has already been completely depleted ($> 99\%$) [107]. These results show that the highest energy harmonics observed were generated exclusively from ions.

5.6 Conclusion

It has been confirmed that a capillary discharge plasma has the correct electron density profile for the guiding of a high intensity laser pulse. Also, it has been demonstrated that harmonic generation from xenon ions in a capillary discharge plasma can significantly extend the highest observable harmonic to shorter wavelengths by a factor of two compared with previous measurements. We have observed an extension of the highest observable harmonic by $\sim$80 eV, from 70 to 150 eV, over previous experiments, as well as an enhancement of the flux of the harmonics in the 95 ± 1 eV region by nearly two orders of magnitude. The presence of the discharge reduces phase modulation of the driving laser and increases the laser intensity available for harmonic generation, producing shorter wavelength harmonics.

Chapter 6

Conclusion

In conclusion, this thesis reports on significant advancements in the fields of ultrafast laser design and high harmonic generation. First, this work developed a novel technique, down-chirped pulse amplification (DPA), for the amplification of ultrashort pulses. This new technique allows for an increase in the output energy of some existing amplifiers by approximately a factor of two in a simpler, more compact design. Second, this novel design has been implemented in a amplifier that is scalable to repetition rates of tens of kilohertz, a previously unexplored regime of ultrafast laser operation. In this repetition range, pulse energies of a few hundred microjoules are possible. This type of system has many advantages in the areas of biology, chemistry, and physics where large pulse energies are not required, but high repetition rates are desirable for reasons of averaging and signal acquisition time. The DPA design has the potential to expand the usefulness of ultrafast lasers to other scientific disciplines due to the minimal adjustments in the stretcher and compressor.

Lastly, the work demonstrating the first evidence of high harmonic generation (HHG) from ions in a capillary discharge has many possibilities for applications as well as the advancement of basic science. First and foremost, it demonstrates a technique by which higher photon energies may be generated from existing amplifier systems. It may be possible to generate harmonics in previously inaccessible spectral regions using this technique. Initial measurements indicate that this technique can be extended to

other noble gases, such as krypton and argon, with similar results. In addition, by combining this technique with that of quasi-phase matching, it would be possible to efficiently generate harmonics in a wider range of spectral frequencies. Simulations of counter-propagating and two-color quasi-phase matching techniques indicate that it is possible to greatly increase the signal from ions, even in the water-window region of the spectrum (2.4–4 nm).

This work represents advances in both ultrafast laser technology and its application, and has the potential to further advance fundamental scientific knowledge as well as technology.

Bibliography

[1] D. M. Gaudiosi, B. Reagan, T. Popmintchev, M. Grisham, M. Berrill, O. Cohen, B. C. Walker, M. M. Murnane, H. C. Kapteyn, and J. J. Rocca, "High-order harmonic generation from ions in a capillary discharge," Physical Review Letters, vol. 96, no. 20, p. 203001, 2006.

[2] R. Jimenez, D. A. Case, and F. E. Romesberg, "Flexibility of an anitbody binding site measured with photon echo spectrscopy," Journal of Physical Chemistry B, vol. 106, no. 5, pp. 1090–1103, 2002.

[3] C.-F. Lei, M. Bauer, K. Read, R. Tobey, Y. Liu, T. Popmintchev, M. M. Murnane, and H. C. Kapteyn, "Hot-electron-driven charge transfer processes on O2/Pt(111) surface probed by ultrafast extreme-ultraviolet pulses," Physical Review B, vol. 66, no. 24, p. 245420, 2002.

[4] S. Nolte, C. Momma, H. Jacobs, and A. Tünnermann, "Ablation of metals by ultrashort laser pulses," Journal of the Optical Society of America B, vol. 14, no. 10, pp. 2716–2722, 1997.

[5] C. Geddes, C. Toth, J. van Tilborg, E. Esarey, C. Schroeder, D. Bruhwiler, C. Nieter, J. Cary, and W. Leemans, "High-quality electron beams from a laser wakefield accelerator using plasma-channel guiding," Nature, vol. 431, pp. 538–541, 2004.

[6] H. C. Kapteyn, M. M. Murnane, and I. P. Christov, "Extreme nonlinear optics: Coherent x-rays from lasers," Physics Today, vol. March Issue, pp. 39–44, 2005.

[7] D. Strickland and G. Mourou, "Compression of amplified chirped optical pulses," Optics Communications, vol. 56, no. 3, pp. 219–221, 1985.

[8] E. B. Treacy, "Optical pulse compression with diffraction gratings," IEEE Journal of Quantum Electronics, vol. QE-5, no. 9, pp. 454–458, 1969.

[9] O. E. Martinez, J. Gordon, and R. Fork, "Negative group-velocity dispersion using refraction," Journal of the Optical Society of America A, vol. 1, no. 10, pp. 1003–1006, 1984.

[10] O. E. Martinez, "Grating and prism compressors in the case of finite beam size," Journal of the Optical Society of America B, vol. 3, no. 7, pp. 929–934, 1986.

[11] O. E. Martinez, "Design of high-power ultrashort pulse amplifiers by expansion and recompression," IEEE Journal of Quantum Electronics, vol. QE-23, no. 8, pp. 1385–1387, 1987.

[12] O. E. Martinez, "3000 times grating compressor with positive group velocity dispersion: Application to fiber compensation in the 1.3-1.6 mm region," IEEE Journal of Quantum Electronics, vol. QE-23, no. 1, pp. 59–64, 1987.

[13] U. Morgner, F. X. Kärtner, S. H. Cho, Y. Chen, H. A. Haus, J. G. Fujimoto, E. P. Ippen, V. Scheuer, G. Angelow, and T. Tschudi, "Sub-two-cycle pulses from a Kerr-lens mode-locked Ti:sapphire laser," Optics Letters, vol. 24, no. 6, pp. 411–413, 1999.

[14] M. Perry, D. Pennington, B. Stuart, G. Tietbohl, J. Britten, C. Brown, S. Herman, B. Golick, M. Kartz, J. Miller, H. Powell, M. Vergino, and V. Yanovsky, "Petawatt laser pulses," Optics Letters, vol. 24, no. 3, pp. 160–162, 1999.

[15] D. M. Pennington, C. G. Brown, T. E. Cowan, S. P. Hatchett, E. Henry, S. Herman, M. Kartz, M. Key, J. Koch, A. J. MacKinnon, M. Perry, T. W. Phillips, M. Roth, T. C. Sangster, M. Singh, R. A. Snavely, M. Stoyer, B. Stuart, and S. C. Wilks, "Petawatt laser system and experiments," IEEE Journal of Selected Topics in Quantum Electronics, vol. 6, no. 4, pp. 676–688, 2000.

[16] M. Bauer, "Femtosecond ultraviolet photoelectron spectroscopy of ultra-fast surface processes," Journal of Physics D - Applied Physics, vol. 38, no. 16, pp. R253–R267, 2005.

[17] R. A. Bartels, A. Paul, H. Green, H. C. Kapteyn, M. M. Murnane, S. Backus, I. P. Christov, Y. Liu, D. Attwood, and C. Jacobsen, "Generation of spatially coherent light at extreme ultraviolet wavelengths," Science, vol. 297, no. 5580, pp. 376–378, 2002.

[18] R. Velotta, N. Hay, M. Mason, M. Castillejo, and J. Marangos, "High-order harmonic generation in aligned molecules," Physical Review Letters, vol. 87, no. 18, p. 183901, 2001.

[19] J. Itatani, J. Levesque, D. Zeidler, H. Niikura, H. Ppin, J. Kieffer, P. Corkum, and D. Villeneuve, "Tomographic imaging of molecular orbitals," Nature, vol. 432, no. 7019, pp. 867–871, 2004.

[20] A. McPherson, G. Gibson, H. Jara, U. Johann, T. Luk, I. McIntyre, K. Boyer, and C. Rhodes, "Studies of multiphoton production of vacuum-ultraviolet radiation in the rare gases," Journal of the Optical Society of America B, vol. 4, no. 4, pp. 595–601, 1987.

[21] M. Ferray, A. L'Huillier, X. Li, L. Lompré, G. Mainfray, and C. Manus, "Multiple-harmonic conversion of 1064 nm radiation in rare gases," Journal of Physics B, vol. 21, no. 3, pp. L31–L35, 1988.

[22] K. C. Kulander, K. J. Schafer, and J. L. Krause, "Dynamics of short-pulse exicitation, ionization and harmonic conversion," in Super-Intense Laser-Atom Physics,

B. Piraux, A. L'Huillier, and K. Rzazewski, Eds. New York: Plenum, 1993, vol. 316, pp. 95–110.

[23] M. Lewenstein, P. Balcou, M. Y. Ivanov, A. L'Huillier, and P. Corkum, "Theory of high-harmonic generation by low-frequency laser fields," Physical Review A, vol. 49, no. 3, pp. 2117–2132, 1994.

[24] D. P. Shelton, "Nonlinear-optical susceptibilities of gases measured at 1064 and 1319 nm," Physical Review A, vol. 42, no. 5, pp. 2578–2592, 1990.

[25] C. G. Durfee III and H. Milchberg, "Light pipe for high intensity laser pulses," Physical Review Letters, vol. 71, no. 15, pp. 2409–2412, 1993.

[26] A. Zigler, Y. Ehrlich, C. Cohen, J. Krall, and P. Sprangle, "Optical guiding of high-intensity laser pulses in a long plasma channel formed by a slow capillary discharge," Journal of the Optical Society of America B, vol. 13, no. 1, pp. 68–71, 1996.

[27] D. Spence, A. Butler, and S. Hooker, "First demonstration of guiding of high-intensity laser pulses in a hydrogen-filled capillary discharge waveguide," Journal of Physics B, vol. 34, no. 21, pp. 4103–4112, 2001.

[28] B. Luther, Y. Wang, M. Marconi, J. Chilla, M. Larotonda, and J. Rocca, "Guiding of intense laser beams in highly ionized plasma columns generated by a fast capillary discharge," Physical Review Letters, vol. 92, no. 23, p. 235002, 2004.

[29] T. Ditmire, M. Hutchinson, M. Key, C. Lewis, A. MacPhee, I. Mercer, D. Neely, M. Perry, R. Smith, J. Wark, and M. Zepf, "Amplification of xuv harmonic radiation in a gallium amplifier," Physical Review A, vol. 51, no. 6, pp. R4337–R4340, 1995.

[30] P. Zeitoun, G. Faivre, S. Sebban, T. Mocek, A. Hallou, M. Fajardo, D. Aubert, P. Balcou, F. Burgy, D. Douillet, S. Kazamias, G. de Lachèze-Murel, T. Lefrou, S. le Pape, P. Mercère, H. Merdji, A. Morlens, J. Rousseau, and C. Valentin, "A high-intensity highly coherent soft x-ray femtosecond laser seeded by a high harmonic beam," Nature, vol. 431, no. 7007, pp. 426–429, 2004.

[31] T. Mocek, S. Sebban, G. Maynard, P. Zeitoun, G. Faivre, A. Hallou, M. Fajardo, S. Kazamias, B. Cros, D. Aubert, G. de Lachèze-Murel, J. Rousseau, and J. Dubau, "Absolute time-resolved x-ray laser gain measurement," Physical Review Letters, vol. 95, no. 17, p. 173902, 2005.

[32] J. J. Rocca, V. Shlyaptsev, F. Tomasel, O. Cortázar, D. Hartshorn, and J. Chilla, "Demonstration of a discharge pumped table-top soft-x-ray laser," Physical Review Letters, vol. 73, no. 16, pp. 2192–2195, 1994.

[33] J. J. Rocca, F. Tomasel, M. C. Marconi, V. Shlyaptsev, J. Chilla, B. Szapiro, and G. Giudice, "Discharge-pumped soft-x-ray laser in neon-like argon," Physics of Plasmas, vol. 2, no. 6, pp. 2547–2554, 1995.

[34] T. Norris, "Femtosecond pulse amplification at 250 kHz with a ti:sapphire regenerative amplifier and application to contiuum generation," Optics Letters, vol. 17, no. 14, pp. 1009–1011, 1992.

[35] S. Backus, C. G. Durfee III, M. M. Murnane, and H. C. Kapteyn, "High power ultrafast lasers," Review of Scientific Instruments, vol. 69, no. 3, pp. 1207–1223, 1998.

[36] S. Backus, R. A. Bartels, S. Thompson, R. Dollinger, H. C. Kapteyn, and M. M. Murnane, "High-efficiency, single-stage 7-kHz high-average-power ultrafast laser system," Optics Letters, vol. 26, no. 7, pp. 465–467, 2001.

[37] S. Backus, C. G. Durfee III, G. Mourou, H. C. Kapteyn, and M. M. Murnane, "0.2-TW laser system at 1 kHz," Optics Letters, vol. 22, no. 16, pp. 1256–1258, 1997.

[38] D. M. Gaudiosi, A. L. Lytle, P. Kohl, M. M. Murnane, H. C. Kapteyn, and S. Backus, "11-W average power Ti:sapphire amplifier system using downchirped pulse amplification," Optics Letters, vol. 29, no. 22, pp. 2665–2667, 2004.

[39] P. Maine, D. Strickland, P. Bado, M. Pessot, and G. Mourou, "Generation of ultrahigh peak power pulses by chirped pulse amplification," IEEE Journal of Quantum Electronics, vol. 24, no. 2, pp. 398–403, 1988.

[40] M. Pessot, J. Squier, P. Bado, G. Mourou, and D. J. Harter, "Chirped pulse amplification of 300 fs pulses in an alexandrite regenerative amplifier," IEEE Journal of Quantum Electronics, vol. 25, no. 1, pp. 61–66, 1989.

[41] C. Fiorini, C. Sauteret, C. Rouyer, N. Blanchot, S. Seznec, and A. Migus, "Temporal aberrations due to misalignments of a stretcher-compressor system and compensation," IEEE Journal of Quantum Electronics, vol. 30, no. 7, pp. 1662–1670, 1994.

[42] G. Pretzler, A. Kasper, and K. Witte, "Angular chirp and tilted light pulses in cpa lasers," Applied Physics B, vol. 70, no. 1, pp. 1–9, 2000.

[43] F. Salin, C. Le Blanc, J. Squier, and C. Barty, "Thermal eigenmode amplifiers for diffraction-limited amplification of ultrashort pulses," Optics Letters, vol. 23, no. 9, pp. 718–720, 1998.

[44] M. Holland, "Thermal conductivity of several optical maser materials," Journal of Applied Physics, vol. 33, pp. 2910–2911, 1962.

[45] A. DeFranzo and B. Pazol, "Index of refraction measurement on sapphire at low temperatures and visible wavelengths," Applied Optics, vol. 32, no. 13, pp. 2224–2234, 1993.

[46] R. Huber, F. Adler, and A. Leitenstorfer, "12-fs pulses from a continuous-wave-pumped 200-nJ Ti:sapphire amplifier at a variable repetition rate as high as 4 mhz," Optics Letters, vol. 28, no. 21, pp. 2118–2120, 2003.

[47] F. Helbing, G. Steinmeyer, J. Stenger, H. Telle, and U. Keller, "Carrier-envelope-offset dynamics and stabilization of femtosecond pulses," Applied Physics B, vol. 74, pp. S35–S42, 2002.

[48] I. Thomann, E. Gagnon, R. Jones, A. Sandu, A. L. Lytle, R. Anderson, J. Ye, M. M. Murnane, and H. C. Kapteyn, "Investigation of a grating-based stretcher/compressor for carrier-envelope phase stabilized fs pulses," Optics Express, vol. 12, no. 15, pp. 3493–3499, 2004.

[49] E. Gagnon, I. Thomann, A. Paul, A. L. Lytle, S. Backus, M. M. Murnane, H. C. Kapteyn, and A. Sandu, "Long-term carrier-envelope phase stability from a grating-based, chirped pulse amplifier," Optics Letters, vol. 31, no. 12, pp. 1866–1868, 2006.

[50] C. Spielmann, M. Lenzner, F. Krausz, and R. Szipöcs, "Compact, high-throughput expansion-compression scheme for chirped pulse amplification in the 10 fs range," Optics Communications, vol. 120, pp. 321–324, 1995.

[51] A. Dubietis, G. Jonuˇ sauskas, and A. Piskarskas, "Powerful femtosecond pulse generation by chirped and stretched pulse parametric amplification in bbo crystal," Optics Communications, vol. 88, no. 4-6, pp. 437–440, 1992.

[52] I. N. Ross, P. Matousek, G. H. New, and K. Osvay, "Analysis and optimization of optical parametric chirped pulse amplification," Journal of the Optical Society of America B, vol. 19, no. 12, pp. 2945–2956, 2002.

[53] N. Ishii, L. Turi, V. S. Yakovlev, T. Fuji, F. Krausz, A. Baltuˇ ska, R. Butkus, G. Veitas, V. Smilgeviˇ cius, R. Danielius, and A. Piskarskas, "Multimillijoule chirped parametric amplification of few-cycle pulses," Optics Letters, vol. 30, no. 5, pp. 567–569, 2005.

[54] S. Witte, R. T. Zinkstok, W. Hogervorst, and K. S. E. Eikema, "Generation of few-cycle terawatt light pulses using optical parametric chirped pulse amplification," Optics Express, vol. 13, no. 13, pp. 4903–4908.

[55] M. T. Asaki, C.-P. Huang, D. Garvey, J. Zhou, H. C. Kapteyn, and M. M. Murnane, "Generation of 11-fs pulses from a self-mode-locked ti:sapphire laser," Optics Letters, vol. 18, no. 12, pp. 977–979, 1993.

[56] From the Schott Optical Glass Catalog: http://www.us.schott.com/optics%5Fdevices/english/download/catalog%5Foptical%5Fglass%5Finformations%5Fusa%

[57] D. N. Nikogosyan, Properties of Optical and Laser-Related Materials: A Handbook. John Wiley and Sons, 1997.

[58] E. R. Van Keuren, "Refractive index measurement using total internal reflection," American Journal of Physics, vol. 73, no. 7, pp. 611–614, 2005.

[59] D. J. Kane and R. Trebino, "Characterization of arbitrary femtosecond pulses using frequency-resolved optical gating," IEEE Journal of Quantum Electronics, vol. 29, no. 2, pp. 571–579, 1993.

[60] A. Efimov, M. D. Moores, N. M. Beach, J. L. Krause, and D. H. Reitze, "Adaptive control of pulse phase in a chirped-pulse amplifier," Optics Letters, vol. 23, no. 24, pp. 1915–1917, 1998.

[61] M. Dugan, J. Tull, and W. Warren, "High-resolution acoutso-optic shaping of unamplified and amplified femtosecond laser pulses," Journal of the Optical Society of America B, vol. 14, no. 9, pp. 2348–2358, 1997.

[62] E. Zeek, R. A. Bartels, M. M. Murnane, H. C. Kapteyn, and S. Backus, "Adaptive pulse compression for transform-limited 15-fs high-energy pulse generation," Optics Letters, vol. 25, no. 8, pp. 587–589, 2000.

[63] K.-H. Hong, S. Kostritsa, T. J. Yu, J. H. Sung, I. W. Choi, Y.-C. Noh, D.-K. Ko, and J. Lee, "100-kHz high-power femtosecond Ti:sapphire laser based on downchirped regenerative amplification," Optics Express, vol. 14, no. 2, pp. 970–978, 2006.

[64] A. Galvanauskas, G. C. Cho, A. Hariharan, M. E. Fermann, and D. Harter, "Generation of high-energy femtosecond pulses in multimode-core Yb-fiber chirped-pulse amplification systems," Optics Letters, vol. 26, no. 12, pp. 935–937, 2001.

[65] J. Takayanagi, N. Nishizawa, H. Nagai, M. Yoshida, and T. Goto, "Generation of high-power femtosecond pulse and octave-spanning ultrabroad supercontinuum using all-fiber system," IEEE Photonics Technology Letters, vol. 17, no. 1, pp. 37–39, 2005.

[66] N. Zhavoronkov and G. Korn, "Regenerative amplification of femtosecond laser pulses in ti:sapphire at multikilohertz repetition rates," Optics Letters, vol. 29, no. 2, pp. 198–200, 2004.

[67] J. Squier, G. Korn, G. Mourou, G. Vaillancourt, and M. Bouvier, "Amplification of femtosecond pulses at 10-kHz repetition rates in Ti:Al2O3," Optics Letters, vol. 18, no. 8, pp. 625–627, 1993.

[68] D. M. Gaudiosi, E. Gagnon, A. L. Lytle, J. L. Fiore, E. A. Gibson, S. Kane, J. Squier, M. M. Murnane, H. C. Kapteyn, R. Jimenez, and S. Backus, "Multikilohertz repetition rate ti:sapphire amplifier based on down-chirped pulse amplification," Optics Express, vol. 14, no. 20, pp. 9277–9283, 2006.

[69] E. A. Gibson, D. M. Gaudiosi, H. C. Kapteyn, R. Jimenez, S. Kane, R. Huff, C. G. Durfee III, and J. Squier, "Efficient reflection grisms for pulse compression and dispersion compensation for femtosecond pulses," Optics Letters, vol. 31, no. 22, pp. 3363–3365, 2006.

[70] S. Kane and J. Squier, "Grating compensation of third-order material dispersion in the normal dispersion regime: Sub-100-fs chirped-pulse amplification using a fiber stretcher and grating-pair compressor," IEEE Journal of Quantum Electronics, vol. 31, no. 11, pp. 2052–2057, 1995.

[71] S. Backus, J. Peatross, C.-P. Huang, H. C. Kapteyn, and M. M. Murnane, "Ti:sapphire amplifier producing millijoule-level, 21-fs pulses at 1 kHz," Optics Letters, vol. 20, no. 19, pp. 2000–2002, 1995.

[72] L. M. Frantz and J. S. Nodvik, "Theory of pulse propagation in a laser amplifier," Journal of Applied Physics, vol. 34, no. 8, pp. 2346–2349, 1963.

[73] A. L'Huillier, P. Balcou, and L. Lompré, "Coherence and resonance effects in high-order harmonic generation," Physical Review Letters, vol. 68, no. 2, pp. 166–169, 1992.

[74] A. L'Huillier and P. Balcou, "High-order harmonic generation in rare gases with a 1-ps 1053-nm laser," Physical Review Letters, vol. 70, no. 6, pp. 774–777, 1993.

[75] A. L'Huillier, M. Lewenstein, P. Salières, P. Balcou, M. Y. Ivanov, J. Larsson, and C. Wahlström, "High-order harmonic-generation cutoff," Physical Review A, vol. 48, no. 5, pp. R3433–R3436, 1993.

[76] C. Wahlström, J. Larsson, A. Persson, T. Starczewski, S. Svanberg, P. Salières, P. Balcou, and A. L'Huillier, "High-order harmonic generation in rare gases with an intense short-pulse laser," Physical Review A, vol. 48, no. 6, pp. 4709–4720, 1993.

[77] J. Macklin, J. Kmetec, and C. Gordon III, "High-order harmonic generation using intense femtosecond pulses," Physical Review Letters, vol. 70, no. 6, pp. 766–769, 1993.

[78] J. Zhou, J. Peatross, M. M. Murnane, H. C. Kapteyn, and I. P. Christov, "Enhanced high-harmonic generation using 25 fs laser pulses," Physical Review Letters, vol. 76, no. 5, pp. 752–755, 1996.

[79] C. Spielmann, C. Kan, N. H. Burnett, T. Brabec, M. Geissler, A. Scrinzi, M. Schnrer, and F. Krausz, "Near-keV coherent x-ray generation with sub-10-fs lasers," IEEE Journal of Selected Topics in Quantum Electronics, vol. 4, no. 2, pp. 249–265, 1998.

[80] A. Rundquist, C. G. Durfee III, Z. Chang, C. Herne, S. Backus, M. M. Murnane, and H. C. Kapteyn, "Phase-matched generation of coherent soft x-rays," Science, vol. 280, pp. 1412–1415, 1998.

[81] E. Constant, D. Garzella, P. Breger, E. Mével, C. Dorrer, C. Le Blanc, F. Salin, and P. Agostini, "Optimizing high harmonic generation in absorbling gases: model and experiment," Physical Review Letters, vol. 82, no. 8, pp. 1668–1671, 1999.

[82] H. Lange, A. Chiron, J.-F. Ripoche, A. Mysyrowicz, P. Breger, and P. Agostini, "High-order harmonic generation and quasiphase matching in xenon using self-guided femtosecond pulses," Physical Review Letters, vol. 81, no. 8, pp. 1611–1613, 1998.

[83] K. Midorikawa, Y. Tamaki, J. Itatani, Y. Nagata, and M. Obara, "Phase-matched high-order harmonic generation by guided intense femtosecond pulses," IEEE Journal of Selected Topics in Quantum Electronics, vol. 5, no. 6, pp. 1475–1485, 1999.

[84] P. Salières, A. L'Huillier, and M. Lewenstein, "Coherence control of high-order harmonics," Physical Review Letters, vol. 74, no. 19, pp. 3776–3779, 1995.

[85] I. Mercer, E. Mével, R. Zerne, A. L'Huillier, P. Antoine, and C. Wahlström, "Spatial mode control of high-order harmonics," Physical Review Letters, vol. 77, no. 9, pp. 1731–1734, 1996.

[86] R. A. Bartels, S. Backus, E. Zeek, L. Misoguti, G. Vdovin, I. P. Christov, M. M. Murnane, and H. C. Kapteyn, "Shaped-pulse optimization of coherent emission of high-harmonic soft x-rays," Nature, vol. 406, no. 6792, pp. 164–166, 2000.

[87] C. Wahlström, S. Borgström, J. Larsson, and S. Pettersson, "High-order harmonic generation in laser-produced ions using a near-infrared laser," Physical Review A, vol. 51, no. 1, pp. 585–591, 1995.

[88] E. A. Gibson, A. Paul, N. Wagner, R. Tobey, S. Backus, I. P. Christov, M. M. Murnane, and H. C. Kapteyn, "High-order harmonic generation up to 250 eV from highly ionized argon," Physical Review Letters, vol. 92, no. 3, p. 033001, 2004.

[89] K. Krusheknick, W. Tighe, and S. Suckewer, "Harmonic generation from ions in underdense aluminim and lithium-fluorine plasmas," Journal of the Optical Society of America B, vol. 14, no. 7, pp. 1687–1691, 1997.

[90] J.-F. Hergott, M. Kovacev, H. Merdji, C. Hubert, Y. Mairesse, E. Jean, P. Breger, P. Agostini, B. Carré, and P. Salières, "Extreme-ultraviolet high-order harmonic pulses in the microjoule range," Physical Review A, vol. 66, no. 2, p. 021801, 2002.

[91] E. A. Gibson, A. Paul, N. Wagner, R. Tobey, D. Gaudiosi, S. Backus, I. P. Christov, A. Aquila, E. M. Gullikson, D. T. Attwood, M. M. Murnane, and H. C. Kapteyn, "Coherent soft x-ray generation in the water window with quasi-phase matching," Science, vol. 302, no. 5642, pp. 95–98, 2003.

[92] E. Seres, J. Seres, F. Krausz, and C. Spielmann, "Generation of coherent soft-x-ray radiation extending far beyond the titanium L edge," Physical Review Letters, vol. 92, no. 16, p. 163002, 2004.

[93] J. Seres, E. Seres, A. Verhoef, G. Tempea, C. Streli, P. Wobrauschek, V. Yakovlev, A. Scrinzi, C. Spielmann, and F. Krausz, "Source of coherent kiloelectronvolt x-rays," Nature, vol. 433, no. 7026, p. 596, 2005.

[94] K. C. Kulander and B. W. Shore, "Calculations of multiple-harmonic conversion of 1064-nm radiation in Xe," Physical Review Letters, vol. 62, no. 5, pp. 524–526, 1989.

[95] A. L'Huillier, K. J. Schafer, and K. C. Kulander, "Theoretical aspects of intense field harmonic generation," Journal of Physics B, vol. 24, pp. 3315–3341, 1991.

[96] A. L'Huillier, K. J. Schafer, and K. C. Kulander, "High-order harmonic generation in xenon at 1064 nm: The role of phase matching," Physical Review Letters, vol. 66, no. 17, pp. 2200–2203, 1991.

[97] J. L. Krause, K. J. Schafer, and K. C. Kulander, "High-order harmonic generation from atoms and ions in the high intensity regime," Physical Review Letters, vol. 68, no. 24, pp. 3535–3538, 1992.

[98] A. L'Huillier, P. Balcou, S. Candel, K. J. Schafer, and K. C. Kulander, "Calculations of high-order harmonic-generation processes in xenon at 1064 nm," Physical Review A, vol. 46, no. 5, pp. 2778–2790, 1992.

[99] P. Corkum, "Plasma perspective on strong-field multiphoton ionization," Physical Review Letters, vol. 71, no. 13, pp. 1994–1997, 1993.

[100] S. Rae, K. Burnett, and J. Cooper, "Generation and propagation of high-order harmonics in a rapidly ionizing medium," Physical Review A, vol. 50, no. 4, pp. 3438–3446, 1994.

[101] K. C. Kulander and K. J. Schafer, "Time-dependent calculations of electron and photon emision from an atom in an intense laser field," Atoms and Molecules in Intense Fields: Structure and Bonding, vol. 86, pp. 149–172, 1997.

[102] I. P. Christov, M. M. Murnane, and H. C. Kapteyn, "High-harmonic generation of attosecond pulses in the "single-cycle" regime," Physical Review Letters, vol. 78, no. 7, pp. 1251–1254, 1997.

[103] I. P. Christov, M. M. Murnane, and H. C. Kapteyn, "Generation and propagation of attosecond x-ray pulses in gaseous media," Physical Review A, vol. 57, no. 4, pp. R2285–R2288, 1998.

[104] M. Geissler, G. Tempea, and T. Brabec, "Phase-matched high-order harmonic generation in the nonadiabatic limit," Physical Review A, vol. 62, no. 3, p. 033817, 2000.

[105] G. Tempea and T. Brabec, "Optimization of high-harmonic generation," Applied Physics B, vol. 70, no. Suppl., pp. S197–S202, 2000.

[106] J. Gao, F. Shen, and J. Eden, "Interpretation of high-order harmonic generation in terms of transistions between quantum volkov states," Physical Review A, vol. 61, no. 4, p. 043812, 2000.

[107] M. Ammosov, N. Delone, and V. Kraĭnov, "Tunnel ionization of complex atoms and of atomic ions in an alternating electromagnetic field," Sov. Phys. JETP, vol. 64, no. 6, pp. 1191–1194, 1986.

[108] A. Scrinzi, M. Geissler, and T. Brabec, "Ionization above the coulomb barrier," Physical Review Letters, vol. 83, no. 4, pp. 706–709, 1999.

[109] P. Balcou, P. Salières, A. L'Huillier, and M. Lewenstein, "Generalized phase-matching conditions for high harmonics: The role of field-gradient forces," Physical Review A, vol. 55, no. 4, pp. 3204–3210, 1997.

[110] M. Lewenstein, P. Salières, and A. L'Huillier, "Phase of the atomic polarization in high-order harmonic generation," Physical Review A, vol. 52, no. 6, pp. 4747–4754, 1995.

[111] M. Perry and J. K. Crane, "High-order harmonic emission from mixed fields," Physical Review A, vol. 48, no. 6, pp. r4051–r4054, 1993.

[112] M. Nisoli, S. De Silvestri, O. Svelto, R. Szipöcs, K. Ferencz, C. Spielmann, S. Sartania, and F. Krausz, "Compression of high-energy laser pulses below 5 fs," Optics Letters, vol. 22, no. 8, pp. 522–524, 1997.

[113] E. A. J. Marcatili and R. A. Schmeltzer, "Hollow metallic and dielectric waveguides for long distance optical transmission and lasers," Bell System Technical Journal, vol. 43, pp. 1783–1809, 1964.

[114] S. Rae, "Ionization-induced defocusing of intense laser-pulses in high-pressure gases," Optics Communications, vol. 97, no. 1-2, pp. 25–28, 1993.

[115] A. Paul, R. A. Bartels, R. Tobey, H. Green, S. Weiman, I. P. Christov, M. M. Murnane, H. C. Kapteyn, and S. Backus, "Quasi-phase-matched generation of coherent extreme-ultraviolet light," Nature, vol. 421, no. 6918, pp. 51–54, 2003.

[116] C. E. Max and J. Arons, "Self-modulation and self-focusing of electromagnetic waves in plasmas," Physical Review Letters, vol. 33, no. 4, pp. 209–212, 1974.

[117] G.-Z. Sun, E. Ott, Y. Lee, and P. Guzdar, "Self-focusing of short intense pulses in plasmas," Physics of Fluids, vol. 30, no. 2, pp. 526–532, 1987.

[118] P. Sprangle, E. Esarey, and A. Ting, "Nonlinear theory of intense laser-plasma interactions," Physical Review Letters, vol. 64, no. 17, pp. 2011–2014, 1990.

[119] P. Sprangle and E. Esarey, "Interaction of ultrahigh laser fields with beams and plasmas," Physics of Fluids, vol. 4, no. 7, pp. 2241–2248, 1992.

[120] E. Esarey, J. Krall, and P. Sprangle, "Envelope analysis of intense laser pulse self-modulation in plasmas," Physical Review Letters, vol. 72, no. 18, pp. 2887–2890, 1994.

[121] J. Krall, E. Esarey, P. Sprangle, and G. Joyce, "Propagation of radius-tailored laser pulses over extended distances in a uniform plasma," Physics of Plasmas, vol. 1, no. 5, pp. 1738–1743, 1994.

[122] E. Esarey, P. Sprangle, J. Krall, and A. Ting, "Self-focusing and guiding of short laser pulses in ionizing gases and plasmas," IEEE Journal of Selected Topics in Quantum Electronics, vol. 33, no. 11, pp. 1879–1914, 1997.

[123] C. G. Durfee III, J. Lynch, and H. Milchberg, "Mode properties of a plasma waveguide for intense laser pulses," Optics Letters, vol. 19, no. 23, pp. 1937–1939, 1994.

[124] C. G. Durfee III, J. Lynch, and H. Milchberg, "Development of a plasma waveguide for high-intensity laser pulses," Physical Review E, vol. 51, no. 3, pp. 2368–2389, 1995.

[125] Y. Ehrlich, C. Cohen, A. Zigler, J. Krall, P. Sprangle, and E. Esarey, "Guiding of high intensity laser pulses in straight and curved plasma channel experiments," Physical Review Letters, vol. 77, no. 20, pp. 4186–4189, 1996.

[126] K. C. Kulander and T. Rescigno, "Effective potentials for time-dependent calculations of multiphoton processes in atoms," Computer Physics Communications, vol. 63, no. 1-3, pp. 523–528, 1991.

[127] A. Fedotov, S. Gladkov, N. Koroteev, and A. Zheltikov, "Highly efficient frequency tripling of laser radiation in a low-temperature laser-produced gaseous plasma," Journal of the Optical Society of America B, vol. 8, no. 2, pp. 363–366, 1991.

[128] Y. Akiyama, K. Midorikawa, Y. Matsunawa, Y. Nagata, M. Obara, H. Tashiro, and K. Toyoda, "Generation of high-order harmonics using laser-produced rare-gas-like ions," Physical Review Letters, vol. 69, no. 15, pp. 2176–2179, 1992.

[129] S. Kubodera, Y. Nagata, Y. Akiyama, K. Midorikawa, M. Obara, H. Tashiro, and K. Toyoda, "High-order harmonic generation in laser-produced ions," Physical Review A, vol. 48, no. 6, pp. 4576–4582, 1993.

[130] A. Butler, D. Spence, and S. Hooker, "Guiding of high-intensity laser pulses with a hydrogen-filled capillary discharge waveguide," Physical Review Letters, vol. 89, no. 18, p. 185003, 2002.

[131] Y. Wang, B. Luther, M. Berrill, M. Marconi, F. Brizuela, J. Rocca, and V. Shlyaptsev, "Capillary discharge-driven metal vapor plasma waveguides," Physical Review E, vol. 72, no. 2, p. 026413, 2005.

[132] M. Berrill and J. J. Rocca, unpublished.

[133] M. Berrill, senior Design Thesis - Colorado State University.

[134] H. Wang, S. Backus, Z. Chang, R. Wagner, K. Kim, X. Wang, D. Umstadter, T. Lei, M. M. Murnane, and H. C. Kapteyn, "Generation of 10-W average-power, 40-TW peak-power, 24-fs pulses from a Ti:sapphire amplifier system," Journal of the Optical Society of America B, vol. 16, no. 10, pp. 1790–1794, 1999.

[135] N. Saito and I. Suzuki, "Multiple photoionization in Ne, Ar, Kr, and Xe from 44 to 1300 eV," International Journal of Mass Spectrometry and Ion Processes, vol. 115, no. 2-3, pp. 157–172, 1992.

[136] J. A. Samson, "The measurement of the photoionization cross sections of the atomic gases," in Advances in Atomic and Molecular Physics, D. Bates and I. Estermann, Eds. New York: Academic Press, 1966, vol. 2, pp. 177–261.

[137] J. J. Rocca, "Table-top soft x-ray lasers," Review of Scientific Instruments, vol. 70, no. 10, pp. 3799–3827, 1999.

[138] M. Drescher, M. Hentschel, R. Kienberger, G. Tempea, C. Spielmann, G. A. Reider, P. Corkum, and F. Krausz, "X-ray pulses approaching the attosecond frontier," Science, vol. 291, no. 5510, pp. 1923–1927, 2001.

[139] C. Tian and T. Sun, "Amplification of high-harmonic radiation by x-ray amplifiers," journal of the Optical Society of America B, vol. 13, no. 12, pp. 2852–2862, 1996.

[140] B. Luther, L. Lurfaro, A. Klix, and J. J. Rocca, "Femtosecond laser triggering of a sub-100 picosecond high-voltage spark gap," Applied Physics Letters, vol. 79, no. 20, pp. 3248–3250, 2001.

[141] B. Benware, C. Macchietto, C. Moreno, and J. J. Rocca, "Demonstration of a high average power tabletop soft x-ray laser," Physical Review Letters, vol. 81, no. 26, pp. 5804–5807, 1998.

[142] S. Heinbuch, M. Grisham, D. Martz, and J. J. Rocca, "Demonstration of a desktop size high repetition rate soft x-ray laser," Optics Express, vol. 13, no. 11, pp. 4050–4055, 2005.

Appendix A

Capillary discharge, extreme-ultraviolet amplifier

Compact capillary discharge lasers and high harmonic generation are sources of bright, soft x-ray pulses, which can be used for a variety of applications. Capillary discharge lasers [32, 33] have the advantage of producing highly energetic pulses ($\sim$1 mJ) [137], but have long pulse durations ($\sim$1 ns). In contrast to this, high harmonic generation (HHG) produces pulses with attosecond pulse durations [138] and, in addition, excellent spatial coherence [17], but low energy. The main limitation of high harmonic generation is the low conversion efficiency (10^{-6}–10^{-4}). Therefore, the use of a capillary discharge as a soft x-ray amplifier for a high harmonic generated seed will provide pulses with the benefits of both techniques: short pulse duration, high spatial coherence, and high pulse energy.

Amplification of HHG was first demonstrated by Ditmire *et al.* in 1995 [29], where a solid gallium target was irradiated by a laser to create a collisionally pumped laser plasma amplifier. An overall gain of $\sim$ 3 was observed for the 21^{st} harmonic of an Nd:glass laser. Since then, very little progress has been made in the area of soft x-ray amplifiers [30, 31, 139], despite the fact that this first observation occurred over ten years ago. In addition, all of the amplifiers that have been demonstrated to date have employed laser created amplifier media [29–31], with the latest versions using optical-field-ionization (OFI), soft x-ray lasers as the gain medium. Capillary discharges provide an attractive alternative, since the discharges are electrically driven and do not require

large amounts (∼1 J) of laser energy.

A.1 Capillary discharge soft x-ray lasers

Capillary discharges have two basic designs, slow and fast, characterized by the rise time of the excitation current pulse. Slow capillary discharges typically use an evacuated plastic capillary and have rise times greater than 50 ns. The slow current pulse ablates material off the inner wall of the capillary, forming a shock wave that compresses the ablated material, which is then collisionally excited by the current pulse.

Fast capillary discharges have rise times less than 50 ns and have been the most successful at producing soft x-ray lasers. The fast current rise time (<50 ns) has the advantage of minimizing the amount of material ablated from the capillary wall. The fast rise time ionizes the gas and creates a large magnetic field, which compresses the plasma. This compression occurs rapidly and detaches the plasma from the capillary wall before significant amounts of material have been ablated. Fast capillary discharges typically compress the plasma from the 1–4 mm capillary diameter to ∼300 μm. The large current density combined with this plasma compression results in a high density, multiply ionized plasma column with good axial uniformity, ideal conditions for soft x-ray lasing. Lasing was first observed in a fast capillary discharge in the $3p$–$3s$, $J = 0$–1 transition of neon-like argon (Ar IX) at 46.9 nm [32, 33].

A.2 Experimental setup

The setup for this experiment (Fig. A.1) consists of a two stage, Ti:sapphire amplifier, operating at 10 Hz and being pumped with a total of 200 mJ at 532 nm. After the second pass of the second stage, the pulse has ∼20 mJ of energy and it is split with a 90%/10% beam-splitter. The portion of the pulse with 90% of the energy is reflected back through the second stage of amplification for two more passes, resulting in a ∼50 mJ pulse. This pulse is then compressed (∼28 fs) and 9–12 mJ is focused

into a 400 μm diameter bore, hollow capillary filled with low pressure ($\sim$1 Torr) xenon. The interaction between the laser pulse and the xenon produces the high harmonic seed that is to be amplified. Pulse energies outside this range resulted in lower HHG signal. To ensure maximum amplification, one of the harmonic peaks must match the spectral bandwidth of the amplifier. The 17^{th} harmonic of 800 nm (47.1 nm) overlaps well with the lasing transition of Ar IX (46.9 nm). In order to maximize the spectral overlap, the oscillator spectrum was adjusted so the output of the amplifier was blue-shifted 3 nm, to 797 nm, aligning the peak of the 17th harmonic with the peak of the amplifier gain.

After the harmonics were generated, two different setups were utilized. The first setup consisted of a large vacuum chamber with two cubic zirconia (ZrO_2) windows. The intent was to use the windows, at a relatively high angle of incidence, to align the harmonic seed with the amplification medium, while rejecting a large portion of the 800 nm light. The windows were mounted on motorized optical mounts, which were controlled from outside the vacuum chamber. The ZrO_2 windows were used at an incidence angle of $\sim$80°, resulting in an overall EUV reflectivity of $\sim$25%. At 80°, the total reflectivity of the two flats at 800 nm is $\sim$17%. In the second setup, the vacuum chamber and ZrO_2 windows were simply removed, allowing the HHG seed to propagate directly into the amplifier.

After this setup, the harmonics were directed into a fast capillary discharge (Fig. A.2). The discharge consists of a spark gap (two large metal plates with a gap between them) and a alumina capillary. The metal plates and gap are sealed and pressurized with air to achieve the correct high voltage hold-off. This entire spark gap is then submerged in transformer oil which is chilled and circulated. One plate of the spark gap is attached to the pulsed, high voltage supply, while the other is attached to one end of a 9–12 cm long, 3 mm diameter alumina (Al_2O_3) capillary filled with $\sim$300 mTorr of argon. The other end of the capillary is grounded. A relatively long (a few ms), high voltage (a few kV) pulse is used to preionize the argon before a very fast ($\sim$25

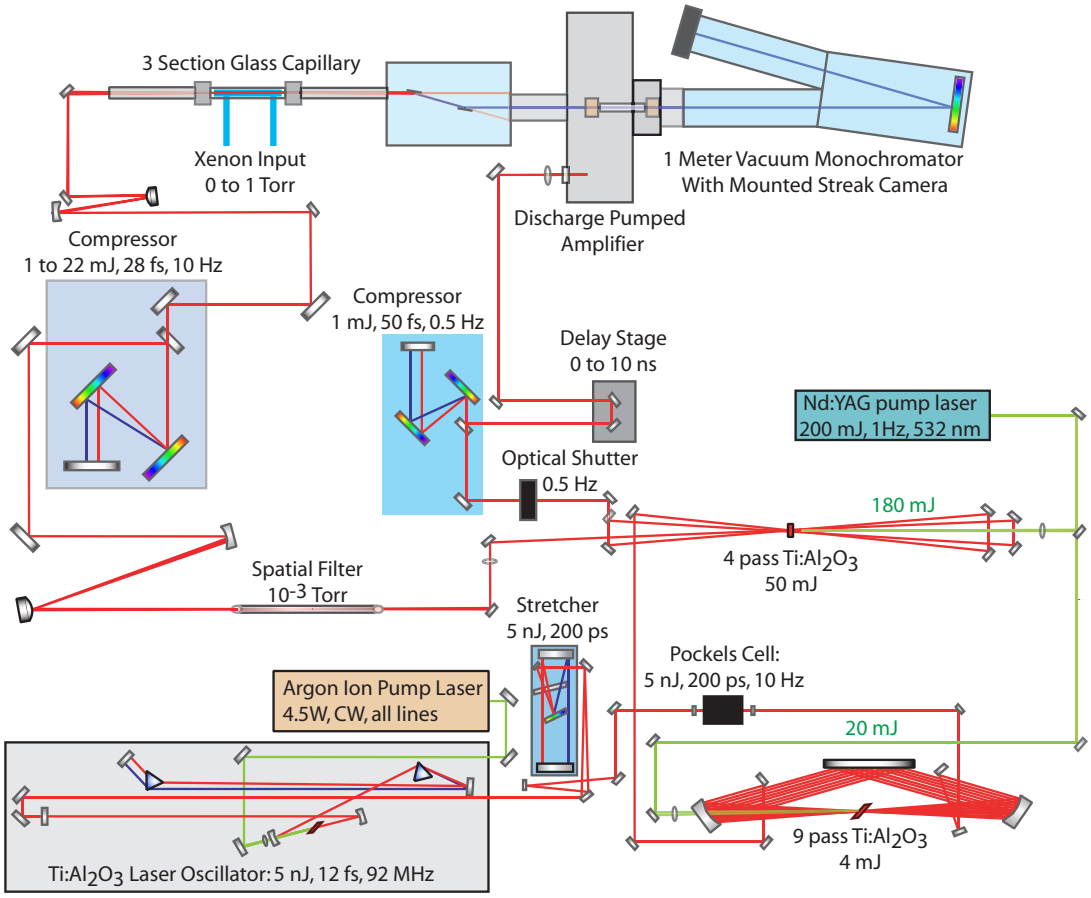

Figure A.1: Experimental setup for amplification of high harmonic generation.

ps rise time), 40–65 kV pulse is applied to initiate the gain. The high voltage pulse charges capacitors until the laser causes a breakdown of the spark gap. This results in a discharge with peak currents of 10–20 kA. The charging times limited the repetition rate of the discharge to ∼1 Hz. In order to reliably initiate the discharge, the high voltage pulse was laser triggered. The small percentage of laser light that was split in the second stage of the laser amplifier is compressed in a second compressor to below 50 fs. It is then sent to a very long optical delay stage (0–10 ns) before being focused into the spark gap of the discharge, initiating the current pulse. The gain in the amplifier lasts for a few ns [33], so accurate and repeatable triggering is necessary for a seeded amplifier experiment. Laser triggering was used to reduce the jitter in a spark gap to sub-100 picosecond levels [140].

A one meter vacuum monochromator, with 100 μm entrance and exit slits, was placed after the discharge amplifier. To determine the resolution of the monochromator, the intensity of the discharge laser line was measured as a function of the monochromator setting since the linewidth of the lasing transition is $\sim$ 50 mÅ [141]. Figure A.3 shows that the monochromator has a full-width-half-maximum resolution of 2 Å.

Attached to the end of the monochromator was a homebuilt streak camera. A streak camera is an accurate way to measure picosecond duration EUV pulses. The operation of a streak camera is shown schematically in Figure A.4. At the entrance of the streak camera is a 100 μm slit, which acts as the exit slit of the monochromator. The EUV pulses pass through the slit and strike a microchannel plate (MCP). The MCP converts the EUV pulse to an electron bunch at the same time it amplifies the signal (Fig. A.4(a)). This electron bunch is accelerated by a biased wire grid and traverse a set of focusing electrodes which ensure that the bunch does not expand in the direction transverse to the motion. The electrons then traverse a set of sweep plates (Fig. A.4(b)). This is a set of parallel plates, one of which is grounded and the other has a very fast high voltage edge applied. This fast edge causes a time varying electric field between

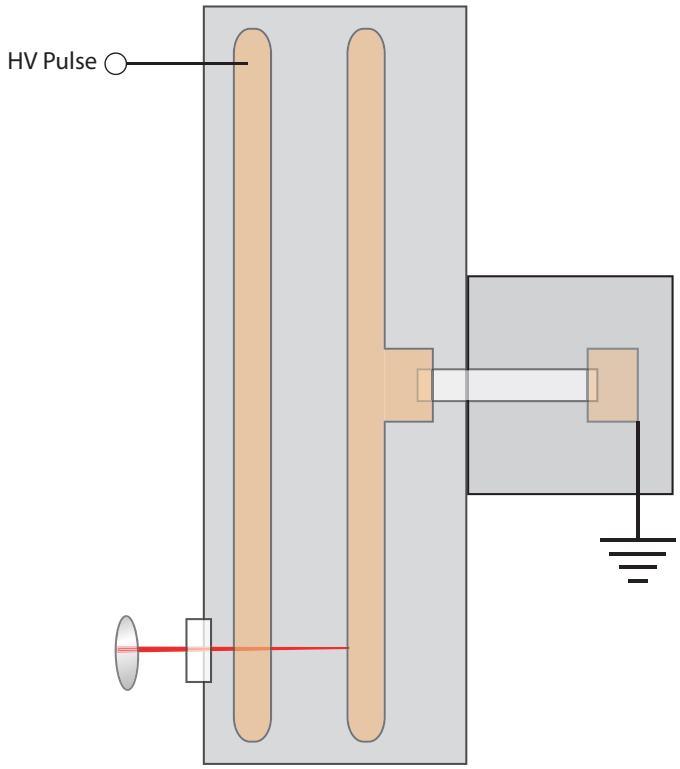

Figure A.2: Laser triggered capillary discharge schematic (top view).

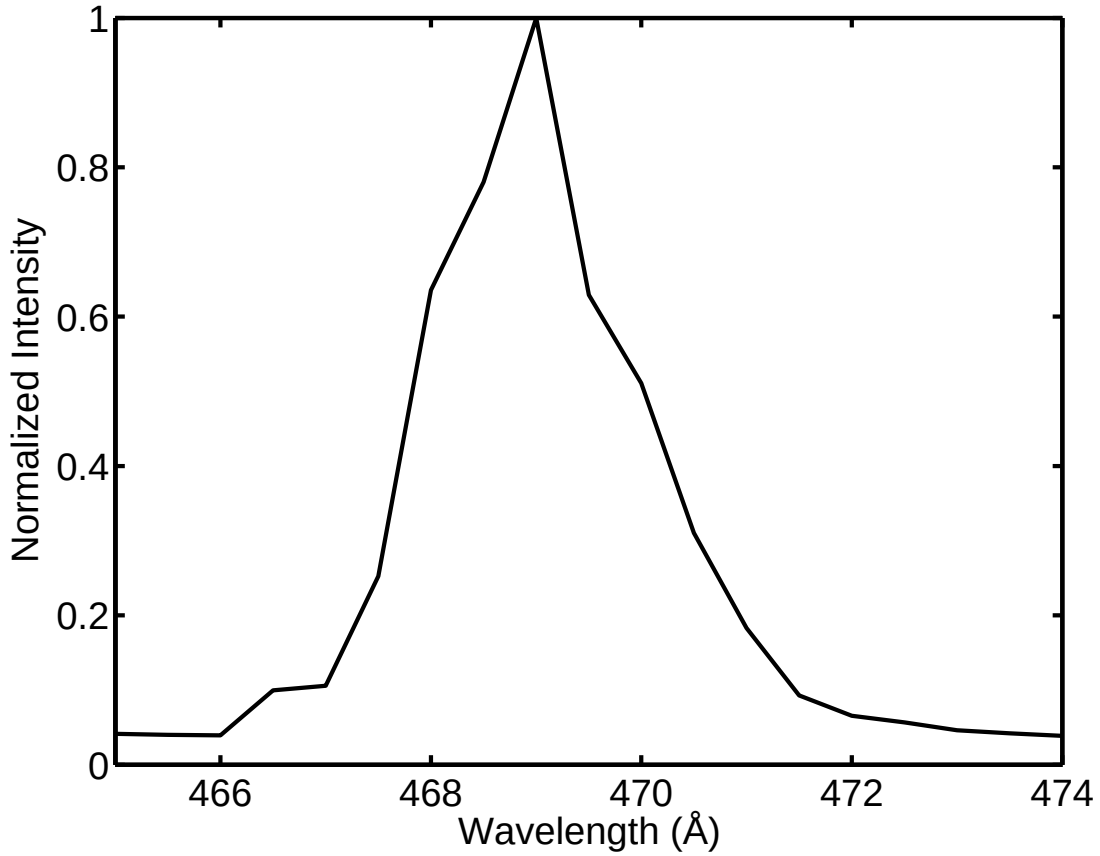

Figure A.3: Measurement of the monochromator resolution, using the discharge lasing line as a delta function source.

the plates, and, consequently, a time varying deflection of the electrons. The sweep plates map temporal structure to spatial structure. The swept electrons then strike a micro-channel plate and a phosphor screen (Fig. A.4(c)). The signal is measured with a phosphor screen imaged onto a visible CCD camera. Based on the sweep voltage and the sweep camera dimensions, the streak camera has a calibration of 4 ps per CCD pixel. The electron bunch that is ejected from the front MCP will exhibit some temporal smearing due to the operation of the MCP. This, combined with space-charge effects within the streak camera, will limit the resolution. Since the HHG emission is effectively a temporal delta function, it can be used to determine the temporal response of the streak camera. Figures A.6(b) and A.7(b) show that the sweep traces of the high harmonic radiation have a FWHM of ∼50 pixels, which gives a streak camera resolution of 200 ps.

A.3 Results

Figure A.5 shows a simultaneous measurement of the discharge current and the emission from the argon plasma. The discharge current was measured with a Rogowski coil designed to convert current to voltage with a 10^{-4} conversion (10 kA $\rightarrow$ 1 V). The plasma emission was measured with a solid aluminum, uncalibrated photocathode, biased with 1600 V. This photocathode was constructed at Colorado State University and the conversion efficiency was estimated to be within a factor of two of similarly constructed photocathodes, with a conversion of 90 kV/J. Using this estimated calibration, the pulse energy of the discharge laser is ∼5 μJ (Fig. A.5), with most of the noise due to interference from the capillary discharge and the incoherent plasma emission. This pulse energy is in agreement with the pulse energy of ∼7.5μJ, obtained by scaling the results of a similar capillary discharge [142] to account for the difference in capillary length. Some of the dynamics of the plasma can be seen in the measured current pulse. The current rises rapidly in the pre-ionized argon. The large current produces a large

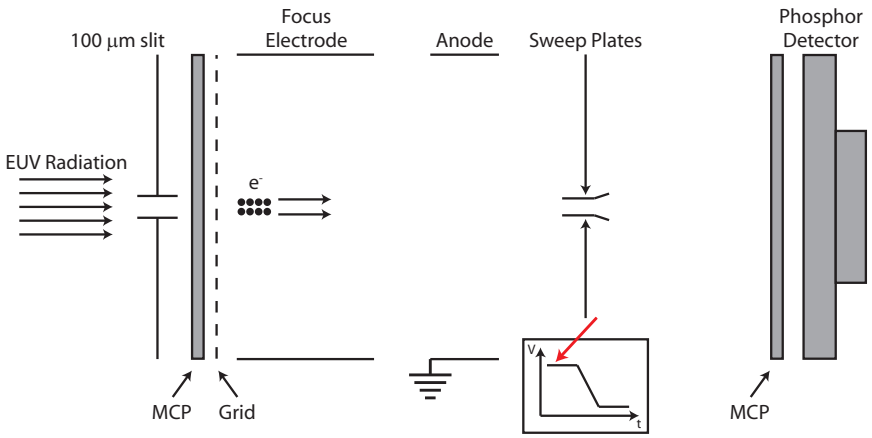

(a)

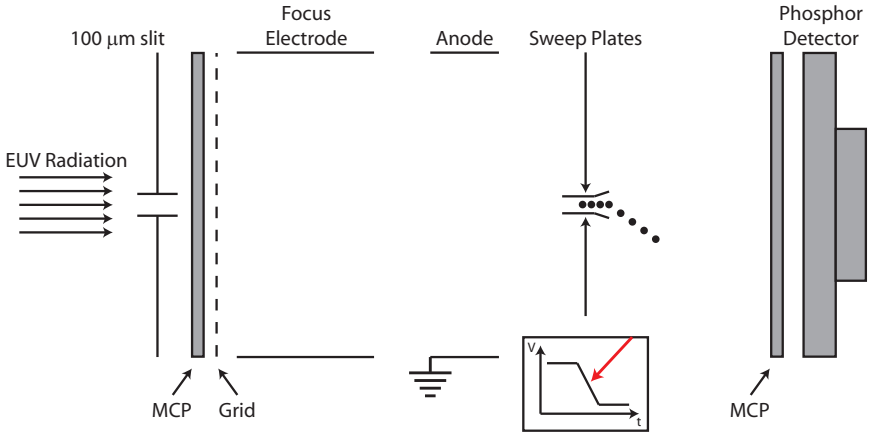

(b)

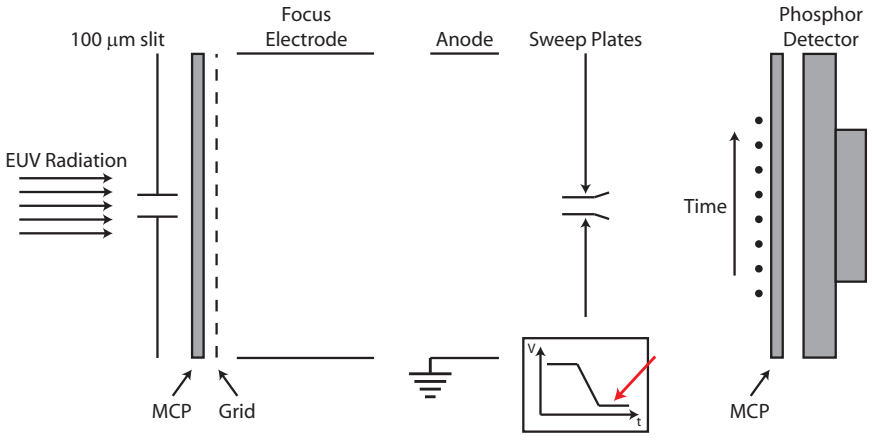

(c)

Figure A.4: Schematic diagram of the EUV streak camera. The red arrow refers to the voltage on the sweep plates.

magnetic field, which compresses the plasma. As the plasma compresses, the inductance of the plasma increases. As the plasma radius nears its minimum, the inductance increases enough to cause the current to level off or decrease. This is when the plasma conditions are ideal for lasing. After the compression, the plasma expands again and the current increases again due to the drop in inductance. The characteristic dip in current is clearly visible in Figure A.5 and it corresponds well with the laser emission, which has a temporal FWHM of $\sim$1.5 ns.

After the discharge was characterized, streak measurements were taken with two different discharge capillary lengths. The monochromator was set to the peak of the amplifier gain and streak images were taken of only the discharge emission, only the HHG emission, and the amplified HHG emission. First, a 12 cm capillary was used in the discharge, providing a strong lasing line. Figure A.6 shows the sweep traces for this capillary length. The discharge and harmonic signals were very jittery with respect to the sweep voltage, both being approximately 500 ps. With laser triggering of the discharge, the jitter between the harmonics and the discharge was also approximately 500 ps. The combined jitter resulted in only a few of the the swept pulse traces being completely contained within the CCD image. There was also a slight pointing instability of the harmonic radiation. The extent of this pointing instability is indicated by the horizontal white lines (Figs. A.6 and A.7). All of the harmonic sweep traces lay between these two lines, so the sweep signals were integrated between these lines for analysis. As can be seen from Figure A.6, there is virtually no difference between the seeded and unseeded discharge sweep traces. All of the data taken with a 12 cm capillary shows this behavior.

In order to increase the signal to noise ratio, the 12 cm capillary was replaced with a 9 cm capillary, resulting in less amplifier gain. The lower gain will reduce the amplified HHG signal, but also the strength of the lasing line, reducing the background signal. Figure A.7 shows the sweep traces for a 9 cm capillary. With the 9 cm capillary, the

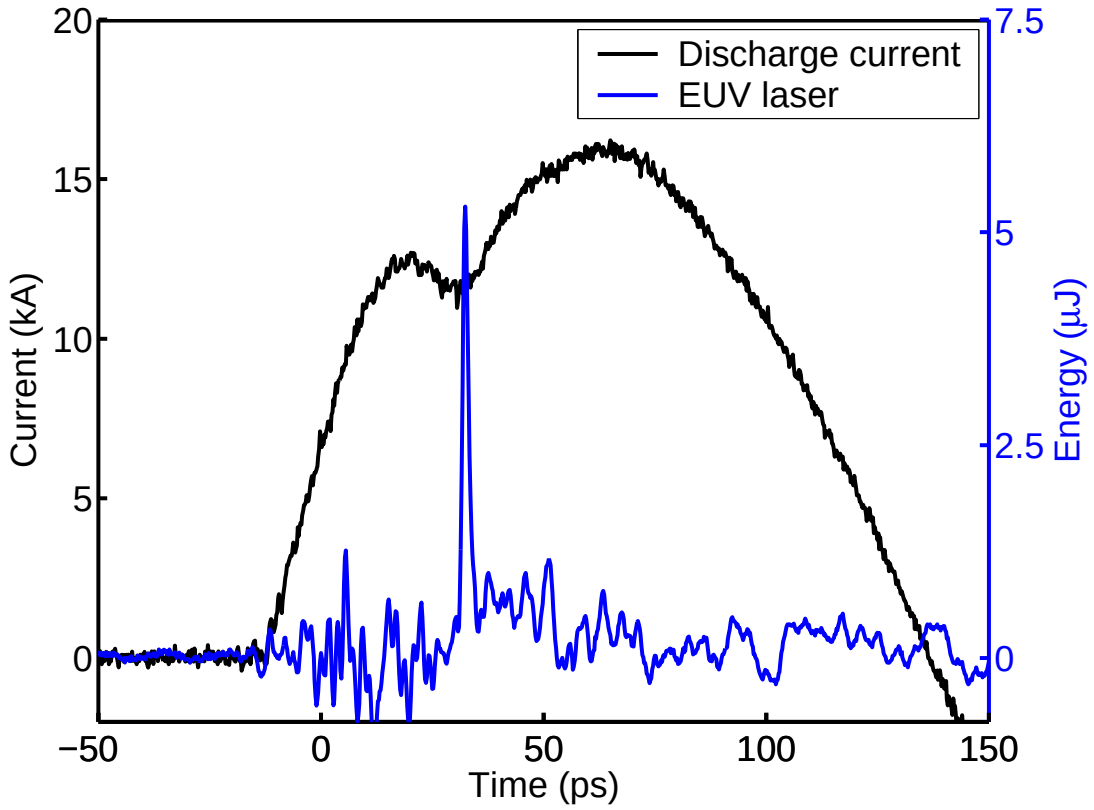

Figure A.5: Measurement of the 12 cm capillary discharge current (black) and 46.9 nm laser energy (blue).

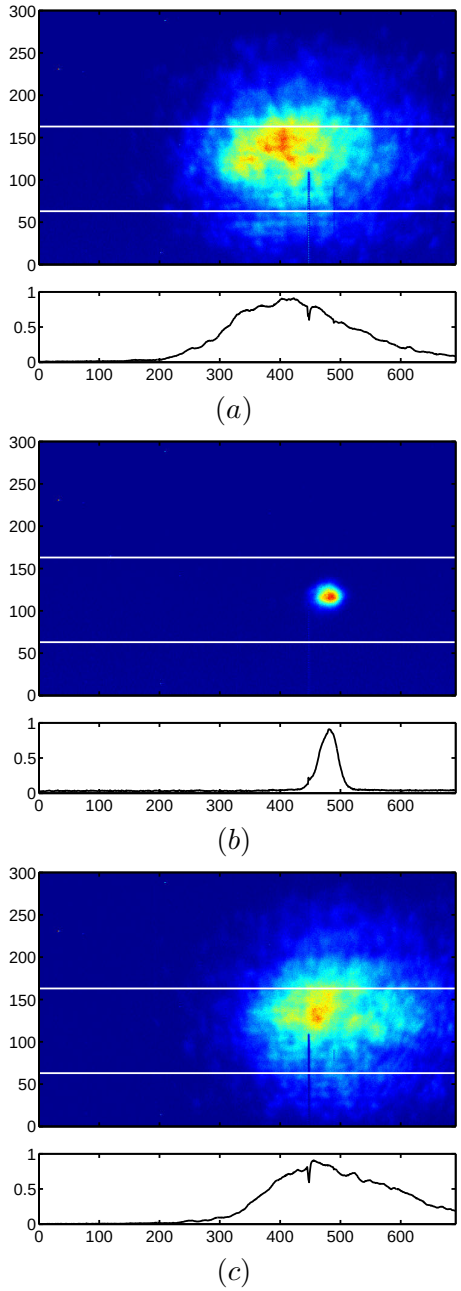

Figure A.6: 12 cm long capillary discharge sweep camera traces of (a) the discharge lasing line, (b) the high harmonic emission, and (c) the seeded amplifier. The signal between the white lines is integrated and plotted below the streak.

harmonics exhibited the same pointing instability, so the sweep traces were integrated in the same manner as the 12 cm sweep traces. Due to the lower gain, the discharge laser is not saturated and exhibits more temporal structure (Fig. A.7(a)). Figure A.7 shows an abnormal peak on the discharge background, possibly indicating amplification. Unfortunately, this signal strength equates to a simple addition of the discharge and harmonic signals. As with the 12 cm capillary, the 9 cm capillary does not exhibit strong evidence of amplification.

A.4 Discussion and conclusion

This experiment was very difficult to construct and execute. First, there were difficulties in obtaining enough HHG signal around 46.9 nm (the peak of the gain in the discharge amplifier) to seed the amplifier. For the experimental parameters used (400 μm, 12 mJ, 28 fs), the 17^{th} harmonic (47.1 nm) had significantly less signal than the 15^{th} harmonic. The measurements were made near the cutoff wavelength of the monochromator grating, so the difference in signal level can be attributed to the grating efficiency. But, a slightly smaller capillary could have provided more intensity which can result in more efficient generation the 17^{th}, resulting in more seed energy for the amplifier. Secondly, a significant amount of energy was expended attempting to align the HHG signal with the gain region. Construction of the discharge did not guarantee that the entrance and exit holes were aligned with the gain medium, so external pinholes were used to determine the axis of maximum gain. Even so, aligning the HHG signal along these pinholes did not result in successful amplification. Lastly, the timing jitter of the laser triggered discharge was an issue. Since the laser was focused onto one of the electrodes, the timing jitter would degrade over time as the laser ablated the electrode material. A temporary solution of replacing the ablated portion of the brass electrode with a stainless steel screw reduced this problem but did not eliminate it. This solution also required the frequent disassembly of the discharge spark gap to replace this screw.

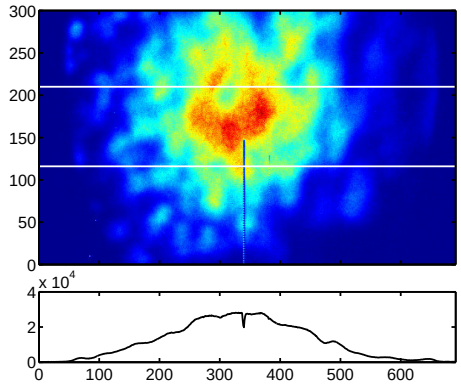

(a)

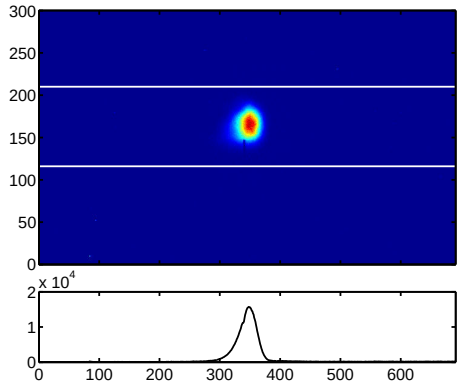

(b)

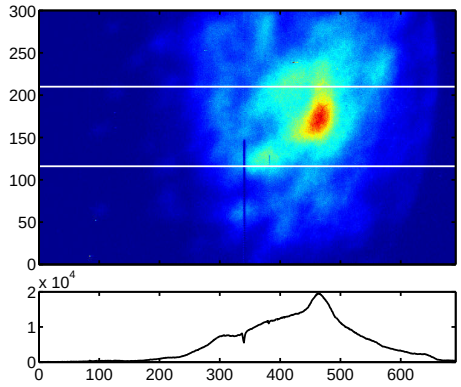

(c)

Figure A.7: 9 cm long capillary discharge sweep camera traces of (a) the discharge lasing line, (b) the high harmonic emission, and (c) the seeded amplifier. The signal between the white lines is integrated and plotted below the streak.

A different laser triggering scheme may improve the jitter while being a more permanent solution to the ablation problem.

When this experiment is compared with published amplification experiments [29, 30], many of the parameters are found to be similar: same spectral mismatch (harmonics ∼200 times larger than the amplifier gain bandwidth), similar seed energy, similar gain-length product (∼5), similar plasma density and similar spatial overlap. The main difference lies in the aspect ratio (length/diameter) of the gain media. The published experiments used gain media with an aspect ratio of 10–25, while the capillary discharge has an aspect ratio of 300–400. Therefore, the capillary discharge amplifier is much more sensitive to the pointing of the harmonic seed than the previous experiments and the negative results of this experiment can be attributed to this pointing sensitivity.

Due to the large similarities between this experiment and published experiments, soft x-ray amplification in a capillary discharge is believed to be feasible and more experiments are needed to confirm or refute this belief. All of the problems mentioned above can be overcome with a little experimenting and engineering. Therefore, it should be possible to amplify high harmonic radiation in a capillary discharge.

Appendix B

ADK rates for arbitrary atomic states

The ADK tunnel ionization rate equation (Eq. 4.4) is only valid for ionization from a ground state with zero orbital angular momentum ($l = 0$). This is valid for hydrogen and helium, but the larger noble gas atoms (neon, argon, krypton, and xenon) have an outer electron shell that consists of six p ($l = 1$) electrons. Therefore, tunnel ionization occurs from a ground state that has a non-zero orbital angular momentum for these atoms and their low ionization states. The full ADK ionization rate, without the assumption of $l = 0$, is [99, 107]:

$$\omega(t) = \omega_p |C_{n^*}|^2 G_{lm} \left(\frac{4\omega_p}{\omega_t}\right)^{2n^* - |m| - 1} \exp\left(-\frac{4\omega_p}{3\omega_t}\right) \tag{B.1}$$

with

$$\begin{aligned}
\omega_p &= \frac{I_p}{\hbar} \\
\omega_t &= \frac{eE_l(t)}{(2mI_p)^{1/2}} \\
n^* &= Z\left(\frac{I_{ph}}{I_p}\right)^{1/2} \\
G_{lm} &= \frac{(2l+1)(l+|m|)!}{2^{|m|}(|m|)!(l-|m|)!} \\
|C_{n^*}|^2 &= 2^{2n^*}[n^*\Gamma(n^*+l^*+1)\Gamma(n^*-l^*)]^{-1}.
\end{aligned}$$

where $l^* = 0$ for $l << n$ and $l^* = n^* - 1$ otherwise, l and m are the orbital quantum

number and its projection, respectively, and the other variables are defined in Eq. 4.4. Figures B.1 and B.2 shows the results of sample calculations with $l = m = 1$ and $l = 1, m = 0$, respectively. The parameters are the same as those used Figure 4.2 (reproduced below). Since $n = 3$ and $l = 1$ for the ground state of argon, the condition $l << n$ is not fulfilled and the full expression for l^* is used. Due to the fact that Figures B.1 and B.2 are different, it can be concluded that the effect of $|m|$ in $\left(\frac{4\omega_p}{\omega_t}\right)^{2n^*-|m|-1}$ is significant since $G_{11} = G_{10}$. It is clear from the figures that ionizing from an $l = 1, m = 0$ state yields larger ADK rates earlier in the pulse, resulting in full ionization at lower cutoff energies.

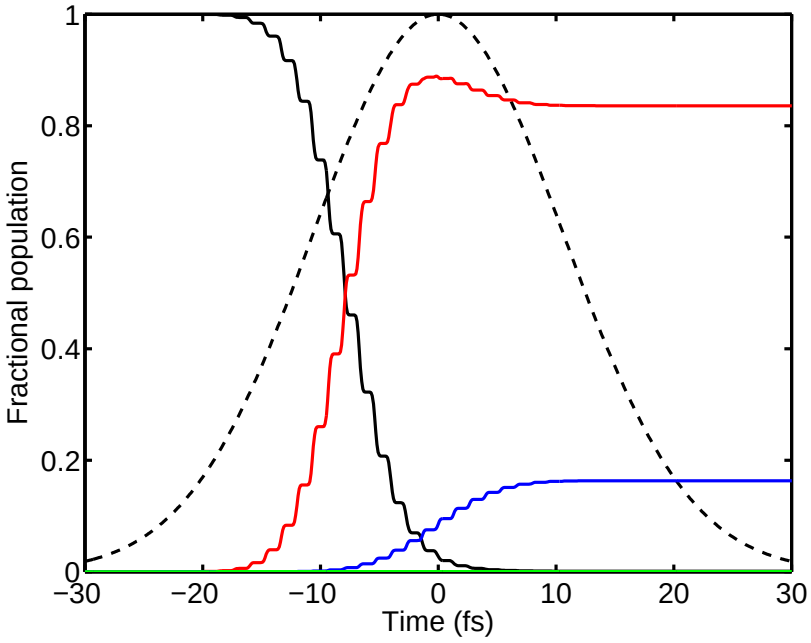

(a)

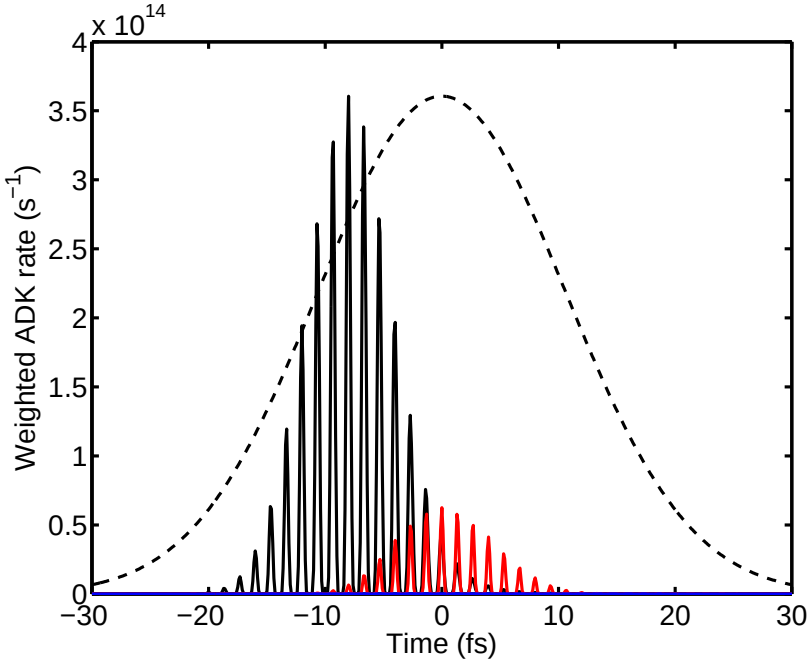

(b)

Figure B.1: (a) Fractional populations, for $l = m = 1$, of neutral Ar (black), Ar^+ (red), Ar^{2+} (blue), and Ar^{3+} (green). (b) ADK ionization rates for neutral Ar (black), Ar^+ (red), and Ar^{2+} (blue), weighted by their respective fractional populations. The temporal pulse envelope (black dotted) is shown for reference. These calculations correspond to a peak laser intensity of 10^{15} W/cm^2, a full-width half-maximum (FWHM) pulse duration of 25 fs, and a central laser wavelength of 800 nm.

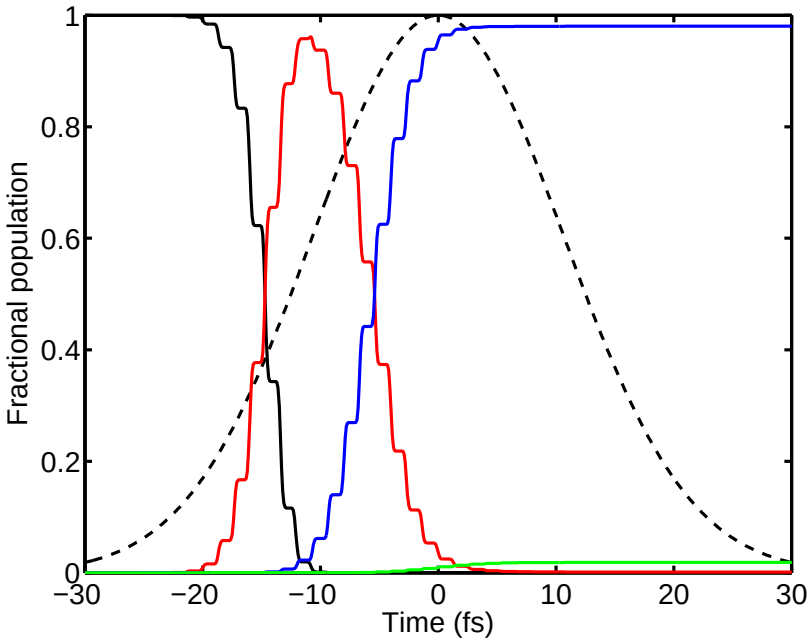

(a)

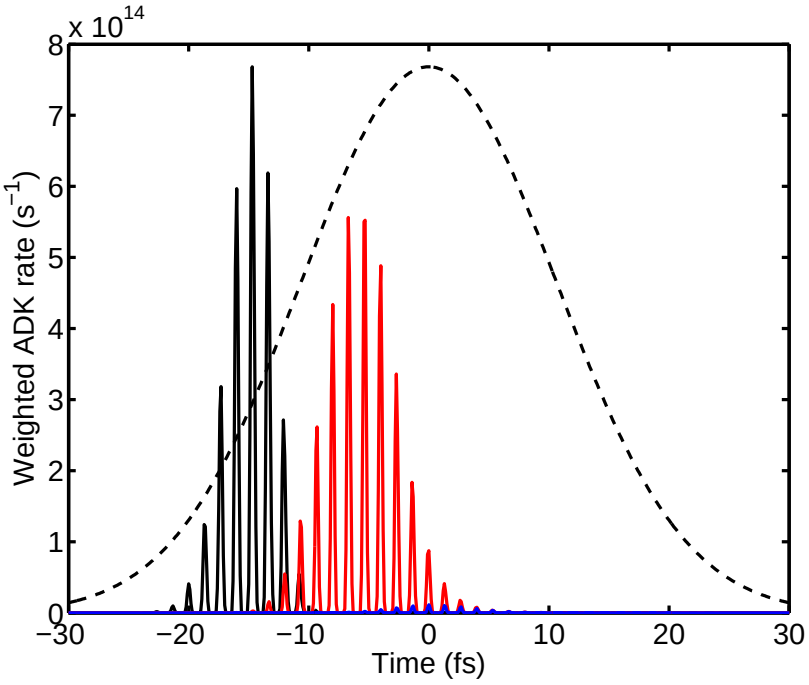

(b)

Figure B.2: (a) Fractional populations, for $l = 1, m = 0$, of neutral Ar (black), Ar^+ (red), Ar^{2+} (blue), and Ar^{3+} (green). (b) ADK ionization rates for neutral Ar (black), Ar^+ (red), and Ar^{2+} (blue), weighted by their respective fractional populations. The temporal pulse envelope (black dotted) is shown for reference. These calculations correspond to a peak laser intensity of 10^{15} W/cm^2, a full-width half-maximum (FWHM) pulse duration of 25 fs, and a central laser wavelength of 800 nm.

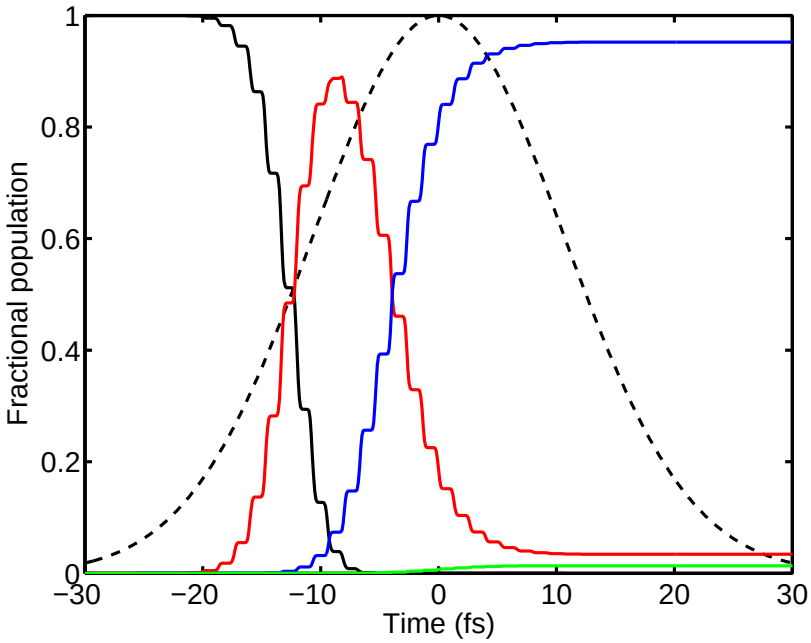

(a)

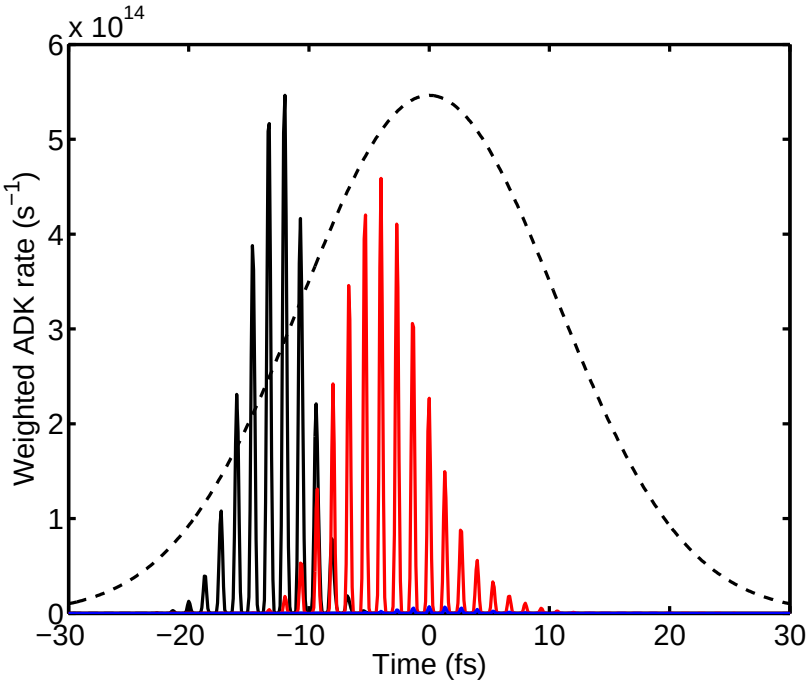

(b)

Figure B.3: (a) Fractional populations, for $l = m = 0$, of neutral Ar (black), Ar^+ (red), Ar^{2+} (blue), and Ar^{3+} (green). (b) ADK ionization rates for neutral Ar (black), Ar^+ (red), and Ar^{2+} (blue), weighted by their respective fractional populations. The temporal pulse envelope (black dotted) is shown for reference. These calculations correspond to a peak laser intensity of 10^{15} W/cm^2, a full-width half-maximum (FWHM) pulse duration of 25 fs, and a central laser wavelength of 800 nm.

Appendix C

Matched radius and plasma waveguide propagation vector derivation

When analyzing the guiding of a Gaussian laser pulse through a plasma waveguide, a parabolic electron density is assumed (Eq. 4.47):

$$N_e(r) = N_0 + \Delta N \left(\frac{r}{r_0}\right)^2 \tag{C.1}$$

where N_0 is the electron density on axis, ΔN is the change in density from the center to the edge of the waveguide, r is the radial position, and r_0 is the radial extent of the waveguide. Assuming the index of refraction is dominated by this plasma, the radially varying index is given by Eq. 4.34

$$\begin{aligned} n_p^2(r) &= 1 - \frac{N_e(r)e^2}{\epsilon_0 m_e \omega^2} && \text{(C.2)} \\ n_p^2(r) &= 1 - \frac{N_0 e^2}{\epsilon_0 m_e \omega^2} - \frac{\Delta N r^2 e^2}{\epsilon_0 m_e \omega^2 r_0^2} && \text{(C.3)} \\ &= n_0^2 - \frac{\Delta N r^2 e^2}{\epsilon_0 m_e \omega^2 r_0^2} && \text{(C.4)} \\ & && \text{(C.5)} \end{aligned}$$

where the index is now a function of radius and not time and n_0 is the index at the center of the plasma. To determine the matched radius (i.e. the radius of a Gaussian beam that does not change during propagation) and propagation vector (k-vector) of a Gaussian beam of frequency ω propagating in a parabolic, plasma waveguide, it is necessary to begin with the time-independent wave equation

$$\nabla^2 E(\mathbf{r}) + \frac{n^2\omega^2}{c^2} E(\mathbf{r}) \quad = \quad 0 \tag{C.6}$$

where E is the electric field, n is the index of refraction, and c is the speed of light in a vacuum. Since the beam is guided, the beam profile does not change in the direction of propagation (in this case, z). Therefore, it is assumed that only the phase can vary in the direction of propagation

$$E(\mathbf{r}) = E(r,\theta)e^{i\beta z} \tag{C.7}$$

where β is propagation vector. Substituting this into Eq. C.6 results in

$$\nabla_\perp^2 E(r,\theta) - \beta^2 E(r,\theta) + \frac{n^2\omega^2}{c^2} E(r,\theta) = 0 \tag{C.8}$$

where $\nabla_\perp^2$ is the transverse divergence. Combining this with the radially varying index of refraction (Eq. C.4) yields

$$\nabla_\perp^2 E(r,\theta) - \beta^2 E(r,\theta) + \left(n_0^2 - \frac{\Delta N r^2 e^2}{\epsilon_0 m_e \omega^2 r_0^2}\right)\frac{\omega^2}{c^2} E(r,\theta) = 0 \tag{C.9}$$

Since the beam is assumed to be Gaussian, the electric field is given by

$$E(r,\theta) = e^{-\left(\frac{r}{w_0}\right)^2} \tag{C.10}$$

where w_0 is the waist size of the Gaussian beam. Substituting this into Eq. C.9 and using the radial form of the transverse divergence ($\nabla_\perp^2 = \frac{1}{r}\frac{\partial}{\partial r} r \frac{\partial}{\partial r} + \frac{1}{r^2}\frac{\partial^2}{\partial\theta^2}$) yields

$$\frac{1}{r}\frac{\partial}{\partial r} r \frac{\partial}{\partial r} e^{-\left(\frac{r}{w_0}\right)^2} + \left(\left(n_0^2 - \frac{\Delta N r^2 e^2}{\epsilon_0 m_e \omega^2 r_0^2}\right)\frac{\omega^2}{c^2} - \beta^2\right) e^{-\left(\frac{r}{w_0}\right)^2} \quad = \quad 0 \tag{C.11}$$

$$\left(\frac{4r^2}{w_0^4} - \frac{4}{w_0^2}\right) e^{-\left(\frac{r}{w_0}\right)^2} + \left(\left(n_0^2 - \frac{\Delta N r^2 e^2}{\epsilon_0 m_e \omega^2 r_0^2}\right)\frac{\omega^2}{c^2} - \beta^2\right) e^{-\left(\frac{r}{w_0}\right)^2} \quad = \quad 0 \tag{C.12}$$

$$\left(\frac{4r^2}{w_0^4} - \frac{4}{w_0^2}\right) + \left(\left(n_0^2 - \frac{\Delta N r^2 e^2}{\epsilon_0 m_e \omega^2 r_0^2}\right)\frac{\omega^2}{c^2} - \beta^2\right) \quad = \quad 0 \tag{C.13}$$

Equating the coefficients of the r^2 term to zero yields an expression for the matched radius

$$\begin{aligned}
\frac{4}{w_0^4} - \frac{4\pi r_e \Delta N}{r_0^2} &= 0 && \text{(C.14)}\\
\frac{4}{w_0^4} &= \frac{4\pi r_e \Delta N}{r_0^2} && \text{(C.15)}\\
w_0 &= \left[\frac{r_0^2}{\pi r_e \Delta N}\right]^{1/4} && \text{(C.16)}\\
& && \text{(C.17)}
\end{aligned}$$

where $r_e = \frac{e^2}{4\pi\epsilon_0 m_e c^2}$ is the classical electron radius. Equating the constant terms yields the propagation vector

$$\begin{aligned}
-\frac{4}{w_0^2} + \frac{n_0^2\omega^2}{c^2} - \beta^2 &= 0 && \text{(C.18)}\\
\beta^2 &= \frac{n_0^2\omega^2}{c^2} - \frac{4}{w_0^2} && \text{(C.19)}\\
\beta^2 &= \frac{\omega^2}{c^2}\left(1 - \frac{N_0 e^2}{\epsilon_0 m_e \omega^2}\right) - \frac{4}{w_0^2} && \text{(C.20)}\\
\beta^2 &= \frac{\omega^2}{c^2}\left(1 - \frac{N_0 e^2}{\epsilon_0 m_e \omega^2} - \frac{4c^2}{\omega^2 w_0^2}\right) && \text{(C.21)}\\
\beta &= \frac{\omega}{c}\sqrt{1 - \frac{N_0 e^2}{\epsilon_0 m_e \omega^2} - \frac{4c^2}{\omega^2 w_0^2}} && \text{(C.22)}\\
\beta &\approx \frac{\omega}{c}\left(1 - \frac{N_0 e^2}{2\epsilon_0 m_e \omega^2} - \frac{2c^2}{\omega^2 w_0^2}\right) && \text{(C.23)}\\
\beta &\approx k\left(1 - \frac{N_0}{2N_{cr}} - \frac{2}{w_0^2 k^2}\right) && \text{(C.24)}\\
& && \text{(C.25)}
\end{aligned}$$

where $k = \frac{\omega}{c}$ is the vacuum wavevector and $N_{cr} = \frac{\epsilon_0 m_e \omega^2}{e^2}$ is the critical density.

Appendix D

Matlab codes

D.1 Amplifier simulation

The amplifier simulation consists of two matlab files: one which contains the actual simulation for one lower state lifetime ($t1$)/degeneracy ratio (g) pair and another file which loops through different values of g. After running the simulation for many different values of $t1$ and g, it was determined that a $t1 * g$ product of 25 gave the best fit to the data. Therefore this code assumes this product, loops through different values of g and calculates the corresponding $t1$ value.

The code which loops through different values and saves the results to data files:

```
% For loop to run Amplifier Simulation for multiple values
% of t1 (lower state lifetime), g (degeneracy ratio)
% and GVD (determines stretched pulse length). This program
% assumes a t1*g product of 25.

% Clear all variables and close all plots
clear all;
close all;

% Time code execution
tic
```

```
% Set values of t1 and GVD
%t1 = [0.1,0.25,0.5,0.75,1,2.5,5,7.5,10,25,50,75,100];
GVD = -3.7e-2*[1,2,3,4,5,6];
g   = [100,50,25,10,5,2.5,1,0.5,0.25,0.1];

% Filename to save values to
filename   = 'New_Eout_constant_gt_g_';

%t1max = length(t1);
GVDmax = length(GVD);
gmax   = length(g);
output = zeros(GVDmax,4);

% Loop through different values of t1 and GVD
for k=1:gmax
    newfile = [filename, num2str(g(k)),'.dat'];
    %for i=1:t1max
        for j=1:GVDmax
            output(j,1) = 25/g(k);
            output(j,2) = g(k);
            temp = AmpSim_v4_GVD_func(25/g(k),GVD(j),g(k));
            output(j,3) = temp(1);
            output(j,4) = temp(2);
            save(newfile,'output','-ascii','-double','-tabs');
        end
        %end
end

% End code timing
toc
```

The actual simulation function code:

```
% Amplifier simulation
% (based on Frantz and Nodvick, J. App. Phys. 34 2346 (1963) and Lowdermilk
% and Murray, J. App. Phys. 51 2436 (1980)
% Written by: David M. Gaudiosi
% Date: 4-5-2006
% Last Modified: 7-20-2006

function output = AmpSim_v4_GVD_func(t1,GVD,g)
% Define constants
sapphindex=1.77;              % index of sapphire
c       = 3.0E-2/sapphindex; % Speed of light in cm/ps in sapphire
%t1      = 1;                 % Lifetime of lower lasing state of Ti:Al2O3 (ps)
hveV    = 1.55;              % Energy of 800 nm photon (eV)
hv      = hveV*1.6E-19;      % Energy of 800 nm photon (J)
%g       = 1;                 % Ratio of degeneracies (g2/g1) of the energy levels
                             % Calculated from the ratio of the
                             % absorption cross-section to the
                             % stimulated emission cross-section
                             % Verdeyen pg 353
sigma   = 3.0E-19;           % Stimulated Emission cross-section of Ti:Al2O3 for
                             % 800 nm and pi-polarization (cm^2)
                             % from Verdeyen pg 393
r       = 100E-4;            % radius of spot in crystal (cm)
tauTL   = 0.020;             % FWHM of transform limited pulse (ps)
%GVD     = -3.7e-2;          % amount of GVD stretched pulse starts with (ps^2)
                             % -3.7e-2 gives approximately 5 ps
tau     = tauTL...           % Approximate stretched pulse length (ps)
          *sqrt(1+(4*log(2)*GVD/tauTL^2)^2);
tsize   = 4;                 % size of time window (# of FWHMs)
                             % i.e if tau =5 and tsize=10 than total
                             % time window is 50 ps
```

```
tsteps = 2^14;                  % # of points in time array
dt     = tau*tsize/(tsteps-1); % time step (ps)
                                % for 2^14 tsteps and tsize=4, dt is below
                                % 0.01 ps for tau from 5 to 40 ps
                                % so it will give accurate results for t1 > 0.1 ps
dw     = 2*pi/(tau*tsize);      % spectral step size (1/ps)
wmax   = 2*pi*(tsteps)...       % spectal window size (1/ps)
         /(tau*tsize);
L      = 0.6;                   % Length of Ti:Al2O3 (cm)
zsteps = 500;                   % # of points in z array
passes = 9;                     % # of passes through gain medium
mask   = 0.9;                   % Assume that the mask passes 90% of the energy

N0     = zeros(passes,1);
N0(1)  = log(3.5)/(sigma*L); % Ti ion density needed to give a signal pass gain of
N0(2)  = log(4.5)/(sigma*L); % 3.5 (approximately what I measured) on the
N0(3)  = log(5.5)/(sigma*L); % first pass, 8 on the fifth through last pass
N0(4)  = log(6.5)/(sigma*L); % and an aproximate linear fit in between
N0(5:passes) = log(8)/(sigma*L);

% Initial photon number density calculated for 1 nJ incident energy in a
% 100 um 1/e^2 gaussian spot and a gaussian temporal profile with a FWHM of tau
n0     = (1E-9*4*sqrt(log(2)))/(hv*pi*(r)^2*sqrt(pi)*c*tau);

% Define and initialize arrays
time   = [-tsize*tau/2:dt:tsize*tau/2]';        % time array
ttemp  = [-tsize*tau/2+dt/2:dt:tsize*tau/2+dt/2]'; % time array with half time steps
w      = ifftshift([-wmax/2:dw:wmax/2-dw]'); % Frequency array (1/ps) with zero
                                             % as the 1st element
dz     = L/zsteps;                           % z step size
n      = zeros(tsteps,passes+1);             % initialize photon density array
En     = zeros(passes+1,1);                  % initialize pulse energy array
```

```
% Assume that initial fractional level populations are independent of z
N1      = zeros(tsteps,1); % Lower level fractional population is 0
                           % when the seed enters medium
N2      = ones(tsteps,1); % Upper level fractional population is 1
                          % when the seed enters medium

% Set initial photon density array with correct GVD
n(:,1)  = exp(-4*log(2)*(time/tauTL).^2); % initialize photon density
                                          % as a gaussian in time at z=0
n_field = ifft(fft(sqrt(n(:,1))).*exp(i*GVD/2*w.^2));
n(:,1)  = abs(n_field).^2;
theta   = unwrap(angle(n_field));
n(:,1)  = n0*n(:,1)/max(n(:,1));          % Normalize n(z,t) and set
                                          % the correct peak value

taufwhm = fwhm(time,n(:,1));              % Calculate the FWHM of the stretched pulse

En(1)   = hv*pi*(r^2)/2*trapz(n(:,1))*c*dt; % initial pulse energy
ntemp   = zeros(2*tsteps-1,1);            % temporary array to hold half-step values
                                          % of n(z,t) for RK4

% This code uses fractional level populations. Will use actual number density
% in calculating the change in the photon density

% GVD calculations
FSGVDcm = 440e-6; % Fused Silica GVD per length (ps^2/cm).
                  % ~440 fs^2 per cm at 56 degrees (Brewster's angle)
SAGVDcm = 666e-6; % Sapphire GVD per length (ps^2/cm).
                  % ~666 fs^2 per cm at 60 degrees (Brewster's angle)
FSphase = exp(i*FSGVDcm/2*(0.2)*w.^2); % phase accumulation due to GVD of
                                       % 2 mm thick fused silica window at 56 degrees
SAphase = exp(i*SAGVDcm/2*dz*w.^2); % phase accumulation due to GVD of
                                    % dz thick sapphire at 60 degrees
```

```
% Loop through all passes through crystal
for m=1:passes
    % Actual numerical integration
    % Propagate through fused silica window at entrance of chamber
    n_field = ifft(fft(sqrt(n(:,m)).*exp(i*theta)).*FSphase);
    n(:,m) = abs(n_field).^2;
    theta  = unwrap(angle(n_field));

    % Loop through zsteps
    for u=1:zsteps
        % Re-initialize first element of population arrays
        N1(1) = 0;
        N2(1) = 1;

        % 4th Order Runge-Kutta (RK4) numerical integration routine for time
        % Interpolate values for n(z,t) at dt/2
        ntemp = interp1(time,n(:,m),ttemp);

        % k variables are for N1 and j are for N2
        for q=1:(tsteps-1)
            k1 = sigma*c*n(q,m)*(N2(q)-g*N1(q))-N1(q)/t1;
            j1 = -sigma*c*n(q,m)*(N2(q)-g*N1(q));
            k2 = sigma*c*ntemp(q)*(N2(q)+(dt/2)*j1-g*(N1(q)+(dt/2)*k1))-N1(q)/t1;
            j2 = -sigma*c*ntemp(q)*(N2(q)+(dt/2)*j1-g*(N1(q)+(dt/2)*k1));
            k3 = sigma*c*ntemp(q)*(N2(q)+(dt/2)*j2-g*(N1(q)+(dt/2)*k2))-N1(q)/t1;
            j3 = -sigma*c*ntemp(q)*(N2(q)+(dt/2)*j2-g*(N1(q)+(dt/2)*k2));
            k4 = sigma*c*n(q+1,m)*(N2(q)+dt*j3-g*(N1(q)+dt*k3))-N1(q)/t1;
            j4 = -sigma*c*n(q+1,m)*(N2(q)+dt*j3-g*(N1(q)+dt*k3));

            N1(q+1) = N1(q)+(dt/6)*(k1+2*k2+2*k3+k4);
            N2(q+1) = N2(q)+(dt/6)*(j1+2*j2+2*j3+j4);
        end
```

```
        % Calculating n(z,t) this way gives the same result as Runge-Kutta and is faster
        n(:,m) = n(:,m).*exp(dz*sigma*N0(m)*(N2-g*N1));

        % Propagate through length dz of sapphire
        n_field = ifft(fft(sqrt(n(:,m)).*exp(i*theta)).*SAphase);
        n(:,m) = abs(n_field).^2;
        theta  = unwrap(angle(n_field));
    end

    % Propagate through fused silica windows at exit of chamber
    n_field = ifft(fft(sqrt(n(:,m)).*exp(i*theta)).*FSphase);
    n(:,m) = abs(n_field).^2;
    theta  = unwrap(angle(n_field));

    % Pass pulse through mask and set exiting pulse as input pulse for next
    % pass
    n(:,m+1)  = mask*n(:,m);
end

% Calculate energy is pulse for each pass (transpose gives a column vector)
En         = (hv*(pi/2)*(r^2)*trapz(n,1)*c*dt)';

SimEnergy = En(passes+1);

output     = [taufwhm,SimEnergy];
```

D.2 Semi-classical three-step model

This code calculates the ADK rate for a given atom/ion under the influence of a given laser intensity. The code contains data for several different ionic species (neutral, 1+, and 2+) of argon, krypton, and xenon. In addition, the electron's return energy

is calculated as a function of the laser phase at the time of ionization. By combining these two calculations, the probability distribution for electrons, which are ionized and return to the position of the nucleus, to have a given energy upon return to the parent ion is calculated. This code generated Figures 4.3 and 4.4.

```
% Program to calculate ionization and free electron propagation steps
% of the 3-step semi-classical model of high harmonic generation

% must declare main rountine as a function to use subroutines
function y = stuff

% close all figures and clear all variables
close all hidden;
clear;

% time code execution: start timer
tic

% declare global variables
global phi2;

% Constants
lambda0 = 0.800;          % central wavelength (um)
tau     = 25;             % fwhm of pulse (fs)
I0      = 1e15;           % Peak intensity of pulse (W/cm^2)
c       = 0.3;            % speed of light (um/fs)
Iph     = 13.6;           % Ionization potential of hydrogen (eV)
hbar    = 6.5828439227E-16; % (eV*s)
m       = 9.1093826E-31;  % electron mass (kg)
charge  = 1.6021764620E-19; % electron charge (C)
eV2J    = charge;         % eV to J conversion factor
mu0     = 4*pi*1e-7;      % permeability of free space (N/A^2)
```

```
% Target atom/ion ionization potential (eV)
IpAr   = [15.76, 27.63, 40.79];% Ip of 1st three states of Ar (neutral, 1+, 2+)
IpKr   = [14.00, 24.36, 36.95];% IP of Kr
IPXe   = [12.13, 21.21, 32.10];% Ip of Xe
Zf     = [1, 2, 3];            % final charge state of ionization of respective states above


w0     = 2*pi*c/lambda0;   % central laser frequency
num    = 5e5;              % number of points in "range" half cycles
dphi   = 2*pi/num;         % phase step size
dt     = dphi/w0;          % time step size
phi    = [0:dphi:2*pi-dphi]; % phase array
N      = length(phi);      % length of phase array (same as num)

% electric field
E0 = (sqrt(I0*377*2)*100); % peak electric field value
E = E0*cos(phi);           % Electric field array (V/m)

% Step one: Tunnel ionization (ADK rates)

% decide which atom to look at
Ip  = IpAr(2); % Use ionization potential of Ar+
Z   = Zf(2);

% Calculation of ADK ionization rates
% Equations from Spielmann et al., "Near-keV Coherent X-Ray Generation with
% Sub-10-fs Lasers," IEEE JSTQE 4, 249 (1998)

wp     = Ip/hbar;
wt     = charge*abs(E)./sqrt(2*m*Ip*eV2J);
% E is in absolute value since the direction of the field does not
% matter for the ADK rate calculations
```

```
nstar   = Z*sqrt(Iph/Ip);
Cnsq    = (2^(2*nstar))/(nstar*GAMMA(nstar+1)*GAMMA(nstar));

% ionization probability per unit time
ws      = wp.*Cnsq.*(4*wp./wt).^(2*nstar-1).*exp(-4*wp./(3*wt));

% ionization probability for each time step
prob    = ws*dt*1e-15;

% Plot the probability                                                    70
lw = 2;
font = 18;
% plot(phi,prob,'k-','linewidth',lw)
% xlabel('Phase (\pi rad)','fontsize',font)
% ylabel('Probability of ionization','fontsize',font)
% set(gca,'Fontsize',font)
% set(gca,'linewidth',lw)

% Step two: Propagation of free electron in E-field (linearly polarized)
% from P.B. Corkum, "Plasma Perspective on Strong-Field                   80
% Multiphoton Ionization," PRL 71, 1994-1997 (1993).

x0 = charge*E0/(m*(w0*1e15)^2)*10^9; % Amplitude of electrons motion (nm)
v0 = charge*E0/(m*(w0*1e15))*10^-6; % Max velocity of electron (nm/fs)

% To save computation time, only 5000 points are used to calculate the
% return energy of the electron. The array is then interpolated to the
% correct number of data points.

Nzero = 5000;                                                             90
initphi = [0:2*pi/Nzero:2*pi*(1-1/Nzero)]; % phase array with 5000 points
offset=1e-4;
```

```
% Determine the return phase for an electron released at each phase of the
% laser pulse
for k = 1:Nzero;
    phi2 = initphi(k);
    % use fzero function to determine when the electron's position is zero
    % start search at a small phase after electron is released and check
    % for almost one full cycle                                          100
    % check that the position changes sign during that 2 pi cycle
    % fzero returns an error if this is not the case
    % if-statement sets return phase equal to inital phase
    % for trajectories that don't return to the parent ion
    if (sign(pos((phi2+offset)))~=sign(pos((phi2+2*pi-offset))))
        returnphi(k) = fzero(@pos,[(phi2+offset),(phi2+2*pi-offset)]);
    else
        returnphi(k) = phi2;
    end
end                                                                     110

% electron's velocity at the time of return
v2 = v0*sin(returnphi)-v0*sin(initphi);
% electron's energy at the time of return
e2 = 0.5*m*(v2*1e6).^2/eV2J;

% interpolate the return energy to num points
e2 = interp1(initphi,e2,phi,'cubic');

% calculate the ponderomotive energy                                    120
Up = lambda0.^2*I0*charge^2*mu0/(8*pi^2*m*c)*1e-2*1e-15/eV2J;

% find the max energy and index
emax = max(e2);

% Histogram the probability
```

```
numbins = 200;
estep = emax/(numbins-2);
eprob = zeros(1,numbins);
ehist = ((1:numbins)-1)*estep;

% add up probabilities for phases that result in a similar return energy
for k=1:N
    j = round(e2(k)/estep)+1;
    eprob(j) = eprob(j)+prob(k);
end

% normalize probability distribution
eprob=eprob/estep/sum(eprob);

% set the probability to 1e-9 if it equals zero so that it will plot nicely
eprob2 = eprob+(eprob==0)*1e-9;

% Plot probability distribution,
% but do not plot the probability of zero return energy
semilogy(ehist(2:end)/Up,eprob2(2:end),'k-','linewidth',lw)

% Add plot labels
xlabel('E_{RETURN}/U_{P}','fontsize',font)
ylabel('Probability/cycle/eV','fontsize',font)
set(gca,'Fontsize',font)
set(gca,'linewidth',lw)
axis([0 3.5 1e-4 1e-1]);

% Save figure as an EPS file
print -deps -r600 returnprob

toc
```

```
% determine the index of the maximum value of the return energy during the
% first laser half-cycle
[emax i] = max(e2(1:floor(N/2)));

plot(phi/pi,e2/Up,'k-','linewidth',lw)
axis([0 1/2 ylim]);
ylabel('E_{RETURN}/U_{P}','fontsize',font)
xlabel('Phase (\pi rad.)','fontsize',font)
set(gca,'fontsize',font,'linewidth',lw)
set(gca,'xtick',[0:1/8:1/2])
set(gca,'xticklabel',[' 0';'1/8';'1/4';'3/8';'1/2'])
hold on
plot([phi(i), phi(i)]/pi,[0,3.5],'k--','linewidth',lw)

print -deps -r600 e_energy


%-------------------------

% subrountine that calculates the electrons fractional position
% (position/x0). Since the purpose is to find the zero of the function,
% this is a valid procedure

function out = pos(phi3)
global phi2;

    out = (cos(phi3)-cos(phi2))+(phi3-phi2)*sin(phi2);
```

D.3 ADK calculation for arbitrary atomic states

This is the code outlined in Appendix B.

```
% Program to calculate the ADK rates for a give pulse and gas
```

```
close all hidden;
clear all;

% Constants
dt      = 0.1; % time step size (fs)
lambda0 = 0.800;% central wavelength (um)
tau     = 25;  % fwhm of pulse (fs)
En      = 2.35133; % pulse energy (mJ)
radius  = 75; % 1/e^2 radius of beam (um)
c       = 0.3; % speed of light (um/fs)
Iph     = 13.6; % Ionization potential of hydrogen (eV)
hbar    = 6.5828439227E-16; % (eV*s)
me      = 9.1093826E-31; % electron mass (kg)
charge  = 1.6021764620E-19; % electron charge (C)
eV2J    = charge; % eV to J conversion factor
mu0     = 4*pi*1e-7; % (N/A^2)

% Target atom/ion ionization potential (eV)
IpAr    = [15.76, 27.63, 40.79];% Ip of 1st three states of Ar (neutral, 1+, 2+)
IpKr    = [14.00, 24.36, 36.95];% IP of Kr
IpXe    = [12.13, 21.21, 32.10];% Ip of Xe
Zf      = [1, 2, 3];            % final charge state of ionization of respective states above
atom    = ['Ar';'Kr';'Xe'];
AllIp   = [IpAr; IpKr; IpXe];

% time array (fs)
twindow = 6;
t = [-twindow/2*tau:dt:twindow/2*tau];
N = length(t);

% Calculate peak intensity
I0 = En*1e-3/(tau*1e-15*sqrt(pi/(4*log(2)))*pi*(radius*1e-4).^2/2)
```

```
% electric field
w0 = 2*pi*c/lambda0;
E0 = (sqrt(I0*377*2)*100);
E = E0*exp(-2*log(2)*(t./tau).^2).*abs(cos(w0*t)); % (V/m)

% Loop through all the gases (1 = Argon, 2 = Krypton, 3 = Xenon)
for k = 1:3

% Atom and ion start in l=1 (p) state
l  = 1;

for m = 0:l % loop from 0 to l
    for j = 1:3
        % decide which atom to look at
        Ip  = AllIp(k,j);
        Z   = Zf(j);

        % Calculation of ADK ionization rates
        % Equations from Spielmann et al., "Near-keV Coherent X-Ray Generation with
        % Sub-10-fs Lasers," IEEE JSTQE 4, 249 (1998)

        wp     = Ip/hbar;
        wt     = charge*E./sqrt(2*me*Ip*eV2J);
        nstar  = Z*sqrt(Iph/Ip);
        Glm    = (2*l+1)*factorial(l+abs(m))*2^(-abs(m))/(factorial(abs(m))*factorial(l-abs(m)));
        lstar  = nstar - 1;
        Cnsq   = (2^(2*nstar))/(nstar*gamma(nstar+lstar+1)*gamma(nstar - lstar));

        ws(j,m+1,:)     = wp.*Glm.*Cnsq.*(4*wp./wt).^(2*nstar-m-1).*exp(-4*wp./(3*wt));

        frac(j,m+1,:)  = exp(-cumtrapz(ws(j,m+1,:)).*dt*10^-15);
    end
```

```
neut    = squeeze(frac(1,m+1,:));
oneplus = squeeze(frac(2,m+1,:))-squeeze(frac(1,m+1,:));
twoplus = squeeze(frac(3,m+1,:))-squeeze(frac(2,m+1,:));
threeplus = 1-squeeze(frac(3,m+1,:));

rn = neut.*squeeze(ws(1,m+1,:));
r1 = oneplus.*squeeze(ws(2,m+1,:));
r2 = twoplus.*squeeze(ws(3,m+1,:));



cutoff = exp(-4*log(2)*(t./tau).^2);

% Plot the fractional populations
lw = 2;
font = 18;

figure
plot(t,neut,'k-','linewidth',lw)
xlabel('Time (fs)','fontsize',font)
ylabel('Fractional population','fontsize',font)
set(gca,'Fontsize',font)
set(gca,'linewidth',lw)
hold on
plot(t,cutoff,'k--','linewidth',lw)
hold on
plot(t,oneplus,'r-','linewidth',lw);
hold on
plot(t, twoplus,'b-','linewidth',lw);
hold on
plot(t, threeplus,'g-','linewidth',lw);
xlim = 1.2*tau;
axis([-xlim xlim 0 1]);
```

```
    filename = [atom(k,:),'_ADK_',num2str(En),'_mJ_',num2str(2*radius),'_um_l=',num2str(l),'_m=',num2str(m),

    print(filename, '-depsc', '-r600')

    close;

    figure
    cutoff = cutoff.*max([max(rn),max(r1),max(r2)]);
                                                                                                    110
    plot(t,rn,'k-','linewidth',lw)
    xlabel('Time (fs)','fontsize',font)
    ylabel('Weighted ADK rate (s^{-1})','fontsize',font)
    set(gca,'Fontsize',font)
    set(gca,'linewidth',lw)
    hold on
    plot(t,cutoff,'k--','linewidth',lw)
    hold on
    plot(t,r1,'r-','linewidth',lw);
    hold on                                                                                         120
    plot(t,r2,'b-','linewidth',lw);
    axis([-xlim xlim ylim]);

    filename = [atom(k,:),'_ADK_',num2str(En),'_mJ_',num2str(2*radius),'_um_l=',num2str(l),'_m=',num2str(m),

    print(filename, '-depsc', '-r600')

    close;
end
end                                                                                                 130
```